BIOLOGICALLY INSPIRED ROSETTE NANOTUBE NANOCOMPOSITES FOR BONE TISSUE ENGINEERING, ORTHOPEDIC AND VASCULAR APPLICATIONS

BY

LIJIE ZHANG

B.S., TIANJIN UNIVERSITY, 2001

M.S., TIANJIN UNIVERSITY, 2004

M.S., BROWN UNIVERSITY, 2007

A DISSERTATION SUBMITTED IN PARTIAL FULFILLMENT OF THE REQUIREMENTS FOR THE DEGREE OF DOCTOR OF PHILOSOPHY IN THE PROGRAM IN BIOMEDICAL ENGINEERING AT BROWN UNIVERSITY

PROVIDENCE, RHODE ISLAND

MAY 2009

This dissertation by Lijie Zhang is accepted in its present form
by the Division of Engineering as satisfying the
dissertation requirement for the degree of Doctor of Philosophy.

Date_____ _____

Thomas J. Webster, Advisor

Recommended to the Graduate Council

Date_____ _____

Robert Hurt, Reader

Date_____ _____

Michael Lysaght, Reader

Date_____ _____

Jeffrey M. Karp, Reader

Date_____ _____

Shouheng Sun, Reader

Approved by the Graduate Council

Date_____ _____

Sheila Bonde, Dean of the Graduate School

CURRICULUM VITAE

Lijie (Grace) Zhang grew up in a beautiful northeast ocean city in China and obtained her Bachelor's degree in Chemical Engineering in 2001 and her Master's degree in Applied Chemistry from Tianjin University in 2004. She got numerous awards at Tianjin University including Motorola Inc. scholarship, Huachang Inc. scholarship, the excellent thesis award, and the excellent student awards. Then she received Edward Mason Fellowship to pursue her Ph.D. study at Brown University in 2005. While at Brown, she completed courseworks all with grade A for Master of Science degree in Chemical Engineering in 2007. Lijie successfully defended her Ph.D. thesis in Biomedical Engineering on January 12th, 2009. Supervised by Dr. Thomas J. Webster, she has published over seven peer-reviewed papers in the top journals in nanobiomaterial fields, six conference proceedings, and three book chapters related to bone tissue engineering and nanotechnology fields during the total 3.4 year study at Brown. In addition, her research was highlighted on NBC nightly news as an example of the future of medicine (May 14, 2007). She has given over 18 oral or poster presentations on annual meetings of leading associations in the world and received the STAR award from the Society for Biomaterials (Chicago) in 2007. During her Ph.D. study, Lijie also actively participated in various outreach activities and served as mentors of Rhode Island's high school teachers in Research Experience for Teachers program as well as mentors of elementary schools' students and K-12 teachers in the Mathematics and Science Partnership program funded by the NSF.

ACKNOWLEDGEMENTS

Many thanks go out to numerous people for helping me during my doctoral work. I would especially like to express my highest gratitude and thanks to Dr. Thomas J. Webster for being such a knowledgeable, supportive and generous advisor. I could not have chosen a better advisor than Dr. Webster in the world. Without his generous financial support, I could not have attended over 18 conferences and have had an enjoyable study life at Brown. Without his enthusiastic guidance, the dissertation would have gotten nowhere and I could not have published so many papers, book chapters and proceedings in 3.4 years. When I had difficulty in my experiments, he was always available to help and more quickly respond than I could have hoped. It is impossible to forget how many drafts of papers, book chapters, and conference abstracts he revised for me. He helped revise my dissertaion and readily gave me very important and helpful advice even during Christmas holidays. Dr. Webster is the nicest professor in the world. It has been my best luck to study in his lab and to develop my scientific writing, research skills and independent thinking under his encouragement and guidance. Thank you, Prof. Webster, for everything you have done for me!

I would like to sincerely thank my exceptional Ph.D. defense committee members Dr. Robert Hurt, Dr. Michael Lysaght, Dr. Shouheng Sun, and Dr. Jeffrey M. Karp for valuable advice and suggestions. I am extremely grateful to Dr. Robert Hurt for his warm help all these years. He admitted me into Brown University and gave me much useful

advice for my course study and advisor selection. In addition, I would like to thank Dr. Michael Lysaght for recommending me many good professors for postdoctoral searching. I would also like to thank Dr. Jeffery M. Karp at MIT for taking a train from Boston in the very early morning to attend my defense.

My especial thanks to Dr. Hicham Fenniri at University of Alberta in Canada and his lab members: Andrew J. Myles, Usha Hemraz, Sharwatie Ramsaywack, Felaniaina Rakotondradany and Jose Rodriguez for providing the rosette nanotubes and warm research assistance. It was impossible to successfully undergo the project without the good collaboration with Dr. Fenniri.

I gladly express my gratitude to Dr. Karen M. Haberstroh for taking her time on my career consulting. I would also like to thank Dr. Edith Mathiowitz, Dr. Jeffrey Morgan, Dr. Diane Hoffman-Kim and Dr. Amit Basu for their useful advice for my research.

I really appreciate the instruction and assistance of the following people: Chang Yao for teaching me the cell culture technology; Peishan Liu and Lei Yang for assistance with HA synthesis; Tony McCormick for assistance with TEM and SEM image collection; Dongwoo Khang for assistance with AFM image collection; Geoffrey Williams for assistance with the fluorescence microscopy imaging; Chris Bull for assistance with mechanical testing; Aihui Yan for assistance with particle size analysis; Reese Webb for assistance with XRD data collection; and Oluwaseun Adegbesan and Eli Fine for summer research assistance. I would like to thank National Institutes of Health for financial

support.

Most importantly, I would like to thank my husband Hongyu Song for his love, encouragement and endurance in my life. He is and always will be my inspiration in everything I do.

TABLE OF CONTENTS

Page

LIST OF TABLES

Page

LIST OF FIGURES

Page

CHAPTER 1

INTRODUCTION

A portion of this chapter has been published in:

1. **L. Zhang**, et al. Nanotechnology and Nanomaterials: Promises for Improved Tissue Regeneration. *Nanotoday*, 4(1):66-80 (2009).
2. **L. Zhang**, et al. Chapter 21: Nanoengineering for Bone Tissue Engineering, in: *Micro and Nanoengineering of the Cell Microenvironment: Technologies and Applications*, A. Khademhosseini, J. Borenstein, M. Toner, S. Takayama (Eds.), Artech House, 2008, 431-460.
3. **L. Zhang**, et al. Carbon Nanotubes and Nanofibers for Tissue Engineering Applications, in: *Carbon*, C. Liu (Ed.), Research Signpost, in press (2009).
4. **L. Zhang**, et al. Nanomaterials for Improved Orthopedic and Bone Tissue Engineering Applications, in: *Advanced Biomaterials: Fundamentals, Processing and Applications*, B. Basu, D. Katti, A. Kumar (Eds.), John Wiley & Sons Inc., in press (2009).

1.1 Demands and Problems in Orthopedic Applications

Bone defects, which are caused by a variety of reasons such as fractures originating from trauma, osteoarthritis, osteoporosis or bone cancers, represent a common and significant clinical problem. Since the first hip replacement conducted in 1923 and the most significant breakthrough which happened in the 1960s with the introduction of ultra low friction cemented arthroplasty by John Charnley [1-2], various bone implant surgeries and procedures (such as for healing bone fractures, repairing defects, and inserting hip and knee replacements) are routinely performed and have rescued a myriad of people suffering from intense pain and limited mobility from bone diseases.

Furthermore, with the increasing age of the U.S. population, there exists a strikingly increasing number of patients who need various orthopedic implants. For example, the National Center for Health Statistics (NCHS) reported that bone fractures for all sites increased from 1,002,000 in 1999 to 1,039,000 in 2004 [3]. In addition, there were about 345,000 hospitalizations for hip fractures in 2003 in the United States alone, but only one in four patients recovered completely. The American Academy of Orthopedic Surgeons reported that in the United States, in just a 4 year period, there was a 19.7% increase in hip replacements performed from nearly 274,000 procedures in 1999 (including 168,000 total hip replacements and 106,000 partial hip replacements) to 328,000 procedures in

2003 (including 220,000 total hip replacements and 108,000 partial hip replacements) [4]. The total hospitalization costs for knee replacements doubled to $11.38 billion in 2003 compared with $5.67 billion in 1999 [5].

However, it is important to note that traditional orthopedic implant surgeries (specifically, autografts and allografts to repair bone defects and hip and knee replacements to treat osteoarthritis) still have many shortcomings. For autografts, it is usually difficult to collect sufficient bone from patients and they also have the problem of donor site morbidity; for allografts, inflammation, rejection, resorption as well as transmission of diseases may frequently occur [6-8]. In addition, considering the endurance of current orthopedic implants (10-15 years on average), younger and more active patients (men under 60 years and women under 55 years) who have received orthopedic implants will inevitably need more than one revision surgery in their lives. For example, in the United States, nearly 11% of hip replacements (36,000 revisions for 328,000 replacements) and 8% of knee replacements (33,000 revisions for 418,000 replacements) were revision procedures of previously failed hip and knee replacements in 2003 [5]. A similar trend occurs in other industrialized countries. On the other hand, although osteoporosis (a disease in which bones become fragile and more likely to break) has been studied for a long time, no effective prevention and treatment methods exist for this disease. Consequently, patients may suffer intense pain caused by these bone defects and complications can dramatically increase health insurance costs at the hospital.

In summary, due to the greater numbers of elderly patients and the relatively high percentage of revision procedures performed around the world, it is urgent to develop a new generation of biocompatible bone substitutes which can restore and improve bone functions as well as significantly lengthen the lifetime of current orthopedic implants. An emerging interdisciplinary field (bone tissue engineering), thus, has evoked increasing interest from scientists wishing to develop novel biological substitutes in order to treat various bone defects.

1.2 Complications Related to Implant Failures

But before discussing ways to design novel biomaterials for orthopedic and bone tissue engineering applications, it is important to thoroughly investigate the fundamental reasons of implant failure. In fact, there are many complications which may occur during different stages of material implantation and finally result in failure. For example, in the early stage of implant surgery, acute complications, infection, inflammation, prosthesis dislocations, and surgery-mediated complications (such as improper placement and cement extrusion) may be reasons for implant failure [9]. After several years, implant loosening originating from insufficient osseointegration, osteolysis, and wear of articular bearing surfaces becomes the main reason necessitating revision surgery [9]. Taking Canada as an example, the Canadian Joint Replacement Registry (CJRR) reported that

the most common reasons for total hip replacement revisions were implant loosening (55%), followed by osteolysis (33%), implant wear and tear (30%), instability/dislocation (17%), bone and implant fracture (12%), and infection (10%) in 2004 [10]. Because some patients have more than one reason necessitating orthopedic implant revision surgery, the aforementioned percentages do not add up to 100%. In the following sections, specific complications leading to implant failures are described.

1.2.1 Biological Failure

Osseointegration, which was initially described as the formation of a direct structural and functional bone-to-implant contact area under load by Per-Ingvar Branemark [11], is a crucial criterion for the long-term success of orthopedic implants. It plays an important role in minimizing the motion-induced damage to surrounding tissues. In other words, insufficient bonding between the implant material and juxtaposed bone may lead to a mismatch in mechanical properties between an implanted material and surrounding bone tissue, thus, resulting in implant loosening and failure.

Many factors including material surface roughness, overloading, inflammation and infection [12-13] have been reported to be related to insufficient osseointegration. Specifically, surface properties of implant materials may be intimately involved in the successful osseointegration between an endosseous implant and bone. Actually,

numerous studies have elucidated that surface roughness of implant materials affects the rate of osseointegration and biomechanical fixation [14-15]. Since traditional orthopedic implant materials (i.e., metals, ceramics, polymers and composites thereof) have only been chosen for implantation based on their mechanical properties and biological inertness, there has not been a large emphasis concerning biomaterial chemical and surface properties to date. Consequently, a variety of implant failures originating from insufficient osseointegration and stress-strain imbalances have frequently taken place when using such conventional materials in orthopedic applications.

The formation of a fibrous soft tissue capsule which originates from excessive secretion of fibrous tissue from inflammatory cells is a vital factor that leads to insufficient osseointegration (Figure 1.1) [16-17]. After inserting a biomaterial into a surgical site, damage to the surrounding tissue causing injury is inevitable. As a response to such injury, various host responses (such as infection and inflammation) are triggered as shown in Figure 1.1. Initially, neutrophils and macrophages arrive at the injury site and begin to attempt to phagocytose the implanted material; when they fail to engulf this large mass, they fuse together to form giant cells and interrogate the biomaterial again resulting in walling it off from the surrounding tissue. At the same time, giant cells send out chemical messengers (e.g., cytokines) to recruit other cells to “help” them. In response to cytokines, fibroblasts (which secrete and synthesize collagen comprising the extra-cellular matrix of the soft tissue capsule [18]) arrive and generate a collagen

capsule, the first sign of a new tissue. The final stage of the process is that the implant is completely encapsulated in an acellular, avascular collagen bag about 50-200 micrometers thick [16]. The fibrous capsule prevents sufficient bonding between an implant surface and juxtaposed bone and frequently leads to clinical failure of orthopedic implants. Consequently, repelling fibroblasts cause such an inflammatory reaction is necessary at the surface of a newly implanted orthopedic device [17]. Moreover, controlling protein adsorption by altering biomaterial surface properties is an effective method towards attracting desirable cells (such as osteoblasts) onto the implant surface and minimizing the functions of fibroblasts (such as their adhesion and secretion of fibrous tissue) [17].

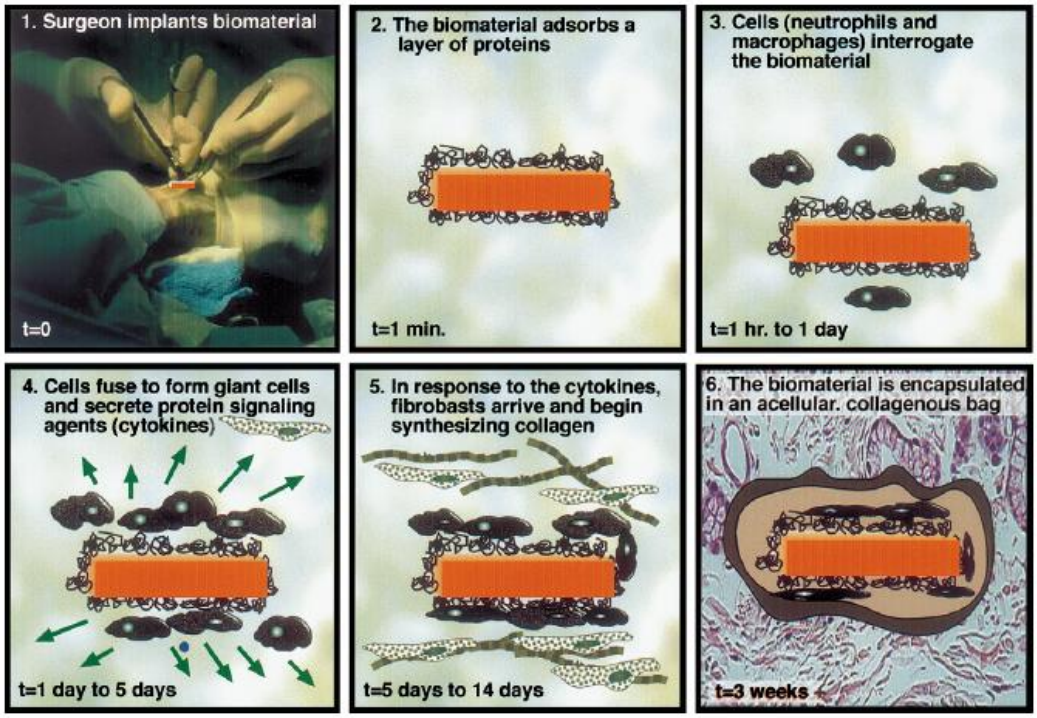

Figure 1.1 The foreign body response towards an implanted biomaterial. 1) A biomaterial is implanted and damage to surrounding tissue occurs. 2) In seconds to minutes, non-specific proteins from body fluids adsorb on the implant surface. 3)

Neutrophils and macrophages interrogate the material. 4) Failing to interrogate the material, cells fuse to form giant cells and concurrently secrete cytokines to signal other kinds of cells. 5) and 6) Fibroblasts arrive and fabricate a collagenous bag to insulate the material from the surrounding tissue. This figure is adapted from [16].

1.2.2 Material Failure

As a late-appearing complication, osteolysis induced by wear particles from implant materials has been regarded as one of the most common complications leading to revision surgery after a primary implant replacement [19-22]. It can cause severe bone loss which eventually results in implant instability and failure. Since they are commonly used as implants, metals, ceramics and polymers (such as polyethylene, a common material used as the acetabular component in hip replacements) are widely found in the form of prosthetic wear particles and serve as major contributors to bone resorption. These wear particles appear most commonly at the bearing implant surface but are also at the host-implant or implant-implant interfaces. Figure 1.2 illustrates the osteolysis process caused by biomaterial wear debris.

Macrophages are believed to play a key role during osteolysis. A critical number of active macrophages exist necessary for osteolysis since only one disturbed macrophage and its neighboring osteoclast would not cause osteolysis. For instance, clinical experience indicates that osteolysis can not happen if the wear rate of the polyethylene cup is below 0.05 mm per year. In contrast, osteolysis frequently occurs if the wear rate exceeds 0.2 mm per year [23]. Moreover, studies have also illustrated that there exists a critical size for bioactive particles to trigger cellular responses and finally result in osteolysis.

Macrophages have evolved to detect and phagocytose bioactive particles in the size range of 0.5-10 μm. Particles larger than 10 μm or less than 0.5 μm are relatively less active for macrophages. Particles larger than 10 μm will cause extensive giant cell responses leading to the formation of fibrous tissue (see details in 1.2.1) without osteolysis. In addition, particles with sharp edges are more active than spherical particles [22].

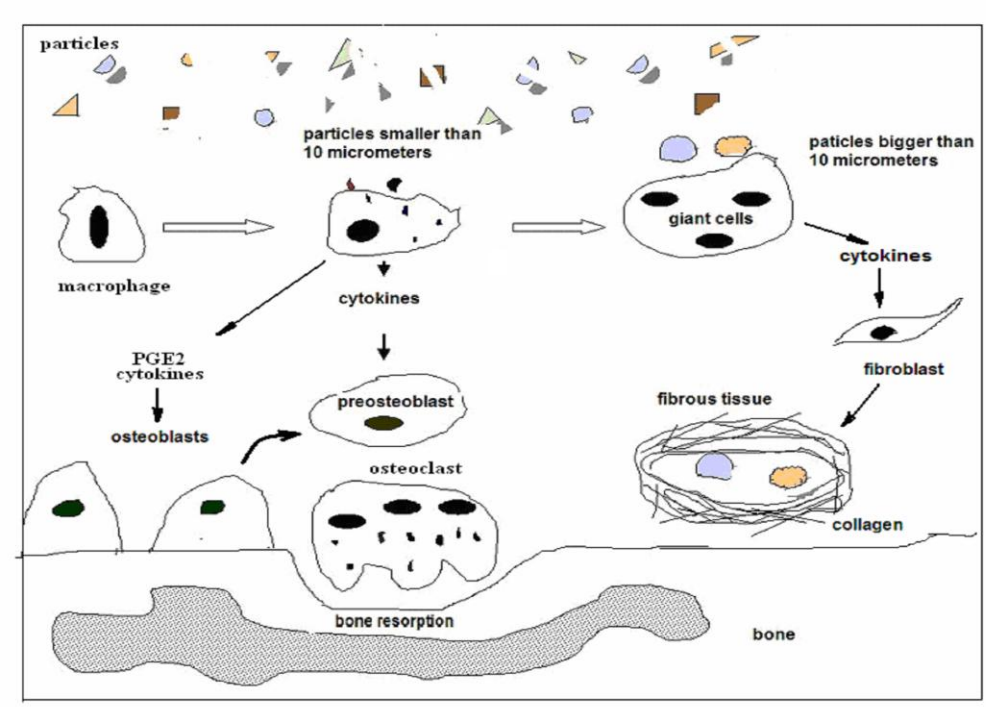

Figure 1.2 Schematic illustration of biomaterial wear debris activating macrophages and inducing osteolysis. Particulate debris is generated from wear of arthroplasty components, metal corrosion, ceramic failure, or polymer degradation. Particles <10 μm are engulfed directly by macrophages but can not be digested easily. Consequently, macrophages begin to release interleukins (IL-1, IL-6), prostaglandin E_2 (PGE_2), and tumor necrosis factors (TNF) which then mediate bone resorption via osteoclasts [22]. Macrophages form giant cells to phagocytose large particles (>10 μm) and then secrete cytokines to signal fibroblasts to synthesize collagen to result in a fibrous tissue capsule around the implant. This figure is adapted and redrawn from [24-25].

It is apparent that minimizing the generation of wear particles in interfacial tissues is a

fundamental approach to preventing osteolysis. Therefore, there has been an enormous amount of effort to design alternative wear-resistant bearing implant materials in order to reduce the production of wear particles. Metal-on-metal, ceramic-on-ceramic or ceramic-on-polyethylene implant components have been developed to prevent osteolysis and have been shown to produce less wear particles in vitro or in vivo than the conventional metal-on-polyethylene implant components [26-27]. For example, a five-year prospective randomized study in the U.S. revealed that osteolysis was greatly decreased from 14.0% in patients with metal-on-polyethylene bearings compared to 1.4% in patients with alumina-on-alumina ceramic bearings [26]. Furthermore, metal-on-metal bearings exhibit low wear rates (such as 0.004 mm per year compared with 0.1 mm per year for polyethylene on metal [27]). However, despite such promise, there still exist many concerns about the generation of metal ions or corrosion for metal combinations, leading to implant failure in the long term.

In addition, the more active and younger the patients who receive orthopedic implants are, the higher the risk of articulating bearing surface wear [28]. In fact, wear of articulating bearing surfaces has commonly evoked our attention. From a basic mechanical viewpoint, adhesive wear, abrasive wear, third body wear, wear fatigue and corrosion are five major mechanisms causing wear of articulating bearing surfaces [29]. Modification of polyethylene and substitution of metal-metal or ceramic-ceramic bearings for polyethylene may both help to improve the wear-resistant property of implant materials. Moreover, bone cements (such as poly(methyl methacrylate), or PMMA) are common materials used in current orthopedic implant for fixing implant into the bone. However,

there still exist some problems related to the current bone cement materials. Specifically, the exothermic reactions of PMMA polymerization may severely damage the surrounding bone tissue during the cure process in situ [30], thus, leading implant failure.

1.2.3 Other Complications

In addition to those described above, there are other complications which may lead to implant failure. Several investigations have revealed that periprosthetic femoral fractures accompanied with total hip replacements are more common after revision surgeries than after primary replacements [31-32]. So with an increasing number of revision surgeries, it is expected that periprosthetic femoral fractures will become more common. Since mechanical properties (including strength, toughness, and ductility) of implant materials are closely related to the above complications and can influence long-term success of an orthopedic implant, synthesizing a wide range of orthopedic implant materials which mimic the various mechanical properties of natural bone is rather desirable.

It should be realized that the above orthopedic implant complications are related to each other. That is, the previously mentioned high rates of implant failures may be accompanied by a loose implant and insufficient osseointegration [9, 33]; insufficient osseointegration can be caused by inflammation or osteolysis; and wear particle generation and infection often coexist with extensive wear of articulating surfaces. Therefore, reducing the influence of one implant failure complication may have extreme positive effects on preventing other complications and finally improving the long-term

success of orthopedic implants. A promising direction in bone tissue engineering and orthopedic implant design is to synthesize novel bone-like biomaterials which possess not only mechanical properties similar to those of physiological bone but also cytocompatible surface properties (such as surface roughness, energy, etc.) in order to successfully promote quick sufficient osseointegration of an implant at defect sites. This is being accomplished with nanotechnology.

1.3 Nanostructured Bone and Bone Remodeling Process

1.3.1 Nanostructured Bone

From the point of view of chemical composition, natural bone is a well-organized composite matrix that consists of a protein based soft hydrogel template (i.e., collagen, noncollagenous proteins and water) and hard inorganic components (specifically, hydroxyapatite or HA, $Ca_{10}(PO_4)_6(OH)_2$)) [17] (Figure 1.3). Furthermore, it is important to point out that all of the components in the bone matrix are nanometer in dimension. For instance, 70 % of the human bone matrix is composed of inorganic nanocrystalline HA which is typically 20-80 nm long and 2-5 nm thick [18]. Additionally, other components in the bone matrix (i.e., type I collagen which is 300 nm in length and 1.5 nm in diameter and noncollagenous proteins (such as laminin, fibronectin and vitronectin)) are all nanometer-scale in dimension [17]. Clearly, this unique structure of bone can create special physical properties (such as Young's modulus, elasticity, and strength) in order to support various mechanical loads during human activity. However,

the conventional implant materials mainly own micron or above particle/grain sizes which did not mimic the nanostructure of bone and may elicit many complications during implantation as described in previous sections.

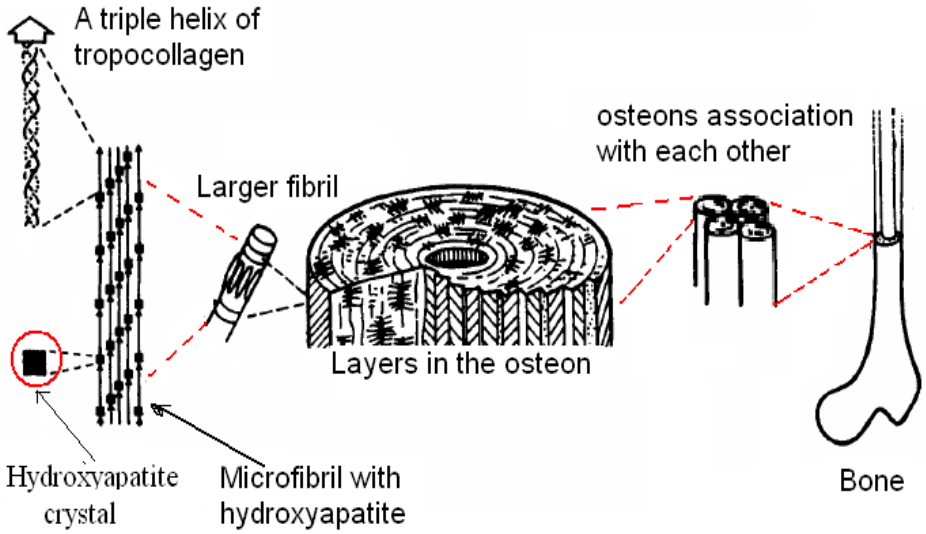

Figure 1.3 Schematic illustration of the cortical bone structure (As an example, the femur) and a detailed structure of osteon which is the circular arrangements of bone around vascular channels [17] as basic functional units of compact bone. This figure is adapted and redrawn from [34-36].

1.3.2 Bone Cell and Cell-Implant Interactions

Since bone is a living organ with self-repairing functions, various bone cells including osteoblasts (bone forming cells), osteoclasts (bone resorbing cells), and osteocytes (mature osteoblasts) are actively involved in normal bone functions. Specifically, osteoblasts contribute to extra-cellular matrix (ECM) mineralization and new bone synthesis. In the bone regeneration process, osteoblasts actively interact with proteins (i.e., fibronectin, laminin and vitronectin) and will adhere on implant surfaces immediately after the absorption of proteins and other minerals [17]. Figure 1.4 illustrates

the interactions among cells, proteins and a model implant material. Generally, although each type of protein has a different amino acid sequence, the short peptide domain, arginine-glycine-aspartic acid (RGD), is a well known cell adhesive domain in many proteins including fibronectin, vitronectin and collagen. It has been known that the RGD domain may interact specifically with integrin receptors of cell membrane receptors and improve osteoblast adhesion. After osteoblast adhesion, osteoblasts actively proliferate, develop an ECM and differentiate into mature bone. Clearly, initial osteoblast adhesion on an implant material is a prerequisite for osseointegration of the implant to juxtaposed bone.

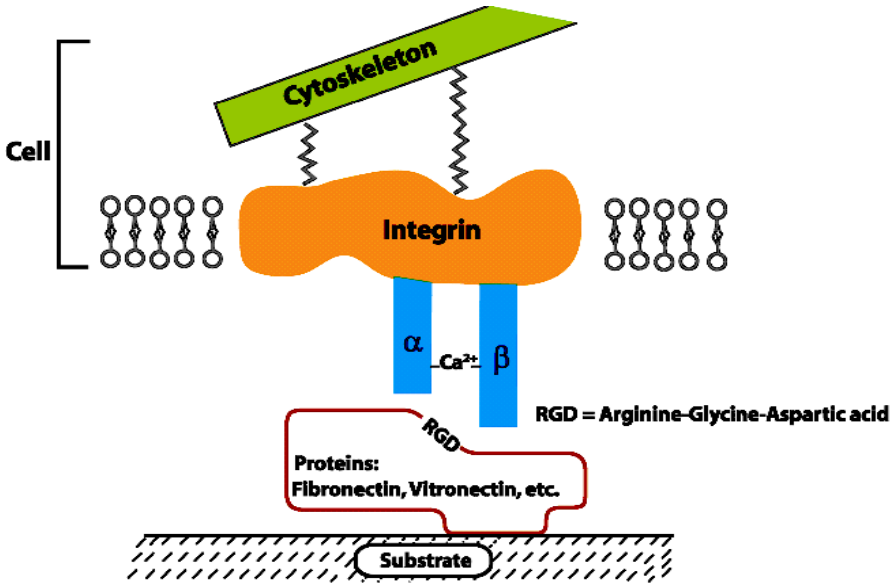

Figure 1.4 Schematic illustration of proteins mediating cell adhesion on biomaterial surfaces. This figure is adapted from [37].

1.3.3 In Vivo Bone Remodeling

Moreover, in vivo bone remodeling is a complicated process involving various types of

cells activities. Mesenchymal stem cells or hematopoeitic cells, which have the capacity to differentiate into osteoblasts, osteocytes, endothelial cells, fibroblasts and osteoclasts, are supplied to bone via the vascular network in the bone marrow [17]. Under the influence of different growth factors, cytokines, and proteins present in the physiological bone matrix, different cell types can be activated for bone regeneration. For example, bone remodeling in cortical and trabecular bone includes a continuously activation of osteoclasts, leading to resorption of bone, and formation of new bone by osteoblasts on the site of the old resorbed bone [17]. Under normal physiological conditions, the bone remodeling process is continual throughout a person's lifetime.

Figure 1.5 illustrates the different stages of bone remodeling after implantation. After the initial absorption of specific protein, desirable cell types (i.e., osteoblasts, osteoclasts and osteocytes) can be recruited to the implant surface. Then, osteoclast resorption activity, and more importantly, osteoblast adhesion, proliferation, differentiation and mineralization can be well coordinated to form new bone on the implant surface as previously mentioned. For bone tissue engineering and orthopedic applications, sufficient bone remodeling at the implant-tissue interface is very important for mediating the long-term success of implants. Insufficient bone remodeling around implant materials or excessive remodeling coupled with massive bone resorption and osteolysis will lead to implant failure. Since the surface properties of implant materials intimately affect the initial protein adsorption from biological fluids and further selective recruitment as well as activation of favorable cell (such as osteoblast) functions, surface modifications (such as altering the implant surface topography and chemistry) have become popular methods

to achieve suitable bone remodeling and improve osseointegration. This is especially true for nanotechnology approaches to improve orthopedic implant efficacy.

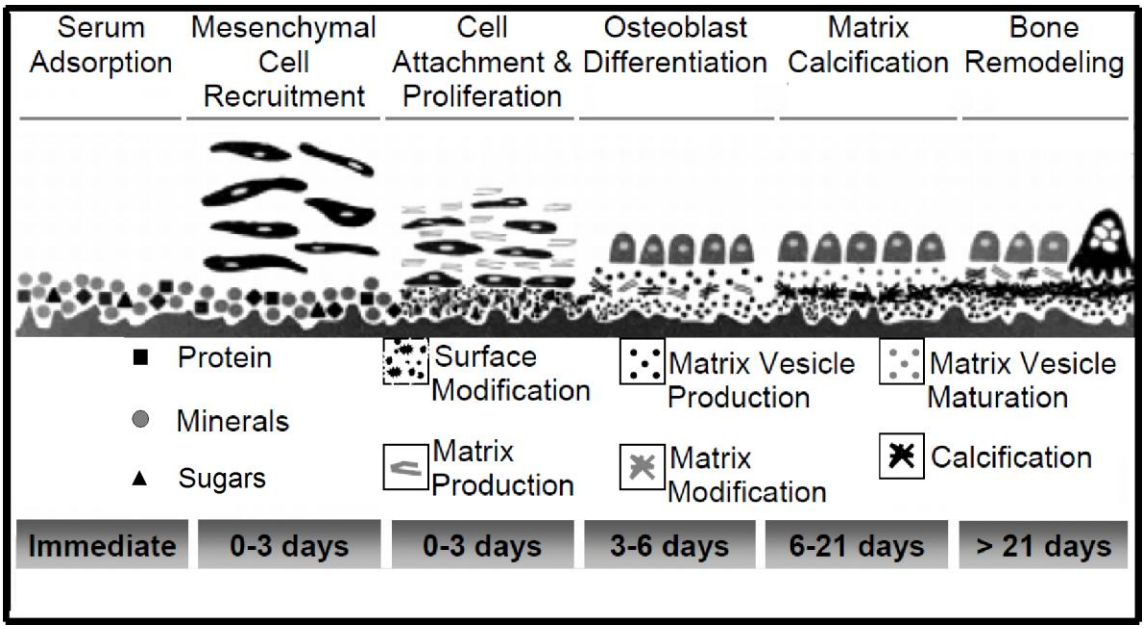

Figure 1.5 The different stages of bone regeneration on implant surfaces. This figure is redrawn and adapted from [38-39].

1.4 Nanotechnology and Nanomaterials: Biomimetic Tools for Bone Tissue Regeneration

In 1959, Nobel award winner Richard Feynman first proposed the seminal idea of nanotechnology by suggesting the development of molecular machines. Ever since, the scientific community has investigated the role that nanotechnology can play in every aspect of society. The intrigue of nanotechnology comes from the ability to control material properties by assembling such materials at the nanoscale. The tunable material properties that nanotechnology can provide were stated in Norio Taniguchi's paper in 1974 where the term "nanotechnology" was first used in a scientific publication [40-41].

Nanotechnology has been widely used in many fields (i.e., various quantum dots and nanoparticles in diagnostics, drug delivery, and therapeutics). Nanomaterials are materials with basic structural units, grains, particles, fibers or other constituent components in the range of 1-100nm [42]. Compared to respective conventional micron-scale materials, nanomaterials exhibit enhanced cytocompatibility, mechanical and electrical properties.

Since natural bone is nanometer in dimension and various bone cells directly interact with (and create) a nanostructured ECM, the biomimetic features and excellent physiochemical properties of nanomaterials play a key role in promoting bone cell functions as well as guiding tissue regeneration. Even though it was a field in its infancy a decade ago, currently many biocompatible nanomaterials were designed for bone tissue engineering and orthopedic applications. From a material property point-of-view, nanomaterials for bone tissue engineering and orthopedic applications can be made of ceramics, polymers, metals, organic materials and composite thereof, just like conventional or micron structured materials. In addition, nanomaterials including nanoparticles, nanoclusters, nanocrystals, nanotubes, nanofibers, nanorods, etc. have been tested for bone regeneration. To date, numerous top-down and bottom-up nanofabrication technologies (such as electrospinning, phase separation, self-assembly processes, thin film deposition, chemical vapor deposition, chemical etching, nano-imprinting, photolithography, electron beam or nanosphere lithographies [43]) are available for the design of nanomaterials with ordered or random nanotopographies. Nanomaterials can also be grown or self-assembled into nanotubes/nanofibers which can even more accurately simulate the dimensions of natural entities, such as collagen fibers. After

decreasing material size into the nanoscale, dramatically increased surface area, surface roughness or surface area to volume ratios of nanomaterials may lead to a higher surface reactivity with many superior physiochemical properties (i.e., mechanical, electrical, optical, catalytic and magnetic properties, etc.) [44]. Therefore, nanomaterials with such excellent properties and biomimetic features have become quite popular in orthopedics.

As is well-known, material surface properties mediate specific protein adsorption and bioactivity before cells adhere on implants, further regulating cell behavior and dictating tissue regeneration [17]. Furthermore, as mentioned in the previous sections, insufficient osseointegration may lead to a separation between implant materials and surrounding bone tissues, even causing implant failures. By controlling surface properties (such as surface roughness, wettability, and chemistry) of implant materials, successful osseointegration between an endosseous implant and bone may be achieved. In addition, other complications (i.e., osteolysis, inflammation, etc.) are also directly or indirectly related to the existing non-biologically inspired properties of conventional implant materials. Therefore, numerous researchers in bone tissue engineering have focused on the overall design and synthesis of bone-like nanomaterials with favorable surface properties in order to more successfully promote bone growth. Specifically, Figure 1.6 illustrates one of possible underlying mechanisms of the superior properties of nanomaterials to conventional micron structured materials for tissue engineering applications. Specifically, since nanomaterials have the increased surface area, surface wettability and favorable surface chemistry compared to conventional materials, they may contribute to increase protein adsorption and bioactivity, promote osteoblast functions and rapidly induce osseointegration by mimicking the nanostructure of bone

[45]. There has already been much progress studying the use of nanomaterials (Specifically, ceramics, metals, and polymers and nanotubes/nanofibers) for bone tissue engineering; this will be the focus of the next section.

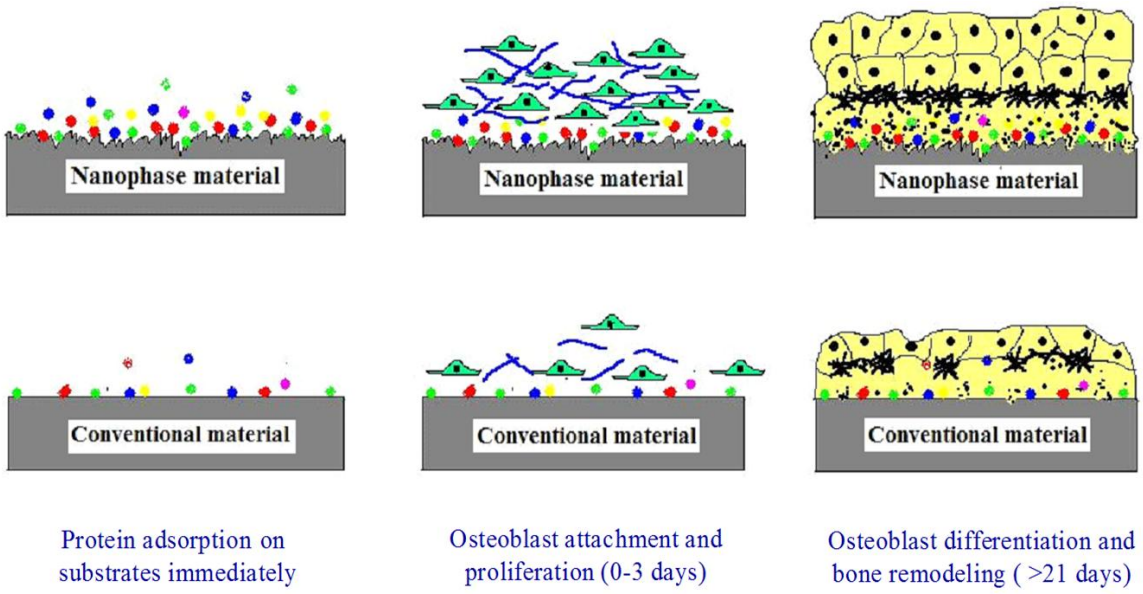

Figure 1.6 Schematic illustration of the possible mechanism by which nanomaterials may be superior to conventional materials for bone regeneration. The bioactive surfaces of nanomaterials mimic those of natural bones to promote greater amounts of protein adsorption and efficiently stimulate more new bone formation compared to conventional materials. This figure is adapted from [45]

1.4.1 Nanoceramics

Ceramics are non-metallic inorganic materials which have excellent cytocompatibility properties and possibly a high degree of biodegradability in the physiological environment, making them attractive for orthopedic applications. For instance, hydroxyapatite (HA), which is one of the most popular bone graft substitutes, coatings and filler materials, has good osteoconductive properties. Its surface can undergo

selective chemical reactivity with surrounding tissues, resulting in a tight bond between bone and the implant. Thus, new bone formation will be improved by the bonded interface [46] and consequently osseointegration occurs more quickly. For these reasons, ceramics have been widely adopted as orthopedic implants (known as bioceramics for several decades). According to the tissue response in an osseous environment, bioceramics can be classified into three groups: bioactive ceramics (such as HA, tricalcium phosphate (TCP), bioglasses, HA/TCP bi-phase ceramics, and glass-ceramics), biopassive ceramics (such as alumina, titania and zirconia), and biodegradable ceramics (such as TCP). Although traditional bioceramics have long served as bone substitutes and filler materials, structural forms, and surface coatings in orthopedic applications [47], there often exists a variety of implant failures due to insufficient osseointegration, osteolysis as well as ceramic implant wear. Therefore, nanoceramics which mimic the nanostructure of natural bone are ideal candidates for orthopedic and bone tissue engineering applications.

With a decreased grain size as well as a decreased pore diameter, nanoceramics possess increased surface area, surface roughness and number of grain boundaries at the surface. For example, from the results of extensive material characterization studies, increased surface roughness and improved surface wettability (i.e., decreased contact angles) are evident in nanophase compared to conventional alumina, HA and titania [48]. In the case of zinc oxide (ZnO), atomic force microscopy (AFM) root-mean-square roughness values of nanophase and microphase ZnO were 32 and 10 nm, respectively [49]. Additionally, a 23 nm grain size alumina had approximately 50% more surface area for cell adhesion

than that of a 177 nm grain size alumina; similarly, a 32 nm grain size titania had nearly 35% more surface area than that of a 2.12 μm grain size titania (Figure 1.7) [15]. A nanophase ZnO compact had 25% more surface area than that of microphase ZnO [49].

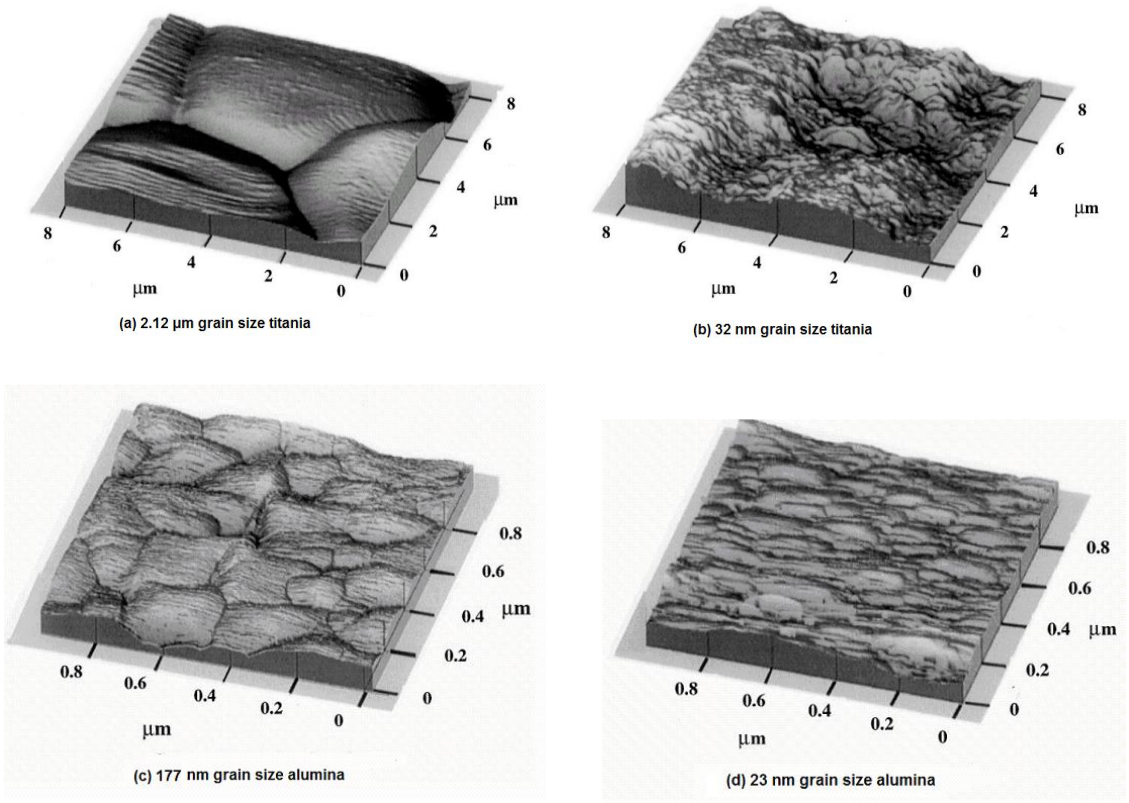

Figure 1.7 AFM images of nanophase and conventional titania and alumina. (a) and (c) represent conventional titania and alumina, respectively, and (b) and (d) represent nanophase titania and alumina, respectively. This figure is adapted from [15].

Furthermore, the special surface properties of nanoceramics are closely related to their excellent cytocompatibility properties. Just taking nanophase HA as an example, it has been demonstrated that higher amounts of surface porosity, increased surface roughness and improved wettability of nanophase HA had positive effects on improving osteoblast functions (such as adhesion, proliferation and differentiation) and osseointegration with

juxtaposed bone [17,39,48]. Specifically, some in vitro studies demonstrated that nanophase HA (67 nm grain size) significantly enhanced osteoblast adhesion and strikingly inhibited competitive fibroblast adhesion compared to conventional, 179 nm grain size HA, after just 4 hours of culture [48]. In addition, enhanced osteoclast-like cell functions (such as the synthesis of tartrate-resistant acid phosphatase (TRAP) and the formation of resorption pits) have also been observed on nano HA compared to conventional HA [50].

Importantly, such results have not been limited to in vitro studies. In vivo studies also demonstrated that nanocrystalline HA accelerated new bone formation on tantalum scaffolds when used as an osteoconductive coating compared to uncoated or conventional micron size HA coated tantalum [39]. Histological examination revealed that nanocrystalline HA coatings promoted greater amounts of new bone growth in the rat calvaria than uncoated or conventional HA coated tantalum after 6 weeks of implantation. Recently, a bioresorbable nanocrystalline HA paste was used as a valuable addition to TCP-HA ceramic granules for acetabular bone grafting in animal models. That study showed that the nanocrystalline HA paste resulted in better acetabular cup stability than the pure allografts and at the same time did not cause adverse biological reactivity [51]. Histology slides in human cancellous bone revealed that nanocrystalline HA paste appeared to be a suitable bone substitute for bone defects or cavities since it showed good tissue incorporation, high biocompatibility and rapid osseointegration [52].

A similar tendency has been reported for other nanoceramics including alumina, zinc

oxide and titania, thus, providing strong evidence that, to some extent, it may not matter what implant chemistry is fabricated to have nanometer surface features to promote bone growth. For example, a 51% increase in osteoblast adhesion and a 235% decrease in fibroblast adhesion were observed on alumina as grain size decreased from 167 to 24 nm in a 4-hour period [48]. The above decreased competitive fibroblast functions on nanoceramics are important to stimulate sufficient osseointegration. Since excessive secretion of fibrous tissue from fibroblasts causes the formation of a detrimental fibrous tissue capsule that leads to loosening of implants, decreased fibroblast functions on nanophase ceramics may contribute to a better bone-implant interface. Moreover, osteoblast adhesion increased by 146% and 200% on nanophase ZnO (23 nm) and titania (32 nm) compared to microphase ZnO (4.9 μm) and titania (4.1 μm), respectively [49]. Furthermore, nanophase ZnO, nanophase titania and nanofiber alumina enhanced collagen synthesis, alkaline phosphatase activity and calcium mineral deposition by osteoblasts compared to conventional equivalents [49, 53]. On the other hand, the inhibited *Staphylococcus epidermidis* (a common bacterium contributing to an undesirable biofilm around the implants) functions were also observed on nanophase ZnO and titania [49].

It elucidated that the special surface topography as well as wettability of nanophase ceramics may be the main reason for the observed promoted bone cell functions on nanoceramics. At the tissue-implant interface, the first and necessary step for success is the adsorption of specific proteins onto biomaterial surfaces (see section 1.3.2). Many researchers have demonstrated that the protein adsorption process depends on surface

properties (such as hydrophilicity, charge density, roughness, and surface energy) [54-55]. For instance, on hydrophilic and nanorough surfaces, studies have shown maximum vitronectin, fibronectin and laminin adsorption [48, 54-55]. Specifically, the highest concentration of vitronectin (a protein known to mediate anchorage-dependent cell adhesion) adsorption on nanophase ceramics may explain the subsequent enhanced osteoblast adhesion on nanophase ceramics [48]. Webster et al. demonstrated that increased unfolding of vitronectin adsorbed on nanophase alumina compared to conventional alumina [106]. Furthermore, the unfolding vitronectin adsorption on nanophase alumina may promote to expose cell-adhesive epitopes (such as RGD) on proteins for subsequent interaction with cell-membrane integrin receptors and further mediating cell adhesion. Therefore, they indicated that enhanced vitronectin adsorption, conformation and bioactivity may explain the increased osteoblast adhesion on nanophase alumina. Clearly, surface properties are closely related to anchorage-dependent cells (like osteoblasts and osteoclasts) adhesion to a biomaterial surface. After that, cell proliferation, differentiation, and ECM deposition can happen and contribute to a successful integration with surrounding tissue.

On the other hand, mechanical properties (such as hardness, ductility, stiffness, bending, compressive and tensile strength) of biomaterials play a crucial role in the long-term success of orthopedic implants. Many attempts and efforts have ensued to improve mechanical properties of orthopedic materials in order to mimic those of physiological bone. For example, in a recent study, Nukavarapu et al. fabricated a biodegradable nano-HA/polyphosphazene microsphere 3-D scaffold which had suitable mechanical

properties (compressive moduli of 46-81 MPa) and cytocompatibility properties for bone tissue engineering applications [56]. It should not be surprising that nanostructured composites have similar mechanical properties to bone since bone itself is a nanostructured composite. Moreover, a variety of nanocomposites (such as zirconia-toughened alumina nanocomposites [57], ceria-stabilized tetragonal zirconia–alumina nanocomposites [58] and HA coated ceria-stabilized tetragonal zirconia–alumina nanocomposites [59]) have shown promise as bearing materials with excellent cytocompatibility and low wear rates in order to prevent osteolysis. In summary, nanoceramics can offer significantly improved mechanical properties, good wear properties as well as excellent cytocompatibility compared to conventional ceramics.

1.4.2 Nanometals

Due to their excellent mechanical and suitable biocompatibility properties, metals and their alloys are the most common materials used in orthopedic applications. However, complications frequently occur on these traditional metal implants (including insufficient and unsustainable osseointegration). Thus, nanophase metals have been extensively investigated for orthopedic applications due to their higher surface roughness, energy, and presence of more particle boundaries at the surface compared with conventional micron metals.

For example, Webster et al. provided the first evidence that nanophase Ti, Ti6Al4V and CoCrMo possessed greater surface roughness at the nanoscale and significantly enhanced osteoblast adhesion compared to respective conventional metals [60]. Furthermore,

Figure 1.8 shows osteoblast morphology on nanophase and conventional metals. Obviously, compared to conventional metals, osteoblasts spread well on nanophase Ti and Ti6Al4V with increased roughness and surface particle boundaries [60]. In addition, recently Puckett et al. created linear nano-featured patterned Ti via electron beam evaporation. This study revealed that the nano region of the patterned Ti induced greater osteoblast adhesion than the micron- rough regions and controlled osteoblast morphology and alignment more similar to th at observed in situ in natural bones [61]. Moreover, an electrochemical method known as anodization, a well-established nano surface modification technique, has been used to fabricate highly porous TiO_2 nanotube layers on Ti. Through the anodization of Ti in dilute hydrofluoric acid (HF) electrolyte solutions, nanotubes with diameters around 100 nm and lengths around 500 nm can be formed in the TiO_2 layers of Ti. Yao et al. reported greatly improved osteoblast functions on nanotubular anodized Ti compared to unanodized Ti in vitro [62]. Moreover, increased chondrocyte (cartilage-forming cells) adhesion was also observed on anodized nanotubular Ti compared to unanodized Ti in a recent study, thus, suggesting the possibility of promoting cartilage growth on anodized Ti [63].

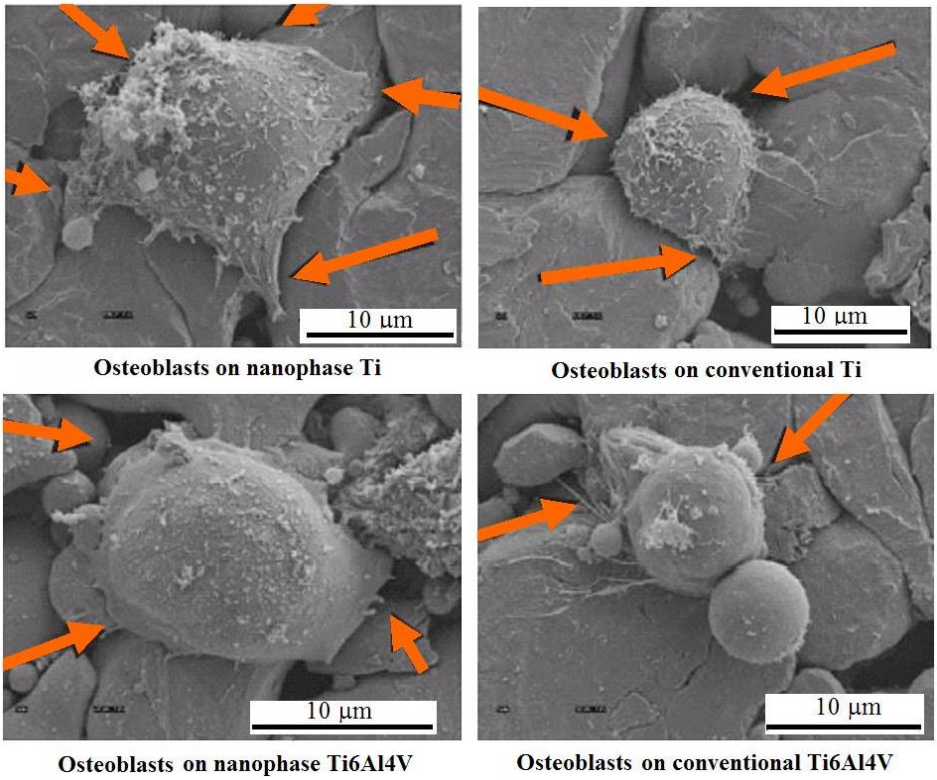

Figure 1.8 SEM images of osteoblasts on nanophase and conventional metals (Ti and Ti6Al4V) after 1 h of cell culture. More osteoblast spreading was observed on nanophase than conventional metals. Arrows point particle boundaries where cell protrusions are seen. This figure is adapted and redrawn from [60].

1.4.3 Nanopolymers

Polymers are a class of synthetic materials characterized by their high versatility and, thus, have been widely applied in orthopedics. They can mechanically secure components of hip replacements into bone (as in bone cements, such as injectable polymethylmethacrylate (PMMA)) and can line acetabular cups for smooth articulation with metallic femoral head components (such as in UHMWPE). However, there also exist many disadvantages related to traditional polymers used in orthopedic applications. For example, PMMA suffers from fatigue-related cracking and impact-induced breakage due

to its poor setting and fixation [64]. Furthermore, PMMA can also elicit a host response due to the release of toxic monomers and necrosis of the surrounding tissue caused by exothermic polymerization in vivo [65]. Increased articulation-induced wear of UHMWPE frequently leads to osteolysis [66].

Therefore, further development of polymer alternatives that could improve osseointegration is necessary, not only for fracture fixation but also as bone tissue engineering scaffolds. For this reason, polymers (such as polylactic acid (PLA), polyglycolic acid (PGA), poly(lactic-co-glycolic acid) (PLGA), poly(l-lactic acid) (PLLA) and various hydrogels) currently generate more interest from tissue engineers to repair bone defects due to their excellent biocompatibility, suitable mechanical properties, biodegradability and ease of modifications. An ideal bone repair scaffold should be biocompatible to minimize local tissue responses but maximize osseointegration. As will be described, an important consideration in polymeric tissue engineering scaffold design is to implement a nanoscale roughness for promoting cellular interactions.

PLGA and its homopolymer derivatives, PLA and PGA are common biodegradable polymers used for bone tissue engineering and orthopedic applications. They have reasonable biocompatibility properties, are FDA approved, have the ability to degrade into harmless monomer units, and are useful for a range of mechanically demanding situations (depending on the copolymer ratio). Various techniques (such as particulate leaching, textile technologies or three-dimensional (3-D) printing techniques) have successfully created three dimensional porous matrices from PLGA and its derivatives

[67-71]. For instance, with the simplicity of a polymer casting and phase separation process, a robust nanofibrous PLLA scaffold can be prepared [71]. These nanofibrous scaffolds have a collagen-like 3-D structure, high porosity and suitable surface structures for osteoblast attachment, proliferation, and differentiation.

In addition, several studies have shown that nanostructured PLGA prepared by chemical etching procedures can promote vascular endothelial and smooth muscle cell adhesion compared to the conventional PLGA [72-73]. Further investigation demonstrated that nanostructured PLGA can adsorb significantly more vitronectin and fibronectin from serum compared to conventional PLGA (just as the aforementioned nanoceramics and nanometals did) [74]. This increase in protein adsorption may help explain the enhanced cell adhesion observed on PLGA with nano-surface roughness. In addition, significantly increased chondrocyte functions (such as adhesion, proliferation and matrix synthesis) have been observed on NaOH-treated nanostructured PLGA [75]. At the same time, it was found that fibroblast density decreased on nanophase PLGA, polyurethane and polycaprolactone which may inhibit the formation of a fibrous tissue capsule [76]. Obviously, these nanostructured PLGA materials have excellent cytocompatibility properties (above that of traditional PLGA) and ease of degradability for improved numerous tissue engineering applications.

Furthermore, polymeric hydrogels have reasonable biocompatibility properties that make them useful in bone tissue engineering applications. For example, since the first reported biomedical potential of poly(2-hydroxyethyl methacrylate) (pHEMA) by Wichterle and

Lim in 1960 [77], pHEMA (a chemically crosslinked hydrogel) has been one of the most widely used hydrogels as a biomaterial for tissue repair surgery, bone or dental applications, drug delivery devices and corneal implants [78-82]. pHEMA has reasonable biocompatibility properties, suitable mechanical properties and ease of modification for diverse applications. pHEMA has also been modified to be biodegradable through the action of enzymes by using dextran-modified pHEMA gels [83]. In addition, when pHEMA was prepared by bulk polymerization with low water content, a material with hardness similar to natural bone was created [84]. Moreover, natural hydrogels (such as collagen and gelatin) are the main components of the ECM of mammalian tissues including bone and cartilage [85]. Through a technique called electrospinning, nanofibrous scaffolds can be successfully created from these synthetic and natural polymers. Several studies have shown that bone cell functions are promoted by electrospun nanofibrous scaffolds that biomimetic the ECM [86-88]. For instance, Venugopal and colleagues electrospun a fibrous nanocomposite of PCL/HA/gelatin at a ratio of 1:1:2. The results demonstrated that osteoblast proliferation, alkaline phosphatase activity and mineralization were highest on the highly flexible PCL/HA/gelatin nanocomposite when compared to other PCL nanofibrous scaffolds [86]. Recently, Osathanon et al. developed a novel polymer/calcium phosphate composite for bone tissue engineering. These nanofibrous fibrin-based composites promoted osteoblast alkaline phosphatase activity as well as osteoblast marker gene (mRNA) expression to support bone maturation both in vitro and in vivo in a mouse calvarial defect model [87].

1.4.4 Carbon Nanotubes and Nanofibers

With the rapid development of carbon nanotube/nanofiber (CNT/CNF) production technologies, CNTs/CNFs with nanometer to millimeter lengths (Figure 1.9) and 1-100nm widths can be prepared [89-90]. Especially, due to their superior cytocompatibility, mechanical and electrical properties, CNTs and CNFs have been incorporated into current natural or synthetic polymers (such as collagen, PGA, etc.) and ceramic (such as HA) scaffolds for orthopedic and bone tissue engineering applications [90-95]. These novel cytocompatible nanotube/nanofiber composites not only overcome the disadvantages of poor mechanical properties of polymer or ceramic scaffolds [95] but they also have improved electrical conductivity properties which contribute to new bone formation under electrical stimulation [96].

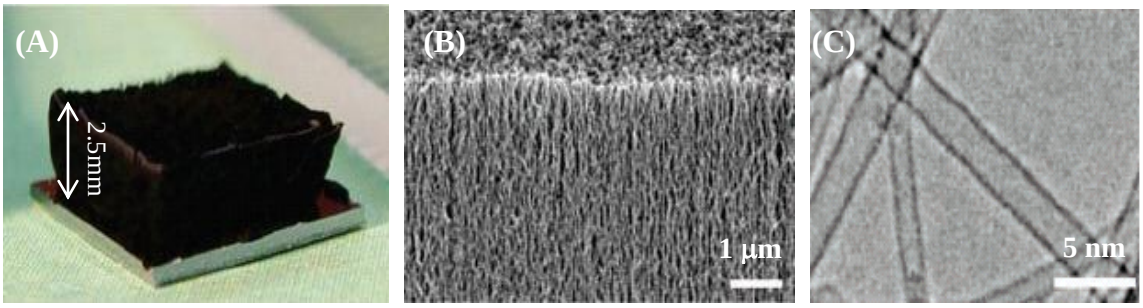

Figure 1.9 High purity and densely aligned single wall carbon nanotube (SWCNT) forests grown with novel water-assisted chemical vapor deposition. The water assisted CVD method can be highly efficient to synthesize highly ordered CNTs (even in 10 min). (A) A SWCNT forest 2.5 mm in height on a 7 mm × 7 mm silicon wafer. (B) Scanning electron microscopy of the SWCNT forest ledge. (C) High-resolution transmission electron microscopy image of the SWCNTs. This figure is adapted from [89].

From a cytocompatibility point of view, there is increasing research showing the promise of CNTs, CNFs and their composites for orthopedic applications [97-102]. For example,

Elias et al. reported that osteoblast proliferation and long-term functions (i.e., synthesis of alkaline phosphatase and deposition of extracellular calcium for up to 21 days) were significantly improved on 60 nm diameter CNFs without a pyrolytic outer layer and 100 nm diameter CNFs with a pyrolytic outer layer when compared to conventional larger carbon fibers [97]. The enhanced long-term osteoblast functions on CNFs have been attributed to their unique nanometer surface topography that mimics the dimension of inorganic crystalline HA and collagen found in natural bone. Further investigations showed not only that nanometer dimension but also that surface energy and chemistry played some role in promoting osteoblast functions on CNFs. In the report, Price et al. demonstrated that 60 nm diameter CNFs significantly increased osteoblast adhesion and concurrently decreased competitive cell (fibroblast, smooth muscle cell, etc.) adhesion in order to stimulate sufficient osseointegration [98]. Other research efforts have also demonstrated that CNTs are suitable to promote osteoblast functions [99]. Recently, Sitharaman and colleagues reported an in vivo study on ultra-short SWCNT polymer nanocomposites after implanting them into rabbit femoral condyles and subcutaneous pockets for up to 12 weeks [100]. The nanocomposites exhibited favorable hard and soft tissue responses after 4 and 12 weeks. They induced a 307% greater bone volume than all other experimental groups after 4 weeks and 200% greater bone growth at defect sites than control polymers without CNTs after 12 weeks. In addition, a study on the cytocompatibility properties of polycarbonate urethane CNF composites demonstrated that osteoblast adhesion was promoted on nanocomposites while a decreasing trend of fibroblast adhesion was observed on these composites with increasing CNF weight ratios in the polymers [101]. Another report observed increased osteoblast and decreased

fibroblast adhesion on PLGA casts of CNFs, highlighting the importance of nanoscale roughness provided by CNTs for orthopedic applications [102].

Moreover, numerous SWCNTs or multi-wall carbon nanotubes (MWCNTs) have been covalently bonded to a wide range of functional groups which make them exhibit excellent candidates for bone tissue engineering applications [103-105]. Specifically, Zhao et al. evaluated HA nucleation and crystallization on the surface of SWCNTs functionalized with phosphonates and poly(aminobenzene sulfonic acid) (PABS) when placed in a solution including $CaCl_2$ and Na_2HPO_4 [104]. Scanning electron microscopy images showed that the functionalized SWCNTs attracted more HA self-assembly on CNTs as collagen did in natural bone. After 14 days of mineralization, the thickness of well aligned HA on functionalized SWCNTs can be over 3 μm. Aryal and colleagues also observed a hierarchy assembly and nucleation of HA crystals on carboxylated MWCNTs after a 7 day incubation in simulated body fluid [105]. Changing the temperature and incubation time can yield different sizes of HA on CNTs. Other research showed that neutrally charged CNTs were suitable to promote osteoblast proliferation and other bone forming activities [99]. In summary, all of these experimental results provide insights into the capability of CNFs/CNTs to serve as biologically inspired scaffold materials to stimulate new bone growth for bone tissue engineering and orthopedic applications.

From a mechanical property point of view, CNTs/CNFs are known as one of the strongest while light weight materials to reinforce bone tissue engineering scaffolds. For example, Shi and colleagues investigated the mechanical properties of an injectable SWCNT

reinforced poly(propylene fumarate) composite [107]. Their results showed that low concentrations of 0.05 wt% SWCNTs dispersed well in uncrosslinked polymer matrices (which have the most potential to enhance mechanical properties of the composites) and high concentrations of 0.2 wt% SWCNTs aggregate in polymers. The aggregation state can damage and decrease the mechanical properties of nanotube polymer composites because applied loads can not effectively transfer in aggregated nanotube reinforced polymer systems. Consequently, it has been demonstrated that a good dispersion of CNTs in poly(propylene fumarate) played a critical role in significant mechanical reinforcement. In another report, MWCNTs, SWCNTs and carbon nanofibrils have been dispersed into a PMMA matrix which is one of the most studied polymers for nanotube composite systems and can mechanically secure the components of the hip replacement device into bone as bone cement [108]. The impact strength (indirectly, the fracture toughness) was significantly improved by SWCNTs. The mechanical properties of the carbon nanofibril and PMMA composites were significantly improved in the study. Moreover, chemically functionalized MWCNTs have provided to great increases in tensile strength and storage modulus when incorporated into polymer matrices considering that load transferring is more effective through chemical bonds [92, 109].

Clearly, there are many researchers dedicated to using CNFs as bone implant material reinforcements and achieving better mechanical properties. For example, Kobayashi et al. showed that CNFs can be used to improve (1.6 times) fracture toughness of HA and the novel CNF/HA exhibited bending strengths similar to cortical bone [110]. It has been observed that the bioactivity of CNF/HA is equal to HA alone when soaking them into

stimulated body fluid. In this manner, CNTs/CNFs as reinforcements in polymer and ceramic scaffolds for bone tissue engineering applications are promising in the design of extremely strong, high porosity matrices to support bone cell adhesion, invasion, and differentiation [91].

From an electrical point of view, CNT/CNF reinforced polymer nanocomposites have also demonstrated excellent electrical conductivity for bone tissue regeneration. It is well known that electrical stimulation can promote osteogenesis at bone fracture sites experimentally and clinically [111-112]. However, traditional methods which have used metal electrodes (i.e., titanium and stainless steel) [113] have disadvantages of inducing secondary surgery to remove electrodes; this may trigger complications (such as infection and loss of osseointegration) [114]. In addition, it is important to note that sometimes electrical stimulation can not effectively promote new bone growth at the entire bone damaged site. For these reasons, much research is focused on the fabrication of novel alternative nanocomposites by incorporating conductive CNTs/CNFs to electrically stimulate bone healing. Just taking biodegradable PLA/CNT composites as an example, the nanocomopsites (specifically, 80/20% (w/w) PLA/CNT) have good conductivity properties while PLA is an insulator [115]. It has been shown that osteoblast proliferation on PLA/CNT composites can be promoted 46% after applying an alternating electrical current for 6 hours each of 2 days and calcium content in the ECM can be increased above 300% after electrical stimulation for 21 days [115]. In summary, all of these studies indicated that the CNTs/CNFs and their composites can serve as osteogenic scaffolds with good cytocompatibility properties, reinforced mechanical properties and improved

electrical conductivity to effectively enhance bone tissue growth.

1.4.5 Self-Assembly Nanotubes and Nanofibers

The last types of nanomaterial to be studied for orthopedic applications are self-assembled materials. Because collagen in bone and cartilage is a nanostructured self-assembled helix, a bottom-up self-assembly process to design novel biomimetic nanofibrous or nanotubular scaffolds has attracted a lot of interest in the bone regeneration community. For instance, Hartgerink et al. reported that a peptide-amphiphile (PA) with the cell-adhesive ligand RGD self-assembled into supramolecular nanofibers [116]. By directly nucleating and aligning HA on the long axis of a nanofiber, a new nanofiber composite was designed with the same self-assembly pattern as collagen and HA crystals in bone. Moreover, Hosseinkhani et al. investigated mesenchymal stem cell (MSC) behavior on self-assembled PA nanofiber scaffolds [117]. Significantly enhanced osteogenic differentiation of MSC occurred in the 3-D PA scaffold compared to 2-D static tissue culture. RGD modified PA nanofibers promoted the maximum amount of alkaline phosphatase activity and osteocalcin content by osteoblasts.

Furthermore, a new class of rosette nanotubes (specifically, RNTs, most of them own the helical structure, thus also named as helical rosette nanotubes (HRNs)) were obtained through the self-assembly of low-molecular-weight synthetic molecules in aqueous solutions. In designing RNTs, the DNA base pair building blocks (Guanine^Cytosine,

G^C) possess key elements for their sequential self-assembly towards the formation of stable nanotubular architectures [118-121]. Figure 1.10A highlights the G^C motif of one type of RNTs, which possesses the Watson-Crick H-bond donor-donor-acceptor array of guanine and acceptor-acceptor-donor array of cytosine central to the self-assembly of RNTs. An amino acid side chain (lysine, K) has been chosen to impose chirality (such as handedness) and surface chemistry on the RNTs. Furthermore, six G^C motifs undergo spontaneous self-assembly under physiological conditions first into a supermacrocycle resembling a rosette (Figure 1.10B). Then, through non-covalent interactions such as H-bonds, base stacking interactions and hydrophobic effects, the rosettes form a stable tubular stack with a hollow core 11 Å in diameter (Figure 1.10C).

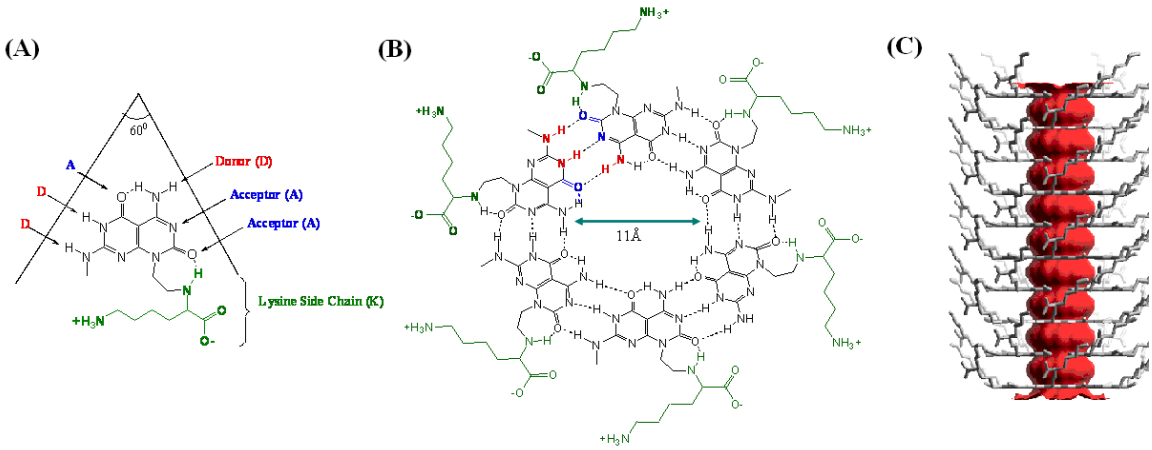

Figure 1.10 Self-assembly of helical rosette nanotubes with a lysine side chain (HRN-K or RNT-K). (A) Guanine^Cytosine motif and K module. (B) Rosette supermacrocycle formed by six G^C motifs maintained by 18 H-bonds. (C) Rosette nanotube with a 3.5 nm diameter and up to several μm in length.

In addition, it is possible to further functionalize the outer space of the G^C motif in order to yield predefined chemical and physical properties for specific tissue

regenerations. For example, the amino acid side chain of RNTs can be possibly replaced by RGD or KRSR (lysine-arginine-serine-arginine), peptide sequences known to enhance cell functions. The RNTs functionalized with different peptide side chains may possibly resemble an environment more favorable to osteoblasts than currently used, non-modified conventional orthopedic materials. Moreover, other bone growth factors or specific peptide sequences which can enhance osteoblast adhesion can possibly attach on the RNTs. The special surface chemistry of RNTs can achieve a strong and robust bonding between the implant and juxtaposed bone for their long-term success of orthopedic implants. In previous study, Chun et al. demonstrated that osteoblast adhesion was greatly enhanced by the RNT-K coated titanium compared to uncoated titanium even at a very low concentration of 0.005 mg/mL [118]. Furthermore, they found RNT-K formed a dense nanotube network after heating or adding to serum free medium [119]. Recently, Journeay et al. reported an in vivo inflammatory study on the RNTs [120]. The results demonstrated that RNTs have low acute toxicity in vivo: i.e., 5 μg dose of RNTs did not trigger an inflammatory response and even with a 50 μg dose, inflammation was resolved after 7 days. Therefore, with such excellent cytocompatibility, flexible design and synthetic accessibility, RNTs are very well suited for orthopedic and bone tissue engineering applications.

In conclusion, the self-assembly nanotubular or nanofibrous materials not only own the nanostructure features like other nanoceramics, nanometals, nanopolymers and CNTs/CNFs, but also mimic the natural hierarchical self-assembly and supramolecular organization of bone. Thus, they hold great promise for bone tissue engineering and

orthopedic applications.

1.5 Objectives

Due to the advantages and promises of the self-assembled RNTs and other types of nanomaterials mentioned above, the main goal of this dissertation was to synthesize, design and fabricate novel biomimetic nanostructured scaffolds or coating materials based on RNTs, nanocrystalline HA as well as hydrogels (specifically, poly(2-hydroxyethyl methacrylate), pHEMA) and test their cytocompatibility for bone tissue engineering and orthopedic applications. Moreover, the potentials of RNTs as coating materials for vascular stent applications were investigated as well. The specific objectives of this in vitro study included:

- Design of novel nanostructured RNTs functionalized with different groups (K and RGD) in hydrogel scaffolds for injectable bone tissue engineering applications.
- Synthesize and characterize nanocrystalline HA and incorporate them into RNTs in hydrogels or coated with RNTs on titanium for improving orthopedic implants.
- Investigate osteoblast adhesion on RNTs in hydrogels and nanocrystalline HA/RNTs in hydrogels or coated on titanium.
- Investigate long-term osteoblast responses (such as proliferation, calcium deposition, protein synthesis and alkaline phosphatase activity) on various RNTs in hydrogels and coated on titanium.
- Modify RNTs with KRSR peptides and investigate osteoblast and fibroblast

adhesion on the novel nanotubes coated on titanium compared to RNTs functionalized with K and RGD coated on titanium for orthopedic applications.

- Determine the role of surface chemistry, surface roughness and surface wettability of RNTs on osteoblast functions.
- Determine endothelial cell adhesion and proliferation on RNTs coated on conventional vascular materials (specifically, titanium) for potential vascular stent applications.

1.6 References

[1] Charnley J. Anchorage of the fermoral head prosthesis to the shaft of the femur. Journal of bone joint surgery 1960;42B:28–30.

[2] Charnley J. Surgery of the hip-joint: present and future developments. Br. Me. J. 1960;5176:821–826.

[3] National Center for Health Statistics (NCHS), online: http://www.cdc.gov/nchs/

[4] Frankowski JJ, Watkins-Castillo S. Primary total knee and hip arthroplasty projections for the U.S. population to the year 2030. American Academy of Orthopedic Surgeons, reviewed by Sculco T P and Sporer SM, August 23, 2002.

[5] American Academy of Orthopedic Surgeons® (AAOS), online: http://www.aaos.org/research/research.asp

[6] Burg KJL, Porter S, Kellam JF. Biomaterial developments for bone tissue engineering. Biomaterials 2000;21:2347–2359.

[7] Summers BN, Eisenstein SM. Donor site pain from the ilium. A complication of lumbar spine fusion. J. Bone Jt. Surg. Br. 1989;71-B:677–680.

[8] Younger EM, Chapman MW. Morbidity at bone graft donor site. J. Orthop. Trauma 1989;3:192–195.

[9] Bozic KJ, Rubash HE, Berry J, Saleh KJ, Durbhakula SM. Modes of failure in revision hip and knee replacement.

[10] Revisions of hip and knee replacements in Canada, Canadian joint replacement registry analytic bulletin: Canadian Institute for Health Information, 2004:1–20.

[11] Branemark PI, Adell R, Albrektsson T, Lekholm U, Lundkvist S, Rockler B. Osseointegrated titanium fixtures in the treatment of edentulousness. Biomaterials 1983;4:25–28.

[12] Esposito M, Hirsh JM, Lekholm U, Thomsen P. Biological factors contributing to failures of osseointegrated oral implants (I): Success criteria and epidemiology. European Journal of Oral Sciences 1998;106:527–551.

[13] Esposito M, Hirsh JM, Lekholm U, Thomsen P. Biological factors contributing to failures of osseointegrated oral implants (II): Etiopathogenesis. European Journal of Oral Sciences 1998;106:721–764.

[14] Wennerberg A, Hallgren C, Johansson C, Danelli S. A histomorphometric evaluation of screw-shaped implants each prepared with two surface roughnesses. Clin. Oral Implants Res. 1998;9:11–19.

[15] Webster TJ, Siegel RW, Bizios R. Osteoblast adhesion on nanophase ceramics. Biomaterials 1999;20:1221–1227.

[16] Castner DG, Ratner BD. Biomedical surface science: Foundations to frontiers. Surface Science 2002;500:28–60.

[17] Webster TJ. Nanophase ceramics: the future orthopedic and dental implant material. In: Ying JY, editor. Advances in chemical engineering. New York: Academic Press, 2001, p.125–166.

[18] Kaplan FS，Hayes WC, Keaveny TM，Boskey A，Einhorn TA, Iannotti JP. Form and function of bone. In: Sinmon SP, editor. Orthopedic basic science. American Academy of Orthopaedic Surgeons, 1994, p.127–185.

[19] Zhu YH, Chiu KY, Tang WM. Review article: polyethylene wear and osteolysis in total hip arthroplasty. Journal of Orthopaedic Surgery 2001;9:91–99.

[20] Harris WH. The problem is osteolysis. Clin. Orthop. 1995;311:46–53.

[21] David V, Jarka N, Olga K. Periprosthetic osteolysis and its association with the molecule RANKL expression. Physiol. Res. 2007;56:455–462.

[22] Bronson JG. Breakthrough technology: searching for artificial articular cartilage. Orthopedic Technology Review 1999;1(1).

[23] Anaheim, Rosemont C. Polyethylene: the past, present and future. In: Orthopaedic proceedings, 66th Annual Meeting, American Academy of Orthopaedic Surgeons. Academy of Orthopaedic Surgeons, 2001, p.445–468.

[24] Zhang LJ, Sirivisoot S, Balasundaram G, Webster TJ. Nanoengineering for bone tissue engineering. In: Khademhosseini A. et al. editors, Micro- and nanoengineering of the cell microenvironment: technologies and applications. Norwood: Artech house, 2008, p.431–460.

[25] Loosening & Osteolysis:Osteolysis (Aseptic Loosening), AAOS online.

[26] D'Antonio J, Capello W, Manley M, Naughton M, Sutton K. Alumina ceramic bearings for total hip arthroplasty. Clinical orthopaedics and related research 2005;436:164–171.

[27] Learmonth ID, Young C, Rorabeck C. The operation of the century: total hip replacement. Lancet 2007;370:1508–1519.

[28] Lindahl H, Garellick G, Regnér H, Herberts P, Malchau H. Three hundred and twenty-one periprosthetic femoral fractures. J. Bone Joint Surg. Am. 2006;88:1215–1222.

[29] Wright TM, Goodman SB. Chapter 22: what are the wear mechanisms and what control them? In: Wright TM, Goodman SB, editors. Implant wear in total joint replacement: clinical and biologic issues, material and design considerations, American Academy of Orthopedic Surgeons, 2001, p.176–185.

[30] Fukushima H, Hashimoto Y, Yoshiya S, et al. Conduction analysis of cement interface temperature in total knee arthroplasty. Kobe J Med Sci 2002;48:63–72.

[31] Learmonth ID. The management of periprosthetic fractures around the femoral stem. J. Bone Joint Surg. Br. 2004;86:13–19.

[32] Herberts P, Malchau H. Long-term registration has improved the quality of hip replacement: a review of the Swedish THR Register comparing 160,000 cases. Acta Orthop Scand. 2000;71;111–121.

[33] Beals RK, Tower SS. Periprosthetic fractures of the femur. An analysis of 93 fractures. Clin. Orthop. Relat. Res. 1996;327: 238–246.

[34] Zhang LJ, Ercan B, Webster TJ. Carbon nanotubes and nanofibers for tissue engineering applications. In: Liu C, editor. Carbon, Research Signpost, 2009, in press.

[35] Vincent J. Materials technology from nature. Metals and Materials, Institute of Materials, 1990.

[36] Smallman RE, Bishop RJ. Modern physical metallurgy and materials engineering-science, process, applications (6th Edition), Elsevier, 1999.

[37] Balasundaram G, Webster TJ. A perspective on nanophase materials for orthopedic implant applications. J. Mater. Chem. 2006;16:3737–3745.

[38] Spencer ND, Textor M. Surface modification, surface analysis, and biomaterials.

[39] Sato M. Nanophase hydroxyapatite coatings for dental and orthopedic applications, PhD Thesis, Purdue University, 2006.

[40] Taniguchi N. On the basic concept of 'nanotechnology', Proc. of International Conference on Precision Engineering (ICPE), Tokyo, Japan, 1974, p. 18–23.

[41] Webster TJ. Editorial foreword. Int. J. of Nanomedicine 2007;2:1–2.

[42] Siegel RW, Fougere GE. Mechanical properties of nanophase metals. Nanostruct. Mater. 1995;6:205–216.

[43] Freeman JW, Wright LD, Laurencin CT, Bhattacharyya S. In: Gonsalves KE, Halberstadt CR, Laurencin CT, Nair LS, Editors, Biomedical nanostructures, John Wiley & Sons, Inc., New Jersey, 2008, p. 3–24.

[44] Fahlman BD. Materials chemistry, Springer, Dordrecht, Netherlands, 2007.

[45] Zhang LJ, Webster TJ. Nanotechnology and nanomaterials: promises for improved tissue regeneration. Nanotoday, 2009;4:66-80.

[46] Chang CK, Wu JS, Mao DL, Ding CX. Mechanical and histological evaluations of hydroxyapatite-coated and noncoated Ti-6Al-4V implants in tibia bone. J. Biomed. Mater. Res. 2001;56:17–23.

[47] Lemons JE. Bioceramics: is there a difference? Clinical Orthopedics and Related Research 1990;261:153–158.

[48] Webster TJ, Ergun C, Doremus RH, Siegel RW, Bizios R. Specific proteins mediate enhanced osteoblast adhesion on nanophase ceramics. J Biomed Mater Res 2000;51:475–483.

[49] Colon G, Ward BC, Webster TJ. Increased osteoblast and decreased Staphylococcus epidermidis functions on nanophase ZnO and TiO2. J Biomed Mater Res A. 2006;78:595–604.

[50] Webster TJ, Ergun C, Doremus RH, Seigel RW, Bizios R. Enhanced osteoclast-like functions on nanophase ceramics. Biomaterials 2001;22:1327–1333.

[51] Chris Arts JJ, Verdonschot N, Schreurs BW, Buma P. The use of a bioresorbable nano-crystalline hydroxyapatite paste in acetabular bone impaction grafting. Biomaterials 2006;27:1110–1118.

[52] Huber F-X, Belyaev O, Hillmeier J, Kock H-J, Huber C, Meeder P-J, Berger I. First histological observations on the incorporation of a novel nanocrystalline hydroxyapatite paste OSTIM® in human cancellous bone. BMC Musculoskeletal Disorders 2006;7:50.

[53] Webster TJ, Hellenmeyer EL, Price RL. Increased osteoblast functions on theta+delta nanofiber alumina. Biomaterials 2005;26:953–960.

[54] Luck M, Paulke BR, Schröder W, Blunk T, Müller RH. Analysis of plasma protein adsorption on polymeric nanoparticles with the different surface characteristics. J. Biomed. Mater. Res. 1998;39:478–485.

[55] Lopes MA, Monteiro FJ, Santos JD, Serro AP, Saramago B. Hydrophobicity, surface tension, and zeta potential measurements of glass-reinforced hydroxyapatite composites. J. Biomed. Mater. Res 1999;45:370–375.

[56] Nukavarapu SP, Kumbar SG, Brown JL, Krogman NR, Weikel AL, Hindenlang MD, et al. Polyphosphazene/nano-hydroxyapatite composite microsphere scaffolds for bone tissue engineering. Biomacromolecules 2008;9:1818–1825.

[57] Affatato S, Torrecillas R, Taddei P, Rocchi M, Fagnano C, Ciapetti G, Toni A. Advanced nanocomposite materials for orthopaedic applications, a long-term in vitro wear study of zirconia-toughened alumina. J. Biomed. Mater. Res. Part B 2006;78B:76–82.

[58] Tanaka K, Tamura J, Kawanabe K, Nawa M, Oka M, Uchida M, Kokubo T, Nakamura T. Ce-TZP/Al2O3 nanocomposite as a bearing material in total joint replacement. J. Biomed. Mater. Res. 2002;63:262–270.

[59] Takemoto M, Fujibayashi S, Neo M, Suzuki J, Kokubo T, Nakamura T. Bone-bonding ability of a hydroxyapatite coated zirconia–alumina nanocomposite with a microporous surface. J. Biomed. Mater. Res. 2006;78A:693–701.

[60] Webster TJ, Ejiofor JU. Increased osteoblast adhesion on nanophase metals: Ti, Ti6Al4V, and CoCrMo. Biomaterials 2004;25:4731–4739.

[61] Puckett S, Pareta R, Webster TJ. Nano rough micron patterned titanium for

directing osteoblast morphology and adhesion. Int. J. Nanomedicine 2008;3:229–241.

[62] Yao C, Perla V, McKenzie JL, Slamovich EB, Webster TJ. Anodized Ti and Ti6Al4V possessing nanometer surface features enhances osteoblast adhesion. J Biomed Nanotechnol 2005;1:68–73.

[63] Burns K, Yao C, Webster TJ. Increased chondrocyte adhesion on nanotubular anodized titanium. J. Biomed. Mater. Res. A. 2008, in press.

[64] Unwin PS. The recent advantages in bone and joint implant technology. In: Ward-Close M, editor. Cost-effective titanium component technology for leading-edge performance, John Wiley & Sons, Inc., New Jersey, 2001.

[65] Dunn MG, Maxian SH. Biomaterials used in orthopedic surgery. In: Greco RS, editor. Implantation biology: The host response and biomedical devices, CRC Press, Inc., 1994, p.229–252.

[66] Davidson JA, Poggie RA, Mishra AK. Abrasive wear of ceramic, metal and UHMWPE bearing surfaces from third-body bone, PMMA bone cement and titanium debris. Biomed. Mater. Eng. 1994;4:213–229.

[67] Coombes AD, Heckman JD. Gel casting of resorbable polymers. Biomaterials 1992;13:217–224.

[68] Devin JE, Attawia MA, Laurencin CT. Three-dimensional degradable porous polymer-ceramic matrices for use in bone repair. J. Biomater. Sci. Polymer Ed. 1996;7:661–669.

[69] Mikos AG, Thorsen AJ, Czerwonka LA, Bao Y, Langer R. Preparation and characterization of poly (l-lactic acid) foams. Polymer 1994;35:1068–1077.

[70] Thompson RC, Yaszemski MJ, Powers JM, Mikos AG. Fabrication of biodegradable polymer scaffolds to engineer trabecular bone. J. Biomater. Sci. Polymer Ed. 1995;7:23–38.

[71] Chen VJ, Ma PX. Nano-fibrous poly(l-lactic acid) scaffolds with interconnected spherical macropores. Biomaterials 2004;25:2065–2073.

[72] Miller DC, Thapa A, Haberstroh KM, Webster TJ, Enhanced functions of vascular and bladder cells on poly-lactic-co-glycolic acid polymers with nanostructured surfaces. IEEE Trans Nanobioscience 2002;1:61–66.

[73] Thapa A, Miller DC, Webster TJ, Haberstroh KM. Nano-structured polymers enhance bladder smooth muscle cell function. Biomaterials 2003;24:2915–2926.

[74] Miller DC, Haberstroh KM, Webster TJ. Mechanism(s) of increased vascular cell adhesion on nanostructured poly(lactic-co-glycolic acid) films. J. Biomed. Mater. Res. A. 2005;73:476–484.

[75] Park GE, Pattison MA, Park K, Webster TJ. Accelerated chondrocyte functions on NaOH-treated PLGA scaffolds. Biomaterials 2005;26:3075–3082.

[76] Vance RJ, Miller DC, Thapa A, Haberstroh KM, Webster TJ. Decreased fibroblast cell density on chemically degraded poly(lactic-co-glycolic acid), polyurethane, and polycaprolactone. Biomaterials 2004;25:2095–2103.

[77] Wichterle O, Lim D. Hydrophilic gels in biologic use. Nature 1960;185:117–118.

[78] Filmon R, Basl é MF, Atmani H, Chappard D. Adherence of osteoblast-like cells on calcospherites developed on a biomaterial combining poly(2-hydroxyethyl) methacrylate and alkaline phosphatase. Bone 2002;30:152–158.

[79] Zavrel V, Štol M. p(HEMA) composite as allografting material during therapy of periodontal disease: three case reports. Biomaterials 1993;14:1109–1112.

[80] Hoffman AS. Hydrogels for biomedical applications. Advanced Drug Delivery Reviews 2002;43:3-12.

[81] Lowman AM, Peppas NA. Hydrogels. In: Mathiowitz E, editor. Encyclopedia of controlled drug delivery, John Wiley & Sons, Inc., 1999, p.397–418.

[82] Schiraldi C, D'Agostino A, Oliva A, Flamma F, et al. Development of hybrid materials based on hydroxyethylmethacrylate as supports for improving cell adhesion and proliferation. Biomaterials 2004;25:3645–3653.

[83] Meyvis TKL, Smedt SCD, Demeester J, Hennink WE. Influence of the degradation mechanism of hydrogels on their elastic and swelling properties during degradation. Macromolecules 2000;33:4717–4725.

[84] Filmon R, Grizon F, Basl é MF, Chappard D. Effects of negatively charged groups (carboxymethyl) on the calcification of poly(2-hydroxyethylmethacrylate). Biomaterials 2002;23:3053–3059.

[85] Lee KY, Mooney DJ. Hydrogels for tissue engineering. Chemical Reviews 2001;101:1869–1879.

[86] Venugopal JR, Low S, Choon AT, Kumar AB, Ramakrishna S. Nanobioengineered electrospun composite nanofibers and osteoblasts for bone regeneration. Artificial Organs 2008;32:388–397.

[87] Osathanon T, Linnes ML, Rajachar RM, Ratner BD, Somerman MJ, Giachelli CM. Microporous nanofibrous fibrin-based scaffolds for bone tissue engineering. Biomaterials 2008;29:4091–4099.

[88] Lia M, Guob Y, Weib Y, MacDiarmidc AG, Lelkes PI. Electrospinning polyaniline-contained gelatin nanofibers for tissue engineering applications. Biomaterials 2006;27:2705–2715.

[89] Hata K, Futaba DN, Mizuno K, Namai T, Yumura M, Iijima S. Water-assisted highly efficient synthesis of impurity-free single-walled carbon nanotubes. Science 2004;306:1362–1364.

[90] Harrison BS, Atala A. Carbon nanotube applications for tissue engineering. Biomaterials 2007;28:344–353.

[91] Wei W, Sethuraman A, Jin C, Riviere NAM, Narayan RJ. Biological properties of carbon nanotubes. J Nanosci Nanotechnol. 2007;7:1–14.

[92] Cui D. Advances and prospects on biomolecules functionalized carbon nanotubes. J Nanosci Nanotechnol. 2007;7:1298–1314.

[93] Saito N, Usui Y, Aoki K, Narita N, Shimizu M, Ogiwara N, Nakamura K, et al. Carbon nanotubes for biomaterials in contact with bone. Curr Med Chem. 2008;15(5):523–527.

[94] Abarrategi A, Gutiérrez MC, Moreno-Vicente C, Hortigüela MJ, Ramos V, López-Lacomba JL, et al. Multiwall carbon nanotube scaffolds for tissue engineering purposes. Biomaterials 2008;29:94–102.

[95] Shi X, Hudson JL, Spicer PP, Tour JM, Krishnamoorti R, Mikos AG. Injectable nanocomposites of single-walled carbon nanotubes and biodegradable polymers for bone tissue engineering. Biomacromolecules 2006;7:2237–2242.

[96] Supronowicz PR, Ajayan PM, Ullmann KR, Arulanandam BP, Metzger DW, Bizios R. Novel current-conducting composite substrates for exposing

osteoblasts to alternating current stimulation. J. Biomedical Materials Research 2002;59:499–506.

[97] Elias KL, Price RL, Webster TJ. Enhanced functions of osteoblasts on nanometer diameter carbon fibers. Biomaterials 2002;23:3279–3287.

[98] Price RL, Waid MC, Haberstroh KM, Webster TJ. Selective bone cell adhesion on formulations containing carbon nanofibers. Biomaterials 2003;24:1877–1887.

[99] Zanello LP, Zhao B, Hu H, Haddon RC. Bone cell proliferation on carbon nanotubes. Nano Lett 2006;6:562–567.

[100] Sitharaman B, Shi X, Walboomers XF, Liao H, Cuijpers V, Wilson LJ, et al. In vivo biocompatibility of ultra-short single-walled carbon nanotube/biodegradable polymer nanocomposites for bone tissue engineering. Bone 2008;43:362–370.

[101] Webster TJ, Waid MC, McKenzie JL, Price RL, Ejiofor JU. Nano-biotechnology: carbon nanofibres as improved neural and orthopaedic implants. Nanotechnology 2004;15:48–54.

[102] Price RL, Ellison K, Haberstroh KM, Webster TJ. Nanometer surface roughness increases select osteoblast adhesion on carbon nanofiber compacts. J Biomed Mater Res 2004;70A:129–138.

[103] Bianco A, Kostarelos K, Partidos CD, Prato M. Biomedical applications of functionalised carbon nanotubes. Chem. Commun. 2005;5:571–577.

[104] Zhao B, Hu H, Mandal SK, Haddon RC. A bone mimic based on the self-assembly of hydroxyapatite on chemically functionalized single-walled carbon nanotubes. Chem. Mater. 2005;17:3235–3241.

[105] Aryal S, Bhattarai SR, Remant Bahadur KC, Khil MS, Lee DR, Kim HY. Carbon nanotubes assisted biomimetic synthesis of hydroxyapatite from simulated body fluid. Materials Science and Engineering A 2006;426:202–207.

[106] Webster TJ, Schadler LS, Siegel RW, Bizios R. Mechanisms of enhanced osteoblast adhesion on nanophase alumina involve vitronectin. Tissue Eng 2001;7:291-301.

[107] Shi X, Hudson JL, Spicer PP, Tour JM, Krishnamoorti R, Mikos A.G.

Rheological behaviour and mechanical characterization of injectable poly(propylene fumarate)/single-walled carbon nanotube composites for bone tissue engineering. Nanotechnology, 2005;16:S531–S538.

[108] Cooper CA, Ravich D, Lips D, Mayer J, Wagner H.D. Distribution and alignment of carbon nanotubes and nanofibrils in a polymer matrix. Composites Science and Technology 2002;62:1105–1112.

[109] Velasco-Santos C, Martinez-Hernandez AL, Castano VM. Carbon nanotube-polymer nanocomposites: The role of interfaces. Composite Interfaces 2005;11:567–586.

[110] Kobayashi, S., and Kawai, W. Development of carbon nanofiber reinforced hydroxyapatite with enhanced mechanical properties. Composites: Part A 38 (2007) 114–123

[111] Brighton CT, Okereke E, Pollack SR, Clark CC. In vitro bonecell response to a capacitively coupled electrical field. Clin Orthop Rel Res 1992;285:255–262.

[112] Zhuang H, Wang W, Seldes RM, Tahernia AD, Fan H, Brighton CT. Electrical stimulation induces the level of tgf-b1 mRNA in osteoblastic cells by a mechanism involving calcium/calmodulin pathway. Biochem Biophys Res Commun 1997;237:225–229.

[113] Black J, Baranowski TJ and Brighton CT. Electrochemical aspects of d.c. stimulation of osteogenesis. Bioelectrochem Bioenergetics 1984;12:323–327.

[114] Bassett CA, Pawluk RJ, Becker RO. Effects of electric currents on bone in vivo. Nature 1964;204:652–654.

[115] Supronowicz PR, Ajayan PM, Ullmann KR, Arulanandam BP, Metzger DW, Bizios R. Novel current-conducting composite substrates for exposing osteoblasts to alternating current stimulation. J Biomed Mater Res 2002;59:499–506.

[116] Hartgerink JD, Beniash E, Stupp SI. Self-assembly and mineralization of peptide-amphiphile nanofibers. Science 2001;294:1684–1688.

[117] Hosseinkhani H, Hosseinkhani M, Tian F, Kobayashi H, Tabata Y. Osteogenic differentiation of mesenchymal stem cells in self-assembled peptide-amphiphile nanofibers. Biomaterials 2006;27:4079–4086.

[118] Chun AL. Helical rosette nanotubes: an investigation towards its application in orthopedics, Ph.D. thesis, Weldon School of Biomedical Engineering, Purdue University, West Lafayette, IN, 2006.

[119] Chun AL, Moralez JG, Webster TJ, Fenniri H. Helical rosette nanotubes: a biomimetic coating for orthopedics. Biomaterials 2005;26:7304–7309.

[120] Journeay WS, Suri SS, Moralez JG, Fenniri H, Singh B. Rosette nanotubes show low acute pulmonary toxicity in vivo. Int J Nanomed 2008;3:373–383.

[121] Fenniri H, Mathivanan P, Vidale KL, Sherman DM, Hallenga K, Wood KV, Stowell JG. Helical rosette nanotubes: design, self–assembly and characterization. J Am Chem Soc 2001;123:3854–3855.

CHAPTER 2

DESIGN OF A CYTOCOMPATIBLE NANOSTRUCTURED ROSETTE NANOTUBE HYDROGEL SCAFFOLD FOR BONE TISSUE ENGINEERING

A portion of this chapter has been published in:

1. **L. Zhang**, F. Rakotondradany, A.J. Myles, H. Fenniri and T.J. Webster. Arginine-Glycine-Aspartic Acid Modified Rosette Nanotube-Hydrogel Composites for Bone Tissue Engineering. *Biomaterials*, 30(7):1309-1320 (2009).
2. **L. Zhang**, S. Ramsaywack, H. Fenniri and T.J. Webster. Enhanced Osteoblast Adhesion on Self-assembled Nanostructured Hydrogel Scaffolds. *Tissue Engineering*, 14(8):1353-1364 (2008).

2.1 Introduction

To date, much of the research in bone tissue engineering has focused on the development of novel nanophase materials (including nanophase polymers, ceramics, and metals, etc.), surface modifications (altering the implant surface topography and chemistry) of currently implanted materials, and the overall design and synthesis of bone-like composites in order to more successfully promote cell adhesion and tissue integration [1]. However, most of the nanomaterials studied so far do not mimic the natural hierarchical self-assembly and supramolecular organization of bone. Thus, it is desirable to design a matrix that can mimic the natural structure of bone and thus enhance osseointegration while providing a scaffold for bone tissue regeneration.

Rosette nanotubes (RNTs) are a type of soft organic nanomaterial obtained through the self-assembly of low-molecular-weight synthetic molecules when placed in water as mentioned in section 1.4.5. RNTs have several unique features that make them attractive for orthopedic and bone tissue engineering applications: (a) rapid and quantitative preparation through self-assembly; (b) biomimetic nanostructured features that improve osteoblast (bone-forming cell) attachment; (c) ability to serve as excellent calcification templates [2]; (d) facile functionalization with amino acid and peptide side chains; (e) well-controlled spatial distributions of the side chains to enhance their functionality [3]; (f) ability to gel when heated or added directly into serum free medium [4] which may allow them to serve as novel injectable materials for bone repair under physiological

conditions; and (g) synthetic accessibility, chemical tunability, and functional group tolerance which impart a broad range of tailorable chemistries and biological properties.

Specifically, the amino acids on the G^C motif of RNTs may be modified with numerous functional groups of different properties [5], thus, making it possible to tailor RNTs for specific tissue engineering applications. Considering that arginine-glycine-aspartic acid (RGD) is a well known cell adhesive domain present in many proteins (including fibronectin, vitronectin and collagen), it is a popular peptide sequence widely studied for improving osteoblast functions. For instance, a wide range of RGD containing peptides (e.g., RGD [6-9], RGDS [10], RGDSP [11,12], RGDFK [13], RGDSGGC [14], GRGD [15], GRGDS [16], GRGDSP [17,18], and GRDSPK [19]) have been immobilized on conventional implant materials (such as titanium and its alloys, hydrogels, and polymers) to improve bone cell functions in vitro and in vivo. For example, Elmengaard et al. showed that bone growth on RGD coated Ti6Al4V implants increased two-fold compared to uncoated implants in the proximal tibia of mongrel dogs for 4 weeks [13]. Recently, Chua et al. also reported that hyaluronic acid/chitosan polyelectrolyte multilayers with RGD immobilized on titanium improved osteoblast functions (such as osteoblast proliferation and alkaline phosphatase activity) by 100%-200% compared to uncoated titanium [8]. Furthermore, bacteria (i.e., *staphylococcus aureus*) functions have been inhibited on titanium coated with RGD functionalized poly(L-lysine)-grafted-poly(ethylene glycol) copolymers [20]. Thus, RGD containing peptides are excellent candidates to be functionalized on RNTs in order to design a more cytocompatible nanomaterial for bone tissue engineering applications.

In the present study, RNTs expressing a mixture of RGD containing peptides (specifically, RGDSK) and K at various concentrations (0%, 1%, 5%, 10% RGDSK to K molar ratios on RNTs, termed RNT-K and RNT-RGD-K, Figure 2.1) were studied for bone tissue engineering applications. Moreover, it should be emphasized that most of the reported efforts involving RGD modification on traditional materials have been carried out on 2-D flat substrates [6-8, 16-20]. It was reasoned that the incorporation of RNTs into a biocompatible hydrogel (specifically, poly(2-hydroxyethyl methacrylate), pHEMA) would result in a biologically-inspired 3-D nanoscale scaffold with self-assembled biomimetic features more suitable for 3-D bone regeneration. pHEMA has been extensively used as a cytocompatible tissue engineering and drug delivery material as mentioned in section 1.4.3. Therefore, by combining RNTs with pHEMA hydrogels, it was anticipated that one could develop a robust and nanostructured orthopedic scaffold with excellent cytocompatibility properties based on favorable surface chemistry.

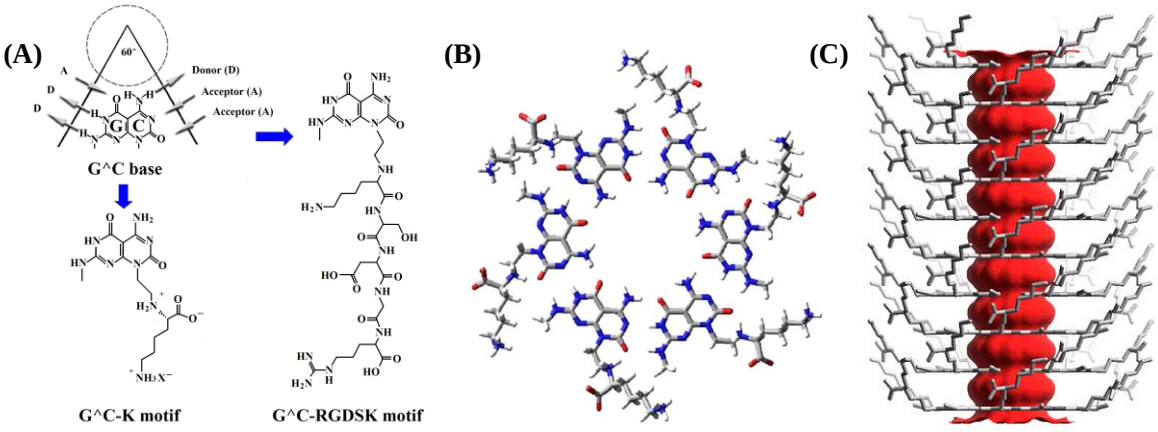

Figure 2.1 Schematic illustration of the self–assembly process of RNT-RGD-K. (A) G^C building blocks, G^C base with lysine side chain (G^C-K, bottom image) and newly synthesized G^C–RGDSK (RGD side chain, right image in (A)); (B) rosette–like

supermacrocycle assembled from six building blocks; and (C) based on hydrophobic, electrostatic and base stacking interactions, rosettes stack up into stable helical nanotubes with a 11 Å hollow core.

2.2 Research Objectives

The objectives of this chapter were to design and investigate the potential of the biologically-inspired K and RGDSK functionalized RNTs placed in hydrogels for bone tissue engineering applications. For this purpose, the RNT-K and 1%, 5%, and 10% RNT-RGD-K were assembled by dissolving different types of G∧C motifs in water; such constructs were further characterized using transmission electron microscopy, scanning electron microscopy, atomic force microcopy, etc. In addition, surface wettability, specific protein (fibronectin) adsorption, osteoblast adhesion and proliferation studies were performed on the various RNTs coated on or embedded in pHEMA hydrogels. Finally, osteoblast responses to the various RNTs hydrogels were compared to those of type I collagen and poly L-Lysine coated hydrogels to understand the mechanism of osteoblast behavior on these new materials. Osteoblast morphology on these materials was also examined to further assess adhesion.

2.3 Materials and Methods

2.3.1 Sample Preparation

2.3.1.1 Preparation of RNTs Functionalized with K and RGDSK

By using the standard peptide synthesis chemistry [5], the G^C-K (lysine side chain) motif was prepared by Sharwatie Ramsaywack from Professor Hicham Fenniri's group at the University of Alberta. Furthermore, the RGDSK modified G^C base (G^C-RGDSK) was synthesized by coupling Wang resin protected RGDSK peptides onto the G^C motif, which was synthesized by Felaniaina Rakotondradany from Prof. Fenniri's lab. Figure 2.2 illustrates the RGDSK coupling onto the G^C motif. The detailed synthesis procedure and characterization data (^{1}H-NMR, ^{13}C-NMR spectra, high resolution ESI-MS and elemental analysis) of the G^C-RGDSK base can be found in [21].

In the current study, 1 mg/mL of RNT with lysine side chains (RNT-K) was prepared by directly dissolving 5 mg of G^C-K building blocks (formed as a white powder) into 5 mL of Millipore distilled and deionized water (ddH_2O). The solution was diluted into various other concentrations including 0.1 mg/mL, 0.01 mg/mL and 0.001 mg/mL RNT-K in ddH_2O. For the RNT-RGD-K formulation, 1%, 5% and 10% molar ratios of RGD to K on RNTs were prepared. Specifically, G^C-RGDSK and G^C-K building blocks were co-dissolved in ddH_2O at molar ratios of 1%, 5% and 10% to achieve 0.1 mg/mL

stocking solutions of 1%, 5% and 10% RNT-RGD-K. Then, these stock solutions were diluted with ddH_2O to achieve 0.01 mg/mL RNT-RGD-K solutions. All of the RNT solutions were sterilized by filtration through a 0.22 μm syringe filter to remove any debris and contamination.

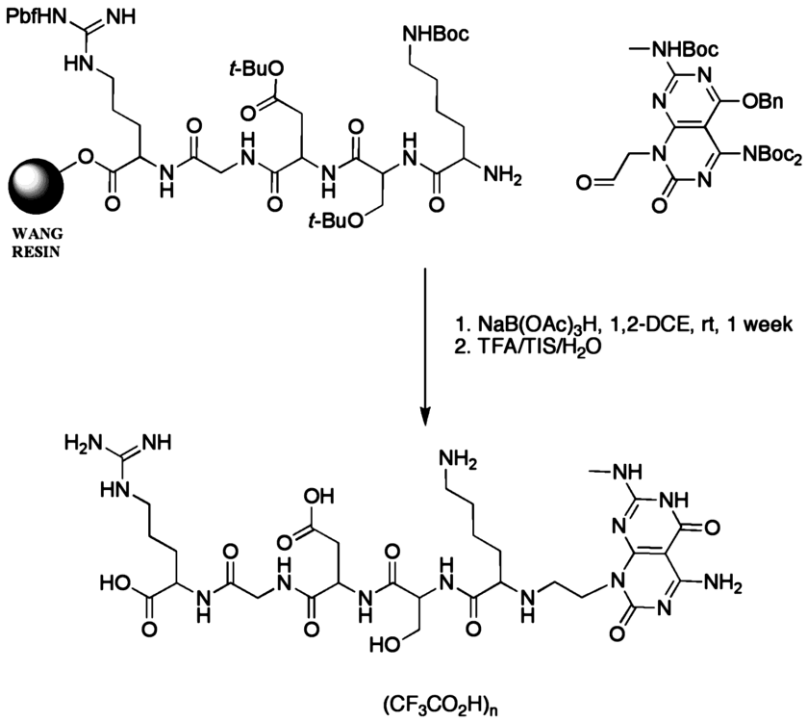

Figure 2.2 A synthetic scheme of Wang resin–supported protected RGDSK peptide coupling onto the G^C base.

2.3.1.2 Fabrication of RNT Hydrogel Scaffolds

The RNTs were then embedded in and coated on pHEMA hydrogels. For the RNTs embedded in hydrogels, 4 mL of the 2-hydroxyethyl methacrylate (HEMA) monomer (Polysciences Inc., PA) was combined with 4 mL of the RNT-RGD-K (0.01 mg/mL of

1%, 5% and 10%) or RNT-K (0.01 and 0.001 mg/mL) solutions in a 10 mL vial. Then, 8 mg of a 2, 2'-azobisisobutyronitrile (Sigma-Aldrich, MO) free radical initiator was added at a concentration of 0.1% w/w (based on the weight of the monomer mixture) [22-24]. The mixture was blended mechanically in order to obtain a homogenous solution, which was then poured into a 10 mL glass beaker and heated in an oven at 78 ℃ for 50~60 min to polymerize. At lower temperatures (such as room temperature), the reaction proceeded slowly and took several days; at higher temperatures (such as above 85℃), the polymerization proceeded too fast and generated undesirable bubbles in the pHEMA. When the polymerization was complete, the beaker was removed from the oven and the gel was easily removed from the beaker. Once removed, the cylindrical hydrogel nanocomposites were placed in a Petri dish and cross sectioned into small samples 1.8 cm in diameter and 2 mm thick for further testing (Figure 2.3A). In addition, the changes in gelling time of the hydrogels after adding RNTs were investigated in this study.

Hydrogels without RNTs served as controls, which were prepared by replacing the RNT solution mentioned in the above procedure with ddH_2O. For preparing RNT coated hydrogels, the hydrogel controls were coated with either RNT-RGD-K (0.01 mg/mL of 1%, 5% and 10%) or RNT-K (0.01 and 0.001 mg/mL) by simple adsorption at room temperature for 45 min (Figure 2.3B). All of the resulting hydrogel nanocomposites and controls were soaked in sterile ddH_2O at room temperature for at least 30 min to remove unreacted residual monomers [25]. Then, various RNT hydrogels and controls were sterilized in a 70% ethanol solution for 15 min, air dried overnight and rinsed with phosphate buffered saline (PBS) prior to cell culture experiments.

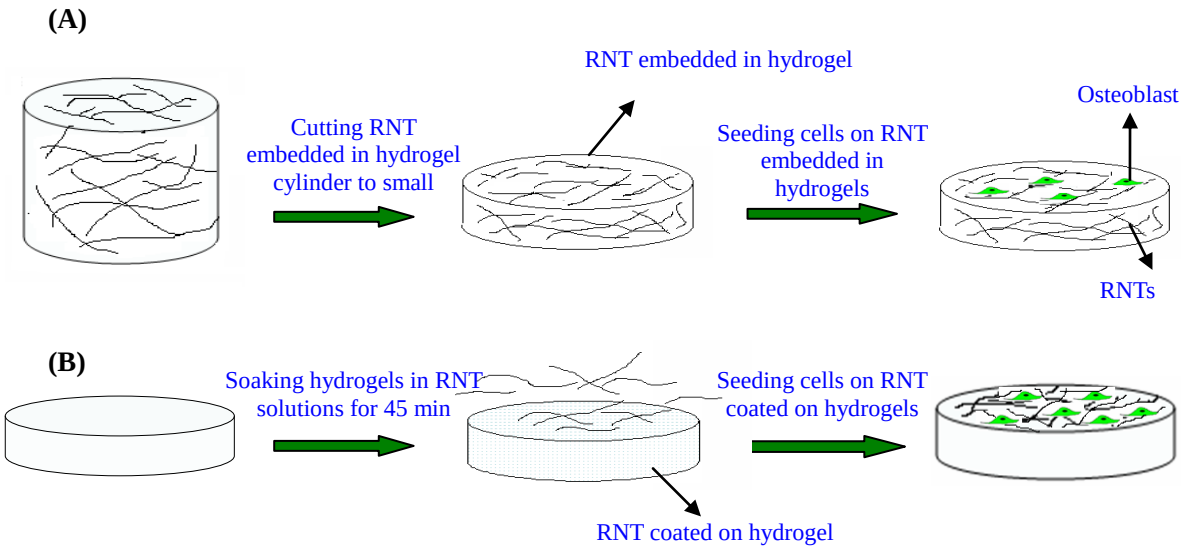

Figure 2.3 Schematic illustration of various RNT hydrogels and osteoblast adhesion on these scaffolds (not drawn to scale). (A) RNTs embedded in hydrogels and (B) RNTs coated on hydrogels.

Lastly, borosilicate glass coverslips (GL) were adopted as a reference substrate in this study. They were degreased in acetone for 15 min, sonicated for another 15 min, and then rinsed three times with ddH_2O. Similarly, they were also soaked in 70% ethanol, sonicated for 15 min and rinsed with ddH_2O, then, soaked and sonicated for another 15 min and thoroughly rinsed with ddH_2O. The glass was furthur etched in 1 M NaOH for 1 h and rinsed. After separating GL with sharp tip tweezers, they were placed in an oven at 80 ℃ overnight and autoclaved under high temperature and pressure (254-259 ℉; 17-20 psi) for at least 35 min for sterilization purposes before cell experiments.

2.3.2 Characterization of RNTs and RNT Hydrogel Scaffolds

2.3.2.1 Transmission Electron Microscopy (TEM)

TEM was utilized to examine the morphology of the various RNTs (specifically, 0.1 mg/mL of 1%, 5% and 10% RNT-RGD-K as well as 3.3 mg/mL, 0.1 mg/mL and 0.01 mg/mL of RNT-K) in water and in hydrogels. For this purpose, a carbon-coated 400-mesh copper grid (EM Sciences, PA) was floated on the viscous RNT hydrogel mixtures for 2 min, which was removed from the oven when polymerization proceeded for 40 min at 45 ℃. For RNTs in water, a copper grid was placed on a droplet of RNT solution for 2 min to adsorb nanotubes. All of the samples, then, were placed on a droplet of 2% aqueous uranyl acetate (EM sciences, PA) for 20 s in order to remove any non-adherent RNTs. They were transferred to a second droplet of 2% aqueous uranyl acetate for 20 s to be negatively stained. The negatively stained RNT hydrogel coated grids were then blotted and dried with filter paper. TEM (Philips, EM410 PW6008, Dutch) images were recorded at 10,000×~235,000× operating at 100 or 120 kV acceleration voltages. Similarly, hydrogel controls without RNTs were imaged under TEM for comparison purposes.

In addition, in order to image the RNT morphology in the fully polymerized hydrogels, two fully polymerized hydrogel scaffolds (0.01 mg/mL RNT-K embedded in hydrogels and hydrogel controls) were fixed in 2% glutaraldehyde (EM Sciences, PA) in PBS at a pH of 7.2 for 2 h. After washing 3 times in PBS, specimens were post-fixed in 2% osmium tetroxide overnight. Then, specimens were washed 3 times in ddH_2O. After dehydration through a graded series of ethanol solutions, specimens were embedded in

Spurr's resin (EM Sciences, PA) at 65 ℃ in a mold. Thin sections (80-90 nm thick) were cut by a Reichert-Jung ultramicrotome and retrieved onto uncoated TEM grids. The grids were imaged at 31,000 × on a TEM at an acceleration voltage of 80 kV.

2.3.2.2 Scanning Electron Microscopy (SEM) and Atomic Force Microscopy (AFM)

Scanning electron microscopy (SEM, LEO 1530-VP) and tapping mode atomic force microscopy (TM-AFM, Dimension 3100, Veeco Instruments, USA) were used to characterize surface topography of RNT hydrogel scaffolds and hydrogel controls. For SEM, the RNT hydrogels and controls were completely dehydrated in an oven at 50 ℃ for 2 days, and were sputter-coated with a thin layer of gold–palladium using a PS-2 coating unit (International Scientific Instruments) in an argon environment for 3 min. They were imaged at an accelerating voltage of 10 kV and 3 kV.

Since the solidified hydrogel surface was too rough to image the RNTs directly under the AFM, a thin layer of hydrogel was coated on glass coverslips and next, RNTs were coated on the hydrogel and imaged under the AFM. To accomplish this, glass coverslips were cleaned by the method mentioned in section 2.3.1.2. They were coated by placing a thin film of viscous hydrogel which was removed from the partly liquid-like hydrogel scaffolds (more than 60% polymerized). Then, they were placed back into the oven to complete the polymerization. The dried hydrogel coated glass coverslips were further coated with a 1.3 mg/mL RNT-K solution by simple adsorption at room temperature for 45 min. The samples were air-dried and imaged by AFM in tapping mode at a scan rate of

1 Hz per line using an ultrasharp silicon cantilever with a radius of curvature less than 10 nm (NSC15/Al BS, MikroMasch, USA).

2.3.2.3 Water Absorption and Equilibrium Water Content Measurements

For water absorption measurements, different concentrations of RNT-K embedded in hydrogels (0.01 mg/mL and 0.001 mg/mL) and hydrogel controls were maintained in ddH_2O, exchanged daily for up to 11 days. Then, the residual surface water was blotted with filter paper and each sample was weighed in order to measure the hydrated scaffold weight ($W_{hydrated}$). Next, samples were dried in an oven at 50 ℃ over a 2 day period. Each scaffold was then weighed again to obtain the dry weight (W_{dry}). The water absorption (WA) of the hydrogel was calculated according to the following equation:

$$WA\% = \frac{(W_{hydrated} - W_{dry})}{W_{dry}} \times 100 \quad (1)$$

In addition, equilibrium water content (EWC), which is water absorption for a fully hydrated hydrogel, was collected ($W_{hydrated}$) after 11 days and calculated according to the above equation. Furthermore, water content changes in scaffolds during polymerization at 45 ℃ were measured as well.

Moreover, the swelling behavior of a variety of RNTs at the same concentration in hydrogels was also measured at room temperature for a period up to 18 days compared to controls. 0.01 mg/mL 1%, 5% and 10% RNT-RGD-K and RNT-K embedded in hydrogels as well as controls were immersed in ddH_2O which was exchanged daily. At select time

points (1, 2, 4, 6, 8, 10, 12, and 18 days), $W_{hydrated}$ was measured as described above. Similarly, after drying for two days at 50 ℃, the dry hydrogel weight was obtained by weighing hydrogels and the EWC values were calculated after 18 days.

2.3.3 Cytocompatibility Studies

2.3.3.1 Osteoblast Culture

A human fetal osteoblast cell line (ATCC, CRL-11372, VA) was cultured in Dulbecco's modified eagle's medium (DMEM, Invitrogen Corporation, USA) supplemented with 10% fetal bovine serum (FBS, Hyclone, UT) and 1% penicillin/streptomycin (P/S, Hyclone, UT) under standard cell culture conditions (37 ℃, a humidified, 5% CO_2/95% air environment). Cells were used up to population numbers of 8-11 in the experiments without further characterization.

2.3.3.2 Osteoblast Adhesion

For investigating the cytocompatibility properties of different concentrations of RNT-K hydrogels, osteoblast adhesion was tested on five types of substrates: #1) 0.01 mg/mL RNT-K coated on hydrogel scaffolds, #2) 0.01 mg/mL RNT-K embedded in hydrogel scaffolds, #3) 0.001 mg/mL RNT-K embedded in hydrogel scaffolds, #4) 0.001 mg/mL RNT-K coated on hydrogel scaffolds, and #5) uncoated hydrogels. In addition, osteoblast adhesion on different types of RNT hydrogels, including 0.01 mg/mL of 1%, 5% and

10% RNT-RGD-K as well as 0.01 mg/mL RNT-K embedded in and coated on hydrogels, was determined and compared to hydrogel controls without RNTs.

Osteoblasts were seeded at a density of 3500 cells/cm^2 and were cultured under standard cell culture conditions for 4 h. Then, the substrates were rinsed using PBS to remove non-adherent cells and the remaining cells were fixed using 10% normal buffered formaldehyde (Fisher Scientific) for 10 min and 0.1% Triton X-100 (Sigma-Aldrich, MO) for 5 min. Osteoblasts were then stained with rhodamine-phalloidin (staining F-actin filaments, Molecular Probes) to examine cell spreading and were further stained with DAPI (Invitrogen). Five different fields of view per substrate were counted under a Zeiss Axiovert 200M fluorescence microscope.

In addition, cell viability on the substrates of interest to the present study was also determined using a Live/Dead Viability/Cytotoxicity Kit for mammalian cells (Molecular Probes, Carlsbad, CA). The adherent cells on each substrate were stained with a mixture of calcein AM and ethidium homodimer-1 (EthD-1) according to manufacturer's instructions. Briefly, a solution of 2 μM calcein AM and 4 μM EthD-1 was prepared (the optimal dye concentrations for current cells according to the product protocol suggested). Then, the above dye solution was added into each substrate seeded with cells as described and was incubated at 37 ℃ for 30 min before visualization under a Zeiss Axiovert 200M fluorescence microscope. The dead and live cells were counted at approximate 490 nm/530 nm wavelengths (excitation/emission) for calcein AM and 560 nm/640 nm wavelengths (excitation/emission) for EthD-1, respectively.

2.3.3.3 Osteoblast Proliferation

For osteoblast proliferation studies, similar to the above procedures, osteoblasts were seeded on substrates (0.01 mg/mL RNT-K embedded in hydrogels and controls) at 2500 cells/cm^2 and were cultured for 1 and 3 days. After the prescribed time periods, adherent cells were fixed, stained with DAPI and counted under the fluorescence microscope as described above. All cellular experiments were run in triplicate and repeated at least three times for each substrate.

2.3.4 Mechanisms of Osteoblast Adhesion on RNT Hydrogels

2.3.4.1 Contact Angle and Surface Energy Measurements

The hydrophilicity of the various RNT hydrogels was measured by an EasyDrop contact angle measuring system (DSA1, Krüss, Germany). Before measurements, a 0.5 mm thick layer of hydrogels was first cast on glass in order to obtain a relatively flat hydrogel surface. 0.01 and 0.001 mg/mL of RNT-K as well as 1%, 5% and 10% RNT-RGD-K were coated on hydrogels for 45 min at room temperature. Static contact angles were measured 10 s after placing 3 μL of dH_2O on the sample surfaces. Surface energy ($E_{surface}$) was calculated using the equation $E_{surface}=E_{lv}\times\cos\theta$, where $E_{lv}=72.8$ mJ/m^2 at 20 ℃ for pure water and θ is the measured contact angle [26]. All experiments were conducted in ambient conditions and were performed at least 6 times per sample.

2.3.4.2 Fibronectin Adsorption (ELISA)

A well established enzyme-linked immunosorbent assay (ELISA) [27,28] was used to determine the amounts of fibronectin that adsorbed on the various RNT hydrogels. 0.01 mg/mL of 1%, 5%, and 10% RNT-RGD-K as well as 0.01 mg/mL RNT-K coated hydrogels were exposed to 10 μL of fibronectin (F1141, Sigma-Aldrich, MO) in 0.5 mL of PBS and were incubated for 24 h at 37 ℃. The negative controls were prepared by only adding PBS (without fibronectin) into each well. After PBS rinsing, non-specific fibronectin adsorption on the substrates was blocked by soaking in 2% bovine serum albumin (BSA, Sigma-Aldrich, MO) for 1 h. Fibronectin was then bound to a primary rabbit anti-bovine fibronectin antibody (Chemicon, CA) for 1 h. The samples were further incubated with a secondary goat anti-rabbit antibody conjugated with horseradish peroxidase (Bio-Rad, MD) for 1 h. After washing with 0.05% Tween 20 (Sigma-Aldrich, MO), the amount of fibronectin absorption on RNT hydrogels was measured with an ABTS substrate kit (Vector Laboratories, CA). The secondary antibody binding was detected using a microplate spectrophotometer at an absorbance wavelength of 405 nm (SpectraMax 340PC, Molecular Devices, CA). The average absorbance was subtracted by the average absorbance obtained from negative controls and analyzed with SoftMax$^{@}$ Pro 5 software. Experiments were run in triplicate at three different times.

2.3.4.3 Cytocompatibilty Comparison of RNTs to Collagen and Poly L-Lysine

In order to understand the potential role of RNTs (specifically, their nanostructure and surface chemistry) in mediating osteoblast functions, type I collagen and lysine were separately coated on hydrogels and compared with the same concentration of RNTs coated on hydrogels as just described. Specifically, rat tail type I collagen (Sigma-Aldrich, C3867) was used and diluted into two concentrations (0.01 mg/mL and 0.001 mg/mL) for cell tests. In addition, a 0.1% poly L-Lysine solution (Poly-K, Sigma) was diluted in ddH_2O to obtain 0.01 mg/mL and 0.001 mg/mL lysine solutions. Although these concentrations are larger than the concentration of lysine in the same concentration of RNT-K, they were chosen in order to initiate the role of lysine plays in RNT-K mediating osteoblast adhesion. Hydrogels were coated with these solutions and respective RNTs at room temperature for 45 min. Osteoblasts were then seeded for 4 h, fixed, stained, and counted as described above.

2.3.5 Statistics

Experiments were run in triplicate and repeated at least three times for each substrate. Numerical data were analyzed with a student's t-test to make pair-wise comparisons. Statistical significance was considered at $p<0.1$.

2.4 Results

2.4.1 Synthesis and Characterization of RNTs and RNT Hydrogels

The G^C-RGDSK was characterized with ^{1}H-NMR, ^{13}C-NMR spectra, high resolution ESI-MS and elemental analysis (Figure 2.4). From ^{1}H-NMR (Figure 2.4(1)), all expected ^{1}H resonances (labeled as A-Z, AA and BB in Figure 2.4) on the G^C-RGDSK were observed. Furthermore, ^{13}C-NMR data (Figure 2.4(2)) showed that the C's in the RGDSK peptide (i.e., the aliphatic CH, CH_2, CH_3, arginine's guanidinium group, four CONH groups and two COOH groups) were present on the newly functionalized G∧C motif. Finally, according to the elemental analysis shown in Figure 2.4(4), C, H and N in the new compound were measured at 32.82%, 4.03% and 13.58%, which was comparable to the theoretical values of C (32.88), H (4.01) and N (13.70) in the G^C-RGDSK. These data verified that the RGDSK peptide was successfully attached to the G^C motif to form G^C-RGDSK. Similarly, G^C-K was also verified the purity and structure as shown in [5].

The structure of the RNT-K embedded hydrogel scaffolds and hydrogel controls were studied by TEM. The procedure followed resulted in minimal disturbance of the nanostructures formed in the hydrogels and, thus, had the ability for the most direct visual inspection of the morphology of RNT-K in the hydrogels. Figures 2.5A and 2.5B show that very large hydrogel fibers (100-300 nm in diameter), which originated from phase

separation during the polymerization, were formed in the hydrogel controls. In contrast, TEM images revealed that the RNT-K formed a dense network of long nanotubes several nm in diameter extending up to 3 μm in length (Figures 2.5C and 2.5D). These nanotubes oriented in the hydrogels and were linked by a number of junctions that contributed to the formation of a highly interconnected network structure. It should be pointed out that the RNT-K embedded in hydrogels were removed for TEM analysis when the polymerization proceeded nearly to half of the time. Obviously, tubular structures of RNT-K were preserved during the polymerization process and the density and length of RNT-K dramatically increased based on the slight heating as well as due to interconnecting with the natural hydrogel fibers. Figures 2.5E and 2.5F revealed 0.01 mg/mL of RNT-K self-assembling in serum free medium and in water. The bundles of nanotubes were visible under the TEM.

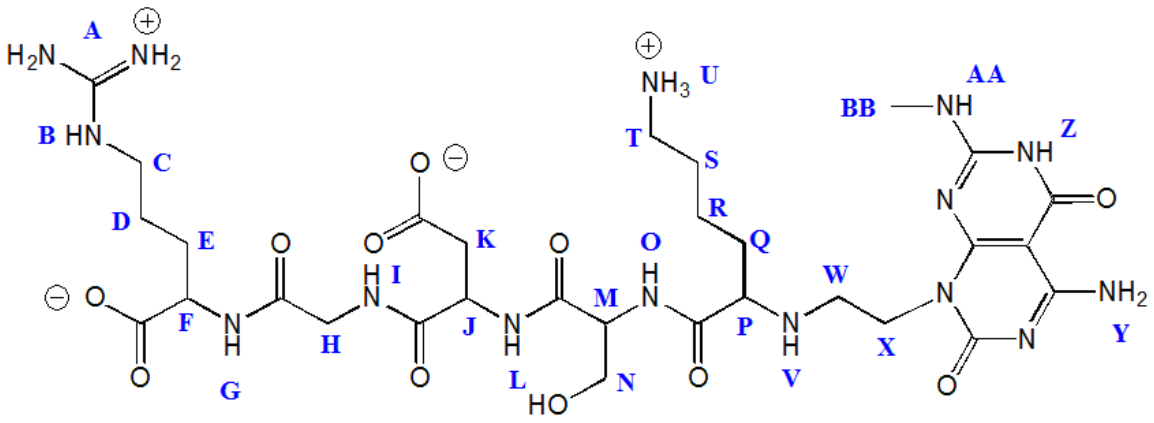

(1) ^{1}H-NMR (500 MHz, in 90% H_2O/D_2O)**:** 9.25 (br, 2H, Y), 8.99 (m, 2H, L and O), 8.68 (m, 1H, V), 8.43 (m, 1H, Z), 8.32 (m, 1H, I), 8.08 (m, G), 7.65 (m, 1H, AA), 7.48 (br, 2H, U), 7.13 (br, 1H, B), 6.59 (br, 4H, A), 4.80 (m, 2H, X), 4.59 (m, 2H, J and M), 4.36-4.40 (m, 1H, F), 4.07 (m, 1H, P), 3.94 (s, 2H, H), 3.86 (d, 2H, K), 3.44 (m, 2H, N), 3.19 (t, 2H, C), 3.02 (s, 3, BB), 2.98 (m, 2H, T), 2.91 (m, 2H, W), 1.92 (m, 2H, S), 1.77 (m, 2H, D), 1.68 (m, 2H, Q), 1.61 (m, 2H, E), 1.45 (m, 2H, R).

(2) ^{13}C-NMR (600 MHz, D_2O)**:** 175.7, 174.3 (COOH groups), 172.8, 171.2, 171.1, 168.6 (CONH groups on peptide), 163.5 (COOH of TFA), 162.7, 160.4, 156.9, 156.0, 150.0, 83.0 (C's on G∧C base), 155.7 (CN_3H_3 group of R), 116.8 (quartet, CF_3 on TFA), 61.1, 60.5, 55.6, 52.7, 50.3, 44.4, 42.6, 40.6, 39.1, 38.9, 35.6, 29.4, 28.0, 27.9, 26.5, 24.5, 21.2 (aliphatic CH's, CH_2's and CH_3).

(3) High resolution electrospray ionization mass spectrometry (ESI-MS): Calculated mass for $C_{30}H_{51}N_{15}O_{11}$ $(M+H^+)/z$ 797.38815; observed 398.69341 $(M+2H^+)/z$.

(4) Elemental analysis: Calculated for $C_{30}H_{51}N_{15}O_{11}$ (G^C-RGDSK) + 6 CF_3CO_2H + $3H_2O$ = C (32.88), H (4.01), N (13.70). Observed C (32.82), H (4.03), N (13.58).

Figure 2.4 ^{1}H–NMR, ^{13}C–NMR, high resolution ESI–MS and elemental analysis data of G^C–RGDSK building blocks. The data were analyzed by Felaniaina Rakotondradany in Prof. Fenniri's lab at University of Alberta, Canada.

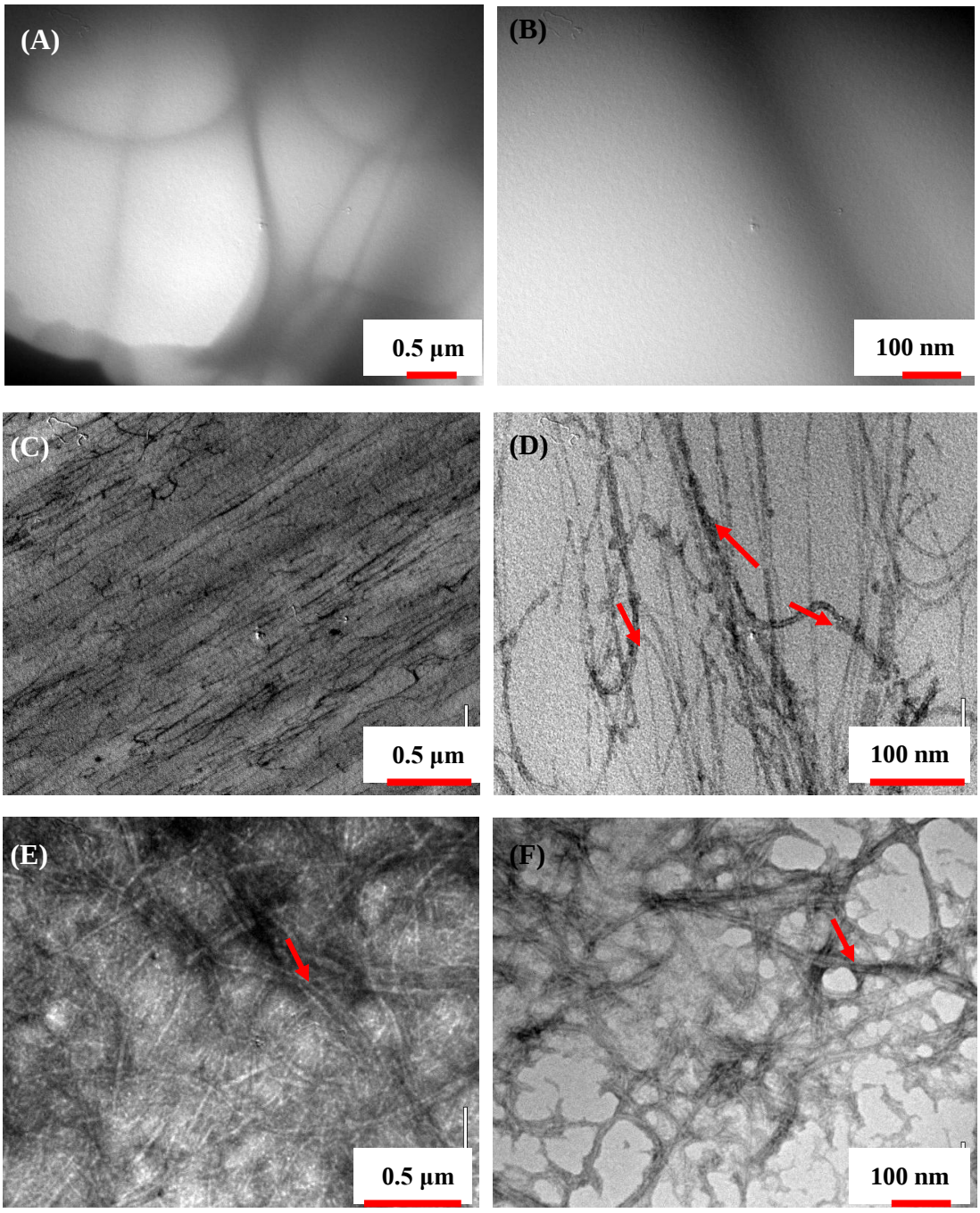

Figure 2.5 Negatively stained TEM images of the self-assembled RNT-K embedded in hydrogels, in water, in serum free medium and hydrogel controls at different magnifications. (A) Fibrillar hydrogel controls at low magnification; (B) Hydrogel controls at high magnification; (C) Oriented and long RNTs at 3.3 mg/mL concentrations embedded in hydrogels at low magnification; (D) Highly interconnected and densely packed RNTs at 3.3 mg/mL concentrations embedded in hydrogels; (E) 0.01 mg/mL RNT-K in serum free medium and (F) in water. The arrows point to individual nanotubes with 3~4 nm outer diameters.

Since the hydrogel scaffolds have very hydrophilic surfaces, they could not be cut by an ultramicrotome without any treatment that would disturb the RNTs. Thus, the scaffolds were embedded into Spurr's resin and TEM images were taken (Figures 2.6A and 2.6B) to provide information about the nanostructure of the low concentration of RNT-K embedded hydrogel scaffolds. Figure 2.6A shows there are numerous black dots in the hydrogels which have a similar size to the RNT cross sections. In contrast, no small dots appeared in hydrogel controls (Figure 2.6B). Therefore, it can be confirmed that the nanostructured and self-assembled properties of RNT-K were maintained in the hydrogel scaffolds in this study. Note also that Figures 2.5 and 2.6 confirmed that when increasing RNT-K concentration, more RNTs were observed in pHEMA (Figure 2.5 utilized 3.3 mg/mL RNT-K in pHEMA while Figure 2.6 utilized only 0.01 mg/mL RNT-K in pHEMA).

Furthermore, the synthesized G^C-RGDSK further assembled with G^C-K into RNT-RGD-K and were characterized with TEM. Figures 2.7A-2.7B, 2.7D-2.7E, and 2.7G-2.7H revealed that 1%, 5% and 10% molar ratios of the G^C-RGDSK and the G^C-K building blocks assembled into RNT-RGD-K nanotubes in water. Furthermore, the 1%, 5% and 10% RNT-RGD-K retained their nanotubular morphologies after embedding them into the hydrogels (Figures 2.7C, 2.7F and 2.7I), which was also observed in the unmodified RNT-K hydrogels (Figure 2.5). For the 1% RNT-RGD-K embedded in hydrogels (Figure 2.7C), very long nanotubes (nearly 10 μm) formed. Therefore, it was verified that the various RNTs preserved their nanotubular morphologies in the hydrogels even after being functionalized with RGDSK.

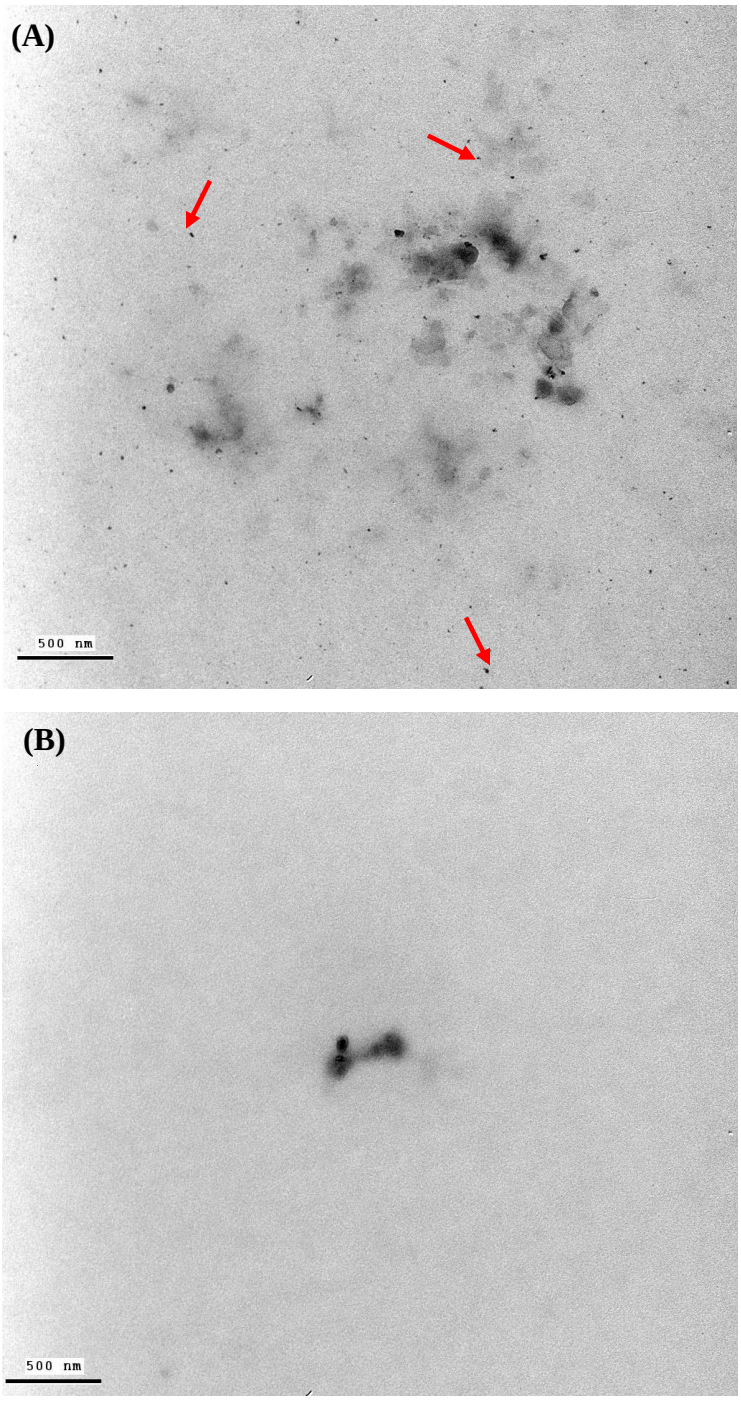

Figure 2.6 TEM images of thin sections of 0.01 mg/mL RNT-K embedded in hydrogels and hydrogel controls. (A) 0.01 mg/mL RNT-K embedded in hydrogels. (B) Hydrogel controls without RNTs. The arrows show the cross sections of RNTs. Scale bar is 500 nm.

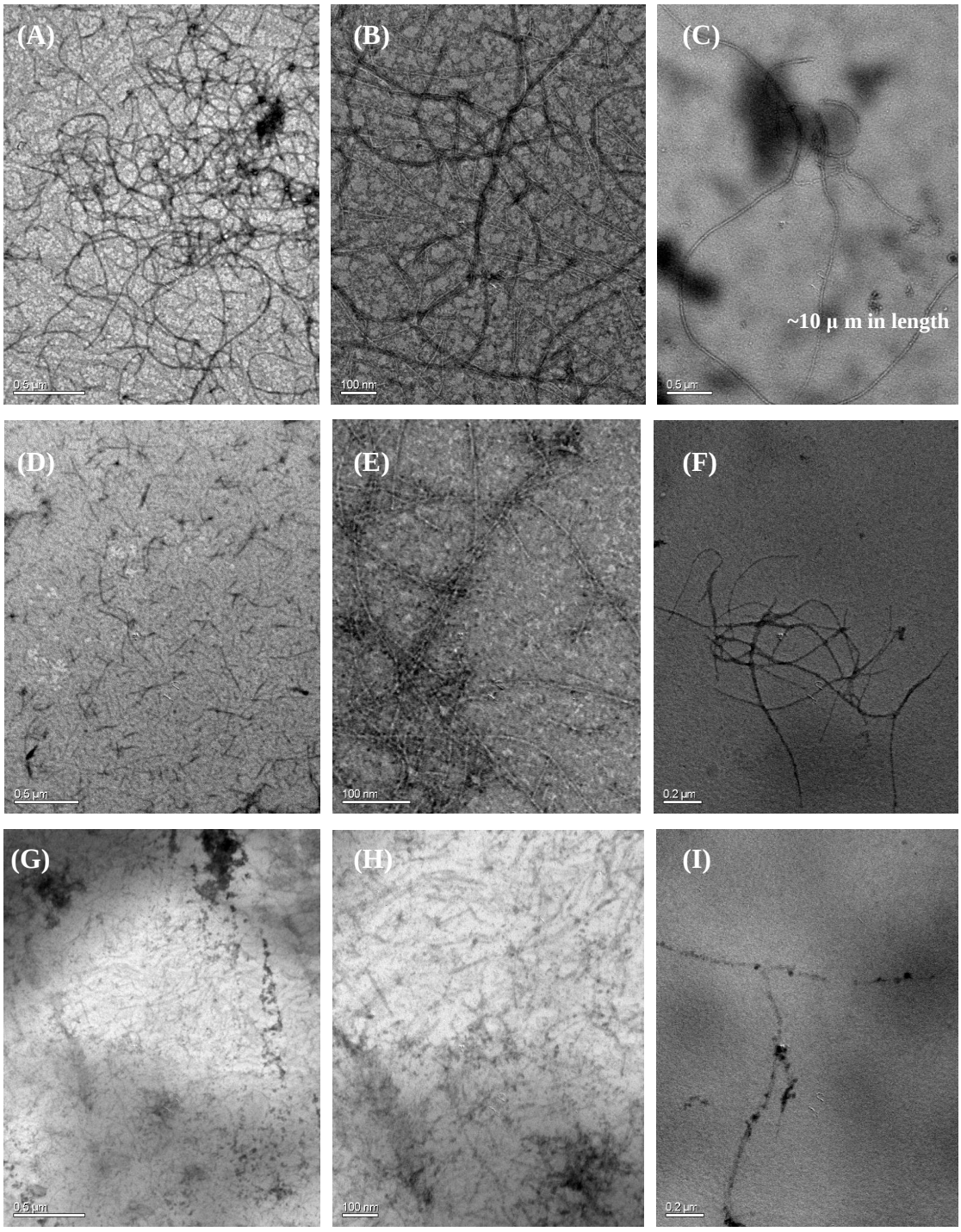

Figure 2.7 TEM images of 0.1 mg/mL of 1% 5% and 10% RNT-RGD-K in water and in hydrogels. (A), (B) and (C) are 1% RNT-RGD-K in water at low and high magnifications as well as in hydrogels, respectively. (D), (E) and (F) are 5% RNT-RGD-K in water at low and high magnifications as well as in hydrogels, respectively. (G), (H) and (I) are 10% RNT-RGD-K in water at low and high magnifications and in hydrogels, respectively.

Moreover, scanning electron micrographs showed that the various RNT-treated hydrogels and control samples had very rough, granular surfaces with rich porous structures inside, which contributed to the retention of a large amount of water in the hydrogels (Figures 2.8A-2.8F).

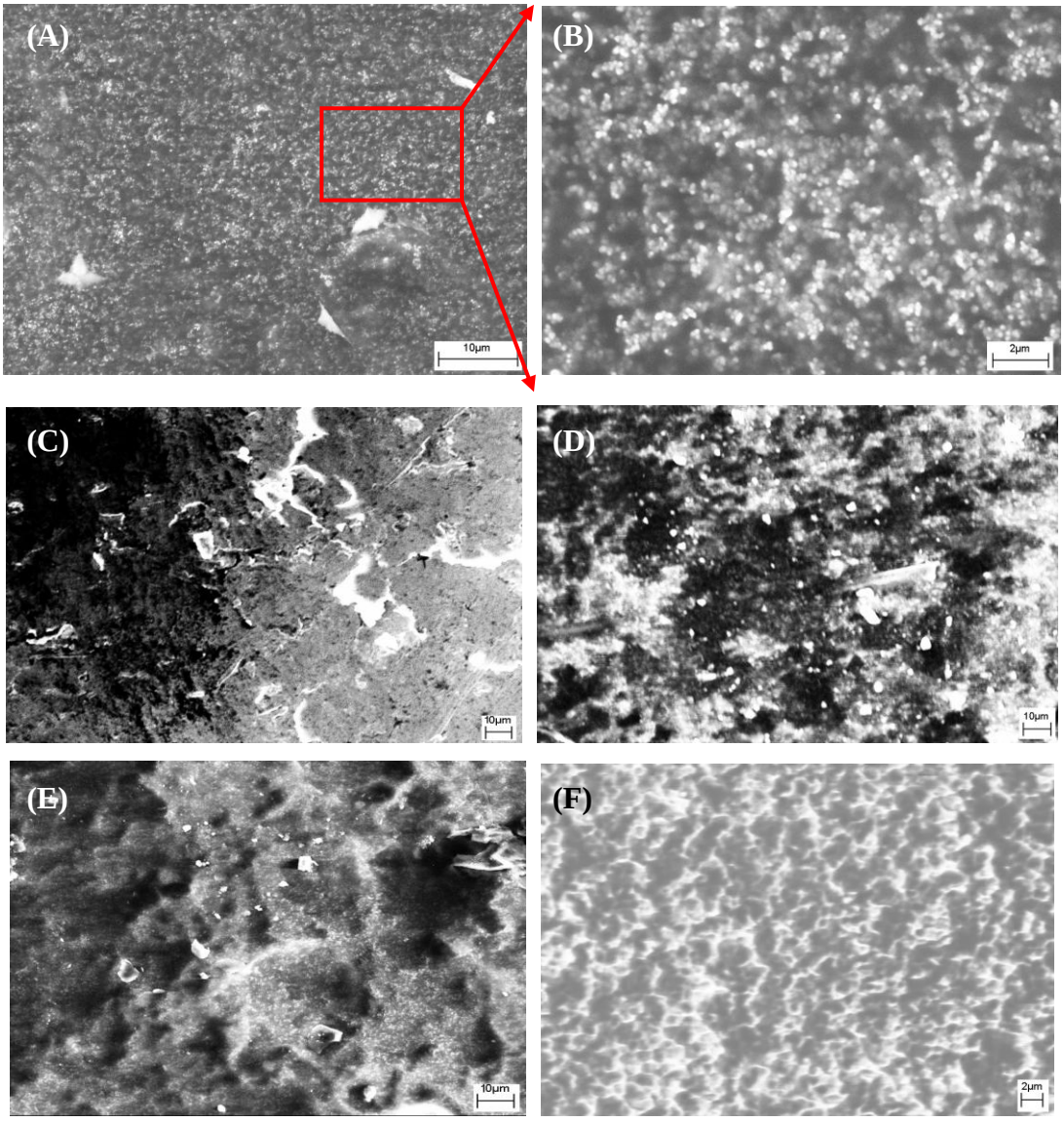

Figure 2.8 Surface morphology of 0.01 mg/mL RNT hydrogels and controls (SEM). (A) 10% RNT-RGD-K embedded in hydrogels; (B) Higher magnification of 10% RNT-RGD-K embedded in hydrogels; (C) 1% RNT-RGD-K embedded in hydrogels; (D) RNT-K embedded in hydrogels; (E) Hydrogel controls and (F) cross section of hydrogels which shows a macroporous network inside the hydrogel. Scale bars are 10 μm and 2 μm.

Previous AFM images of RNT-K adsorption on titanium or highly ordered pyrolytic graphite have clearly shown that RNT-K can be easily coated substrates to form a nanostructured RNT network [3,4,29]. The present AFM image of RNT adsorption on hydrogels is shown in Figure 2.9A. A sectional analysis of the data (Figures 2.9B and 2.9C) indicates a height of ~3.5-4.0 nm, which corroborates the calculated diameter of RNT-K from the aforementioned TEM results.

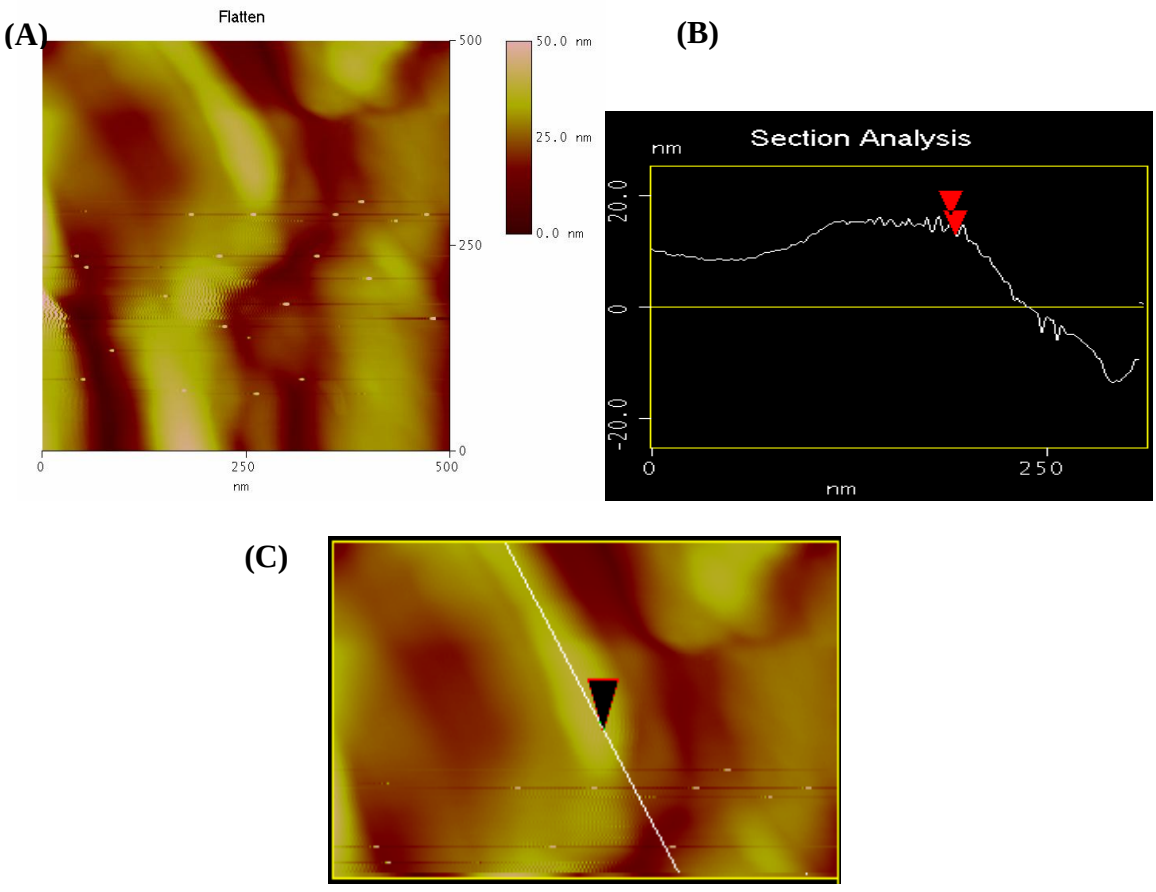

Figure 2.9 Tapping mode AFM images of RNT-K coated on hydrogels. (A) AFM images of 1.3 mg/mL RNTs coated on hydrogels and (B) and (C) section analysis of image A: Arrow heads display one nanotube. The section analysis indicates a height of ~3.9 nm, which is in agreement with the calculated diameter of a single RNT. Images obtained at 1 Hz, scan size is 500 nm.

According to the gelling condition studies (Figure 2.10), RNT-K embedded in hydrogels need significantly less polymerization time than hydrogel controls, especially at low temperatures (37-45°C). That is, by incorporating RNT-K with hydrogels, results of this study showed that bone regenerative constructs can be made through their solidification into viscous materials in less than 130 min at 40 °C (220 min for hydrogel controls without RNTs at 40 °C); at 37 °C, viscous constructs were made in 150 min for RNT-K with hydrogels while hydrogel controls took over 290 min.

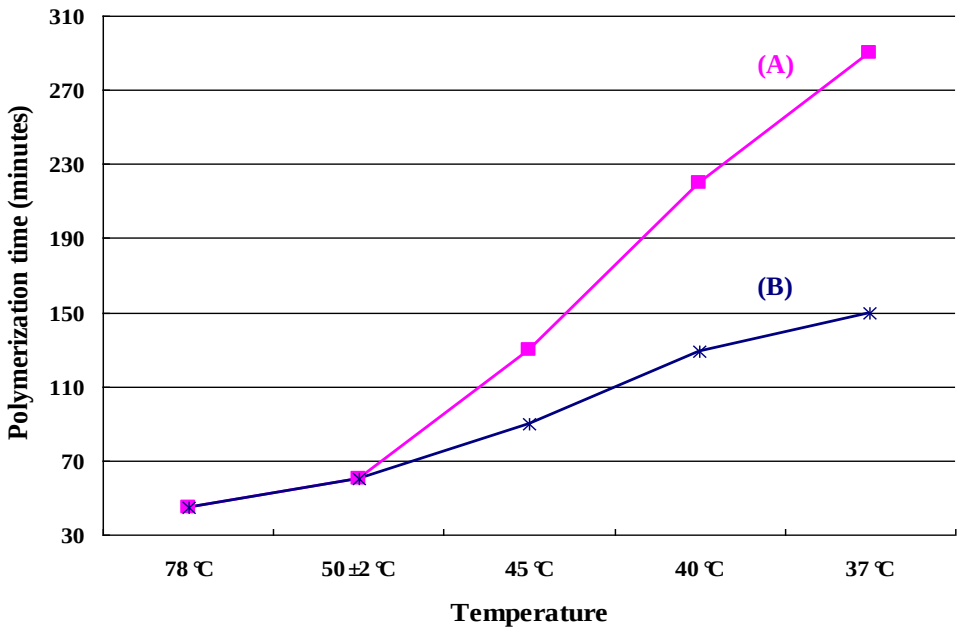

Figure 2.10 Temperature and RNT-K effect on hydrogel polymerization time. (A) Hydrogel control polymerization time at different temperatures and (B) 0.01 mg/mL RNT-K embedded in hydrogel polymerization time at different temperatures.

Moreover, the change of water content during polymerization was recorded at 1 h and 2 h for different concentrations of RNT-K embedded in hydrogels (0.01 mg/mL and 0.001 mg/mL) and hydrogel controls (Figure 2.11). It was found that 0.01 mg/mL and 0.001

mg/mL RNT-K embedded in hydrogels lost water significantly faster than hydrogel controls. The water content changed slightly after 2 h at a 45 ℃ reaction temperature for 0.01 mg/mL and 0.001 mg/mL RNT-K embedded in hydrogels. Visually, RNT-K embedded in hydrogels were completely polymerized while hydrogel controls just partly solidified after 2 h at a 45 ℃ heating. This also confirmed the above results of a quicker gelling time of RNT hydrogel scaffolds than hydrogel controls without RNTs at lower temperatures. In addition, Figure 2.11 revealed that the equilibrium water content for the above three types of hydrogel scaffolds were similar after 11 days: 66.74% for 0.01 mg/mL RNT-K embedded in hydrogels; 66.51% for 0.001 mg/mL RNT-K embedded in hydrogels and 66.19% for hydrogel controls.

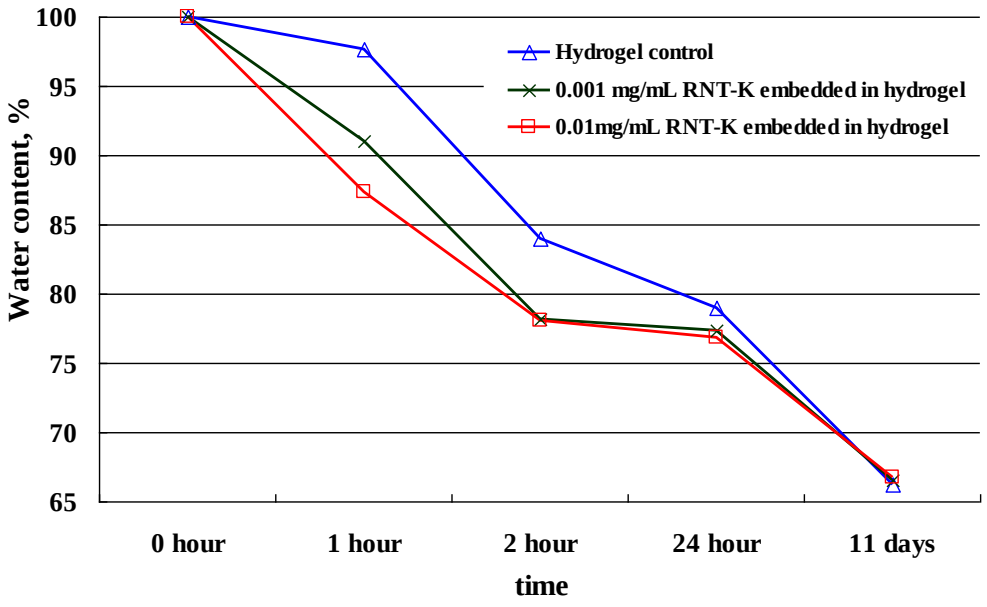

Figure 2.11 Water content of soaking scaffolds in water for 24 h and 11 days as well as changes of water content during polymerization (1 h, 2 h) for three types of hydrogel scaffolds: 0.01 mg/mL RNT-K embedded in hydrogels, 0.001 mg/mL RNT-K embedded in hydrogels, and hydrogel controls.

Furthermore, Figure 2.12 showed the swelling behavior of different types of RNTs at the same concentration in hydrogels for a period up to 18 days compared to controls (without RNTs, red line). The water content of the hydrogel controls greatly fluctuated compared to relatively small fluctuations of the RNT hydrogels. For instance, the water content of hydrogel controls decreased 13.9% while those for the RNT hydrogels changed less than 5% on the 6th day. After 18 days, controls decreased their water content 10% compared to 1.1%, 5.4%, ~0% and 2.7% for 0.01 mg/mL of 1%, 5%, 10% RNT-RGD-K and RNT-K hydrogels, respectively. The equilibrium water content of hydrogels did not show a large difference among the various RNT hydrogels and controls. In summary, the result suggested that incorporating various RNTs into hydrogels not only speeded up the polymerization time, but also diminished water content fluctuations of the hydrogels.

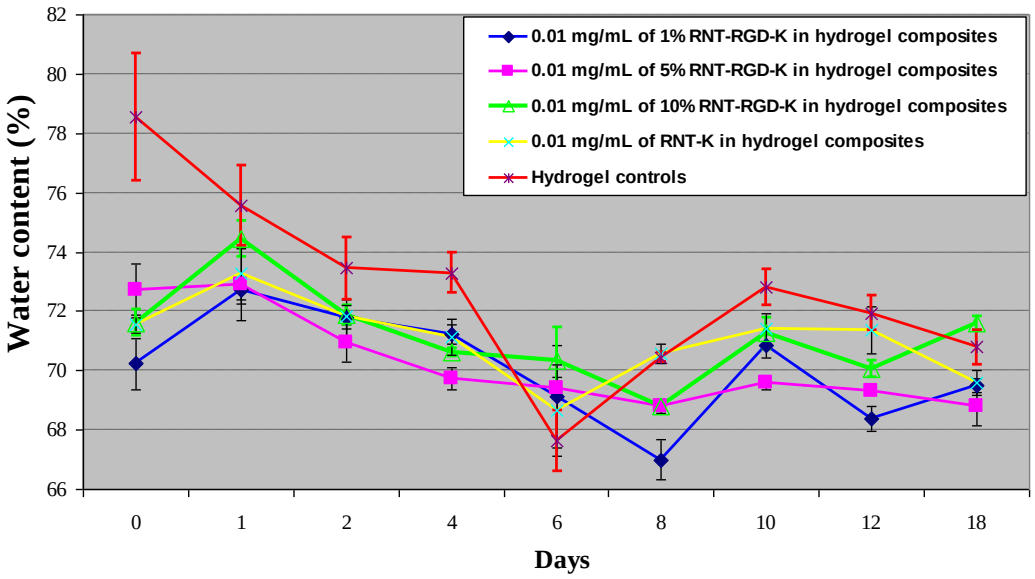

Figure 2.12 Water content changes and EWC of different RNT hydrogel composites. Relatively small water content changes occurred for RNTs in hydrogels. Error bars are mean ± SEM with n=3.

2.4.2 Favorable Osteoblast Responses on Nanostructured RNT Hydrogels

Figure 2.13 shows the results of osteoblast adhesion on the different concentrations of RNT-K coated on and embedded in hydrogels. Osteoblasts adhered more on RNT-K coated on and embedded in hydrogel scaffolds than to uncoated hydrogels. In the case of 0.01 mg/mL RNT-K coated on hydrogels, the results ($p<0.001$) were significantly greater than that of uncoated hydrogels. With increasing RNT-K concentrations, cell density also increased. The difference in osteoblast adhesion between 0.01 mg/mL RNT-K embedded in and coated on hydrogels was not statistically significant. Also, there was no statistical difference between osteoblast adhesion on 0.001 mg/mL RNT-K embedded in and coated on hydrogels. Lastly, there were no significant differences found in the number of dead cells on the substrates of interest to the present study (Figure 2.13). However, since there were more cells on the RNT-K embedded in and coated on hydrogels, a larger percentage of live cells (and a smaller percentage of dead cells) was observed on those composites compared to pure hydrogels. Fluorescently stained cell nuclei on the various substrates are shown in Figure 2.14.

Furthermore, the osteoblast proliferation results also provided the first evidence that the 0.01 mg/mL RNT-K embedded in hydrogels enhanced osteoblast growth more than hydrogel controls after 1 and 3 days of cultures (Figure 2.15). The osteoblast density on RNT-K hydrogels was 115.4% more than that on hydrogel controls after 3 days. Moreover, although osteoblasts on each of the substrates proliferated from 1 to 3 days, embedding RNT-K into hydrogels improved cell growth by 160.5% compared to an

83.3% improvement in control experiments.

Most importantly, after modifying RNTs with RGD side chains, more favorable osteoblast adhesion on 1%, 5% and 10% RNT-RGD-K hydrogels was observed in this study (Figure 2.16). Specifically, results of the present study provided the first evidence that RNT-RGD-K hydrogels contributed to more than a 136% increase in osteoblast density than controls after 4 h. In particular, 10% RNT-RGD-K coated on or embedded in hydrogels enhanced osteoblast attachment by 209% and 197%, respectively, when compared to controls.

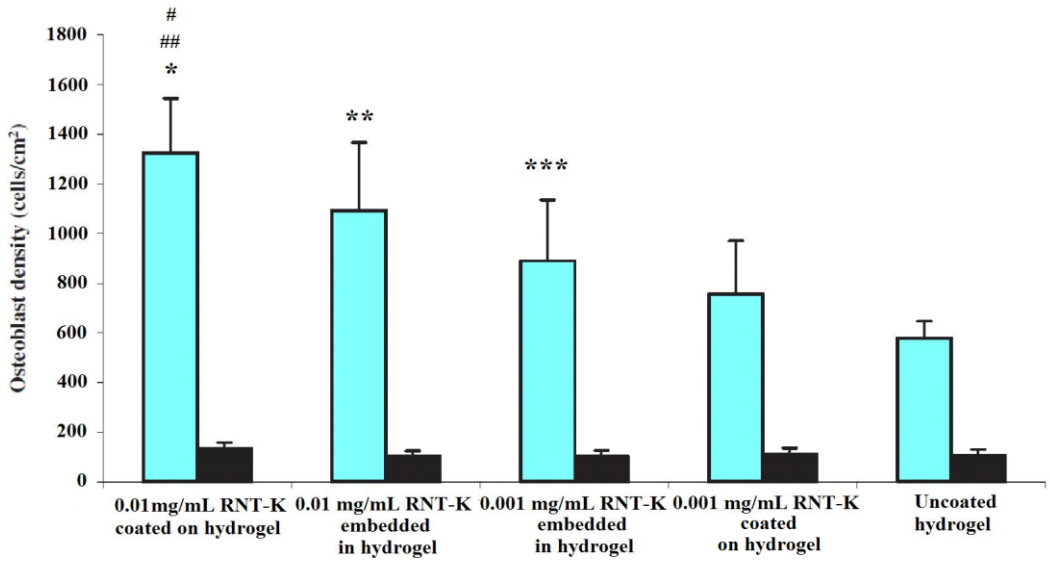

Figure 2.13 Enhanced osteoblast adhesion on 0.01 mg/mL RNT-K coated and embedded hydrogels. Data are mean ±SEM; N=3. *p<0.001, **p<0.01, and ***p<0.05 when compared to uncoated hydrogels; $^{\#}$p<0.005 when compared to 0.001 mg/mL RNT-K coated on hydrogels. $^{\#\#}$p<0.05 when compared to 0.001 mg/mL RNT-K embedded in hydrogels. Light blue bars are total cells; black bars are dead cells.

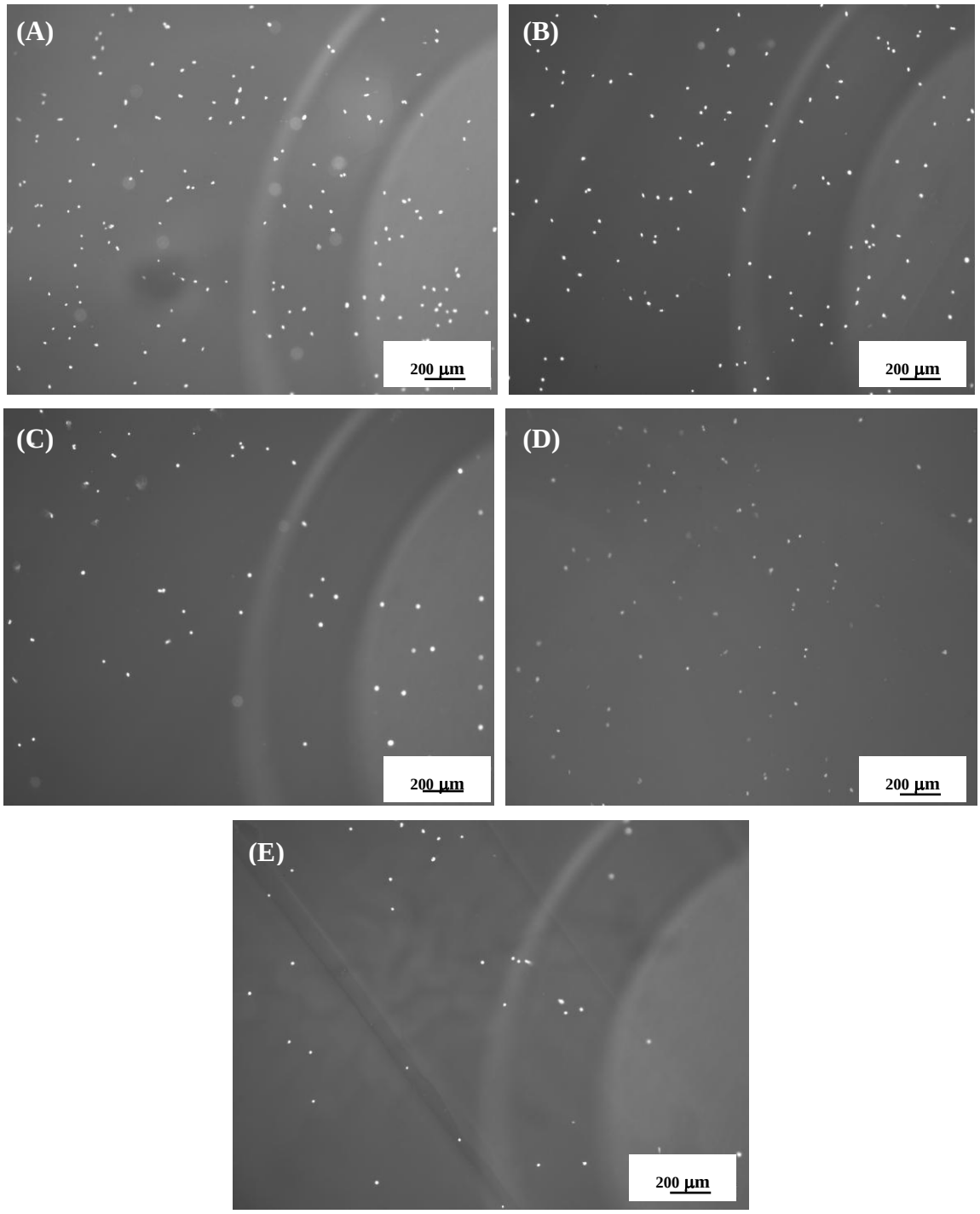

Figure 2.14 Increasing number of fluorescently stained osteoblasts on RNT-K coated or RNT-K embedded hydrogels compared to plain hydrogel controls. (A) 0.01 mg/mL RNT-K coated on hydrogels; (B) 0.01 mg/mL RNT-K embedded in hydrogels; (C) 0.001 mg/mL RNT-K embedded in hydrogels; (D) 0.001 mg/mL RNT-K coated on hydrogels; and (E) hydrogel controls without RNTs. Scale bars are 200 µm.

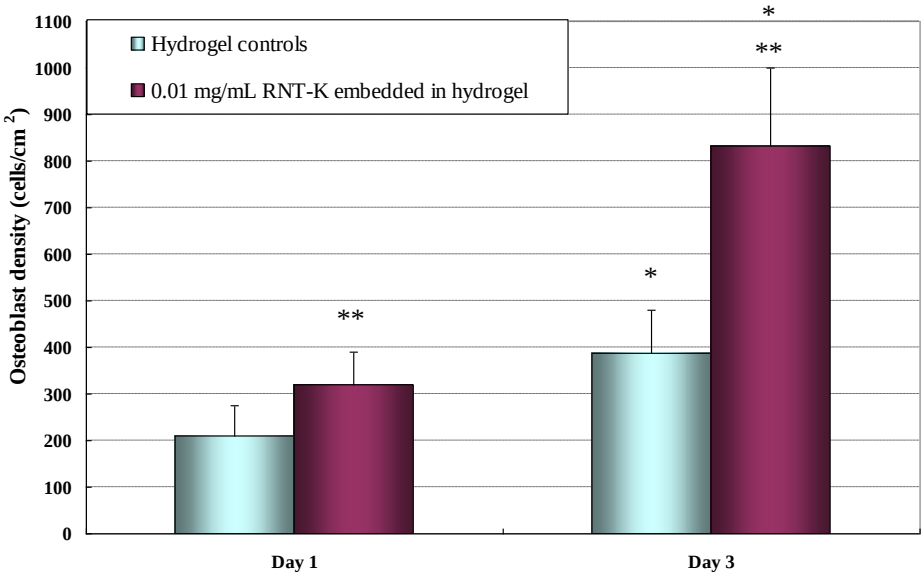

Figure 2.15 One and three day osteoblast densities on RNT hydrogels. Data are mean values ±SEM; N=3, *p<0.05 compared to respective hydrogels after 1 day cell culture and **p<0.05 compared to hydrogel controls at respective days.

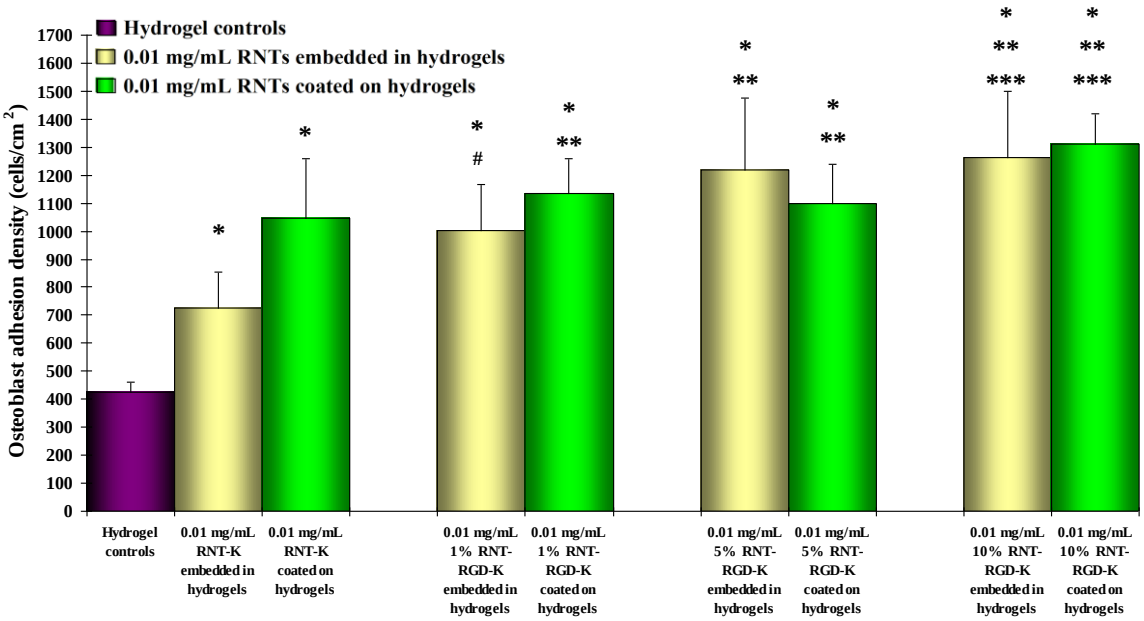

Figure 2.16 Improved osteoblast adhesion on 0.01 mg/mL RNT-RGD-K hydrogels after 4 h. Data are mean values ±SEM; N=3. *p<0.05 compared to uncoated hydrogels, **p<0.05 and #p<0.1 compared to 0.01 mg/mL RNT–K embedded in hydrogels, and ***p<0.1 compared to respective 0.01 mg/mL 1% RNT–RGD–K coated on and embedded in hydrogels.

Furthermore, an increasing trend of osteoblast adhesion with increasing RGD molar ratios on RNTs was observed. That is, a statistically significant difference in osteoblast adhesion on 1%, 5% and 10% RNT-RGD-K hydrogels relative to the same concentration of RNT-K embedded in hydrogels was observed. Specifically, 10% RNT-RGD-K coated on or embedded in hydrogels improved osteoblast adhesion by 80.9% and 74.1%, respectively, compared to unmodified RNT-K embedded in hydrogels. Thus, the modified RNT-RGD-K hydrogels were more effective at increasing osteoblast adhesion on hydrogels, which provided evidence of the excellent cytocompatibility properties of the RNTs as bone tissue engineering materials.

2.4.3 The Potential Reasons for RNTs Improving Osteoblast Density

Since the surface wettability, surface energy, surface chemistry and surface roughness of biomaterials are believed to be closely related to mediating cell adhesion, proliferation and differentiation on surfaces [27,30], the results of following sections will give some insights into the role of surface features of the RNTs towards enhancing osteoblast density. First, pHEMA hydrogels did not vary significantly in their contact angle measurements as the hydrophilicity only decreased slightly after the incorporation of RNT-K (Figure 2.17A). Interestingly, the hydrophilicity of the modified RNT-RGD-K hydrogels also decreased (for example, the contact angle of 5% was 63.9 º and 10% was 60.6 º) compared to uncoated hydrogels (46.6 º) (Figure 2.17B).

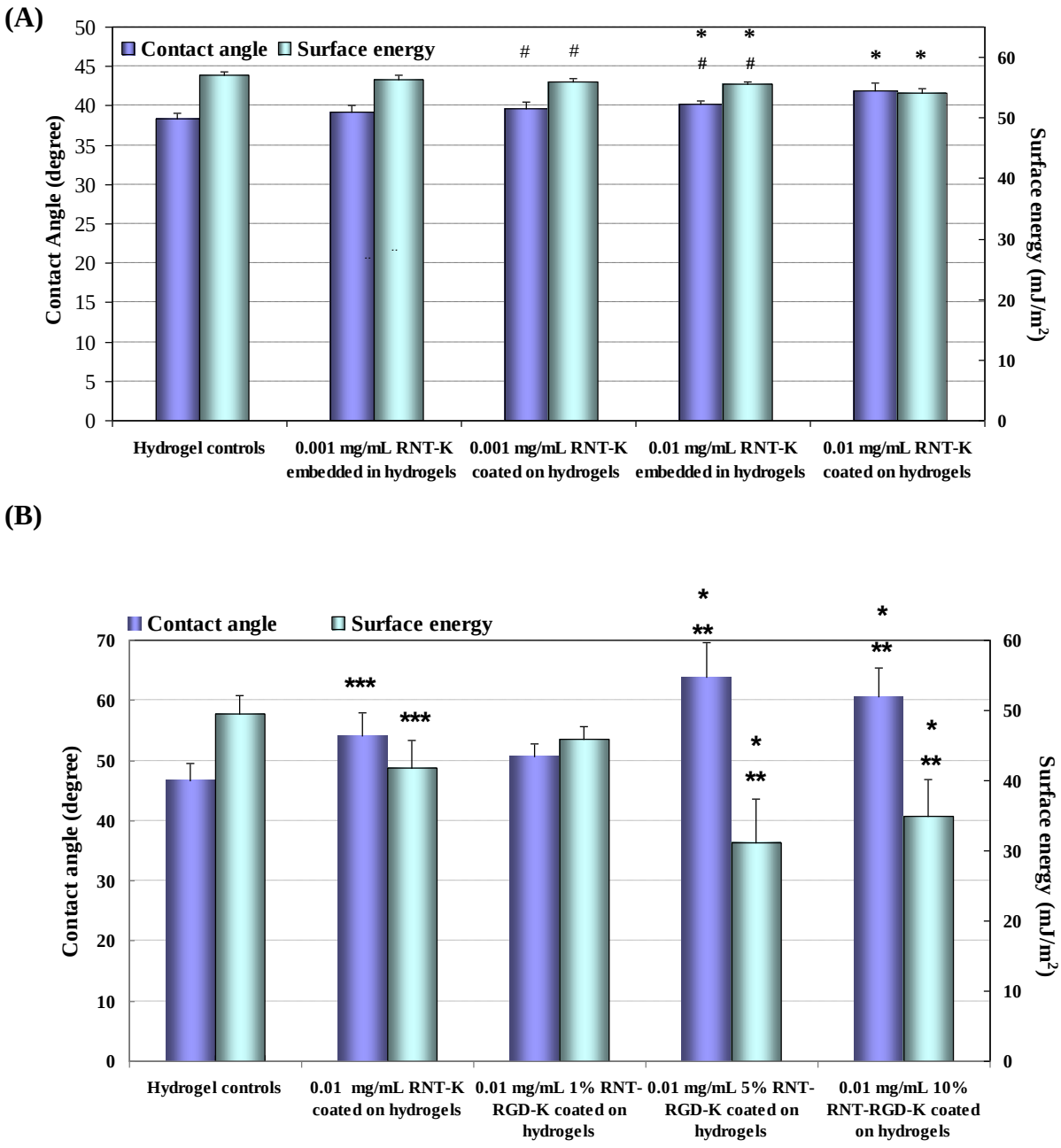

Figure 2.17 Changes in surface wettability and surface energy after coating either RNT-RGD-K or RNT-K on hydrogels. (A) The slightly increased hydrophobicity and decreased surface energy of RNT-K hydrogels and (B) the wettability and surface energy changes of RNT-RGD-K hydrogels compared with controls. Data are mean values ±SEM; n=6, *$p<0.05$ when compared to hydrogel controls, **$p<0.05$ when compared to 1% RNT-RGD-K coated on hydrogels, ***$p<0.1$ when compared to hydrogel controls, and $^{\#}p<0.05$ when compared to 0.01 mg/mL RNT-K coated on hydrogels.

More importantly, an increasing trend of fibronectin adsorption was observed on the 1%, 5% and 10% RNT-RGD-K and RNT-K coated hydrogels compared to uncoated hydrogels (Figure 2.18). Specifically, significantly greater amounts of fibronectin adsorbed onto the hydrogels coated with 0.01 mg/mL of 1% and 5% RNT-RGD-K as well as RNT-K relative to uncoated hydrogels. The greatest fibronectin adsorption occurred on the 1% RNT-RGD-K hydrogels. There was no statistical difference in protein adsorption between RNT-K, 5% and 10% RNT-RGD-K coated on hydrogels.

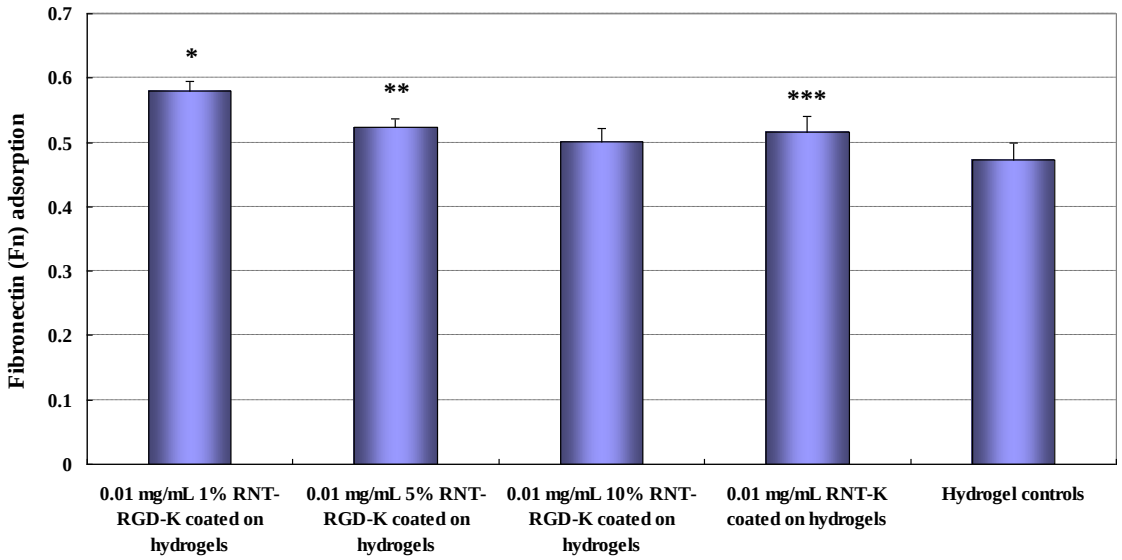

Figure 2.18 Increased fibronectin adsorption on RNT coated hydrogels. Data are mean values ±SEM; N=3, *$p<0.05$ when compared to all other scaffolds, **$p<0.05$ and ***$p<0.1$ when compared to hydrogel controls.

From the surface chemistry point of view, Figure 2.19 provides evidence that the amino acid side chains on RNTs were involved in increasing osteoblast attachment in this study. For example, osteoblast adhesion on poly L-Lysine coated hydrogels significantly increased with increasing lysine concentrations from 0.001 to 0.01 mg/mL, which was

also better than uncoated hydrogels (Figure 2.19). Similarly, the 0.01mg/mL RNT-K and RNT-RGD-K coated hydrogels increased osteoblast adhesion more than 0.001 mg/mL RNT-K coated hydrogels. In addition, results revealed that 0.01mg/mL RNT-K and RNT-RGD-K coated hydrogels increased osteoblast adhesion by 72% compared to the same concentration of poly L-Lysine coated hydrogels. Lastly, osteoblasts were more spread on RNT-K and RNT-RGD-K coated hydrogels than on uncoated hydrogels or poly L-Lysine coated hydrogels at respective concentrations (Figures 2.20A-2.20F).

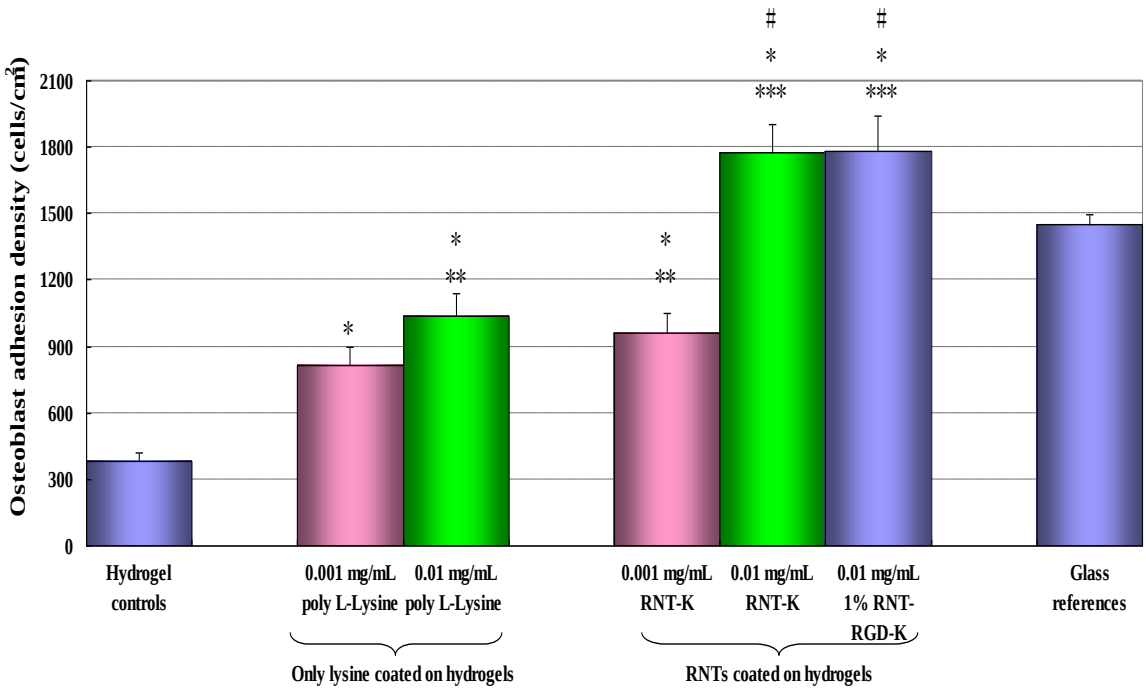

Figure 2.19 Quantitative results of enhanced osteoblast adhesion on RNT-K and RNT-RGD-K coated hydrogels compared to poly L-Lysine coated hydrogels. Data are mean values ±SEM; N=3. *$p<0.001$ when compared to uncoated hydrogels; **$p<0.05$ when compared to 0.001 mg/mL poly L-Lysine coated hydrogels; ***$p<0.01$ when compared to 0.01 mg/mL poly L-Lysine coated hydrogels; and #$p<0.001$ when compared to 0.001 mg/mL RNT-K coated hydrogels.

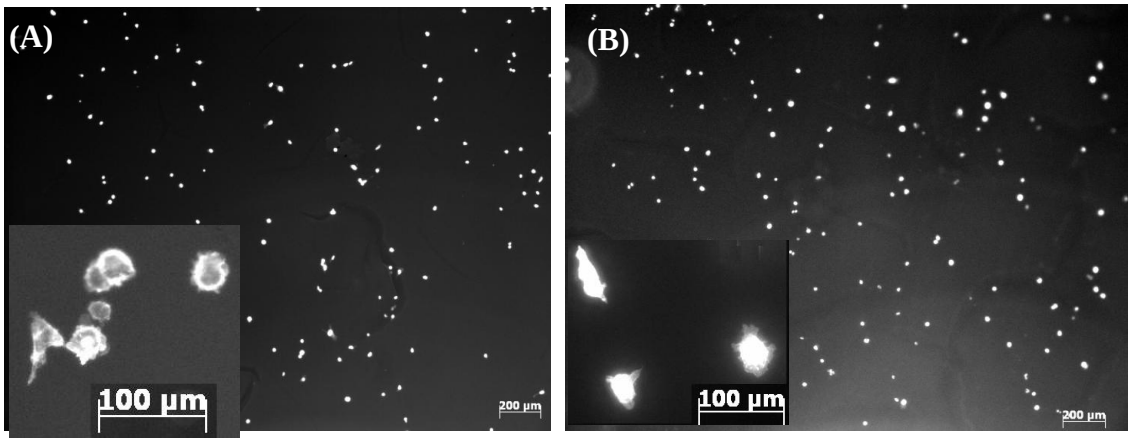

0.01 mg/mL of 1% RNT-RGD-K coated on hydrogels **0.01mg/mL of RNT-K coated on hydrogels**

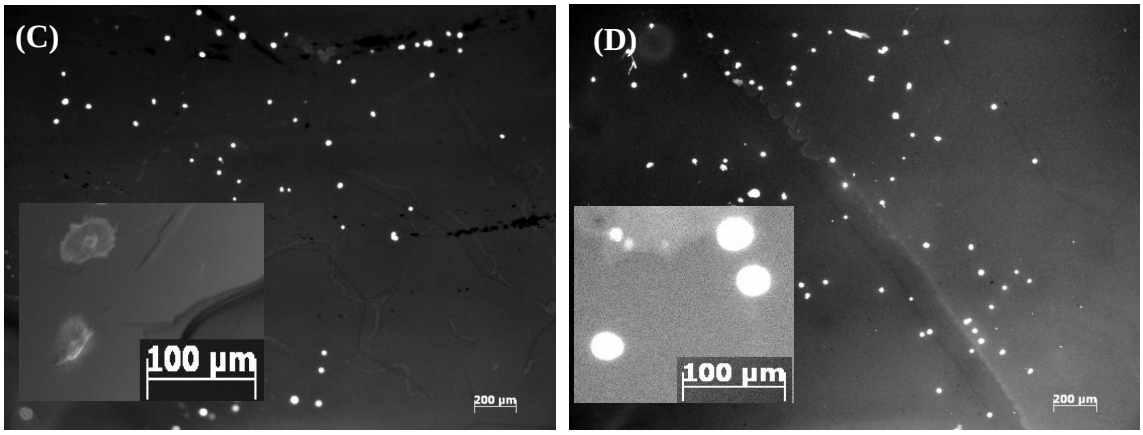

0.001mg/mL of RNT-K coated on hydrogels **0.01 mg/mL of poly L-Lysine coated on hydrogels**

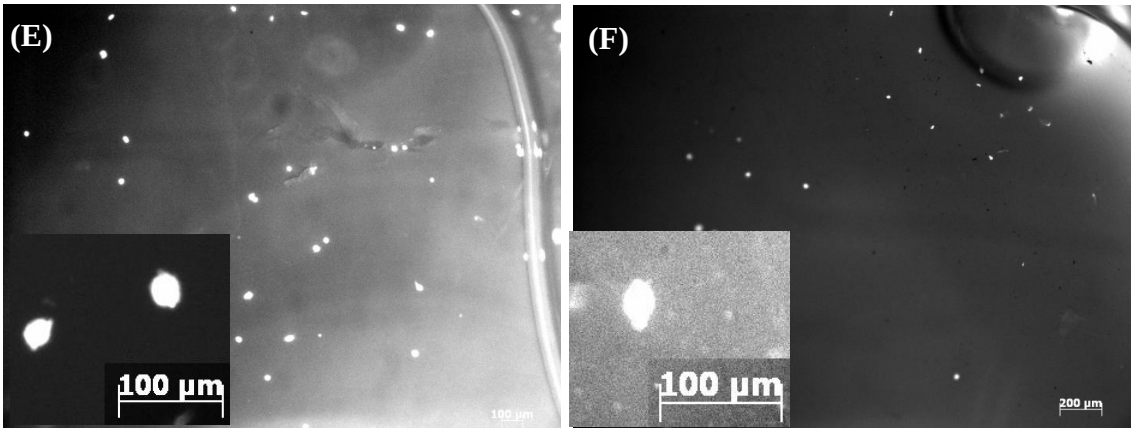

0.001 mg/mL of poly L-Lysine coated on hydrogels **Uncoated hydrogels**

Figure 2.20 Increasing fluorescently stained osteoblasts and extended cell spreading (inset images, stained F-actin filaments) on RNT-K and RNT-RGD-K coated hydrogels compared to poly L-Lysine coated hydrogels at respective concentrations and hydrogel controls. Scale bars are 200 µm in the large images and 100 µm in the inset images.

This study established the synergistic role of not only adhesion peptides conjugated to the RNTs but also the nanoscale architecture in promoting osteoblast adhesion; in particular, the RNTs feature dimensions that are reminiscent of collagen in the extra-cellular matrix of bone. These studies have shown that 10% RNT-RGD-K coated hydrogels promoted a 73% increase in osteoblast adhesion compared to the same concentration of collagen coated hydrogels (Figure 2.21). Additionally, higher concentrations of collagen were more efficient at improving osteoblast adhesion than lower concentrations of collagen and poly L-Lysine. Fluorescently stained cell nuclei on the various substrates are shown in Figure 2.22.

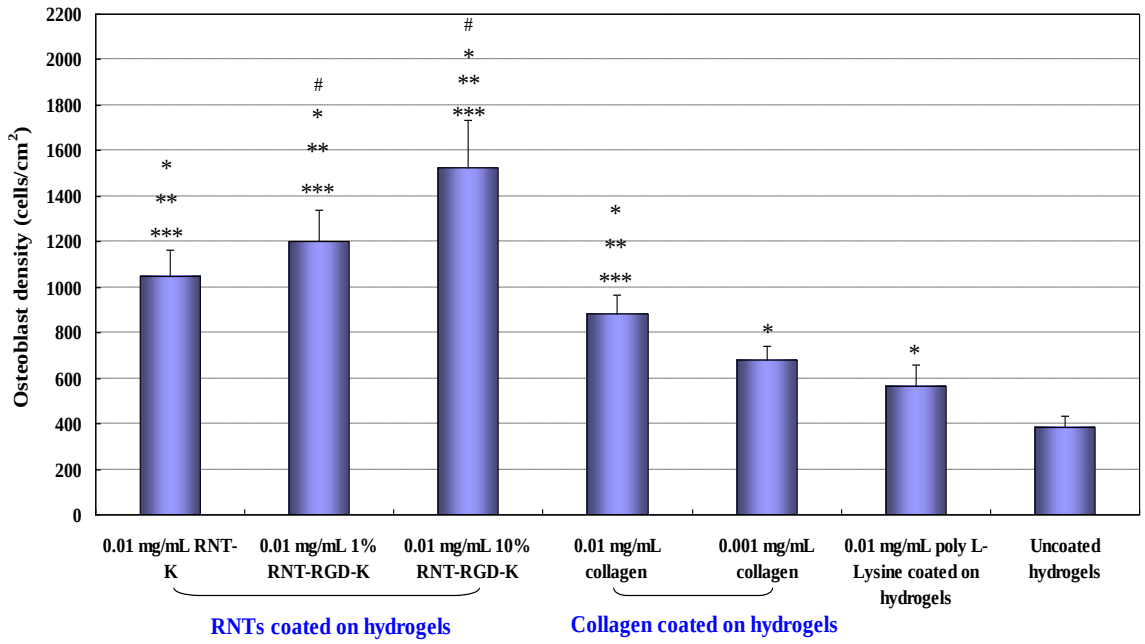

Figure 2.21 Enhanced osteoblast adhesion on RNT-RGD-K coated hydrogels compared to collagen coated hydrogels. Data are mean values ±SEM; N=3. *p<0.05 compared to uncoated hydrogels, **p<0.05 compared to 0.001 mg/mL collagen coated hydrogels, ***p<0.01 compared to 0.01 mg/mL poly L-Lysine coated hydrogels, and #p<0.05 compared to 0.01 mg/mL collagen coated hydrogels.

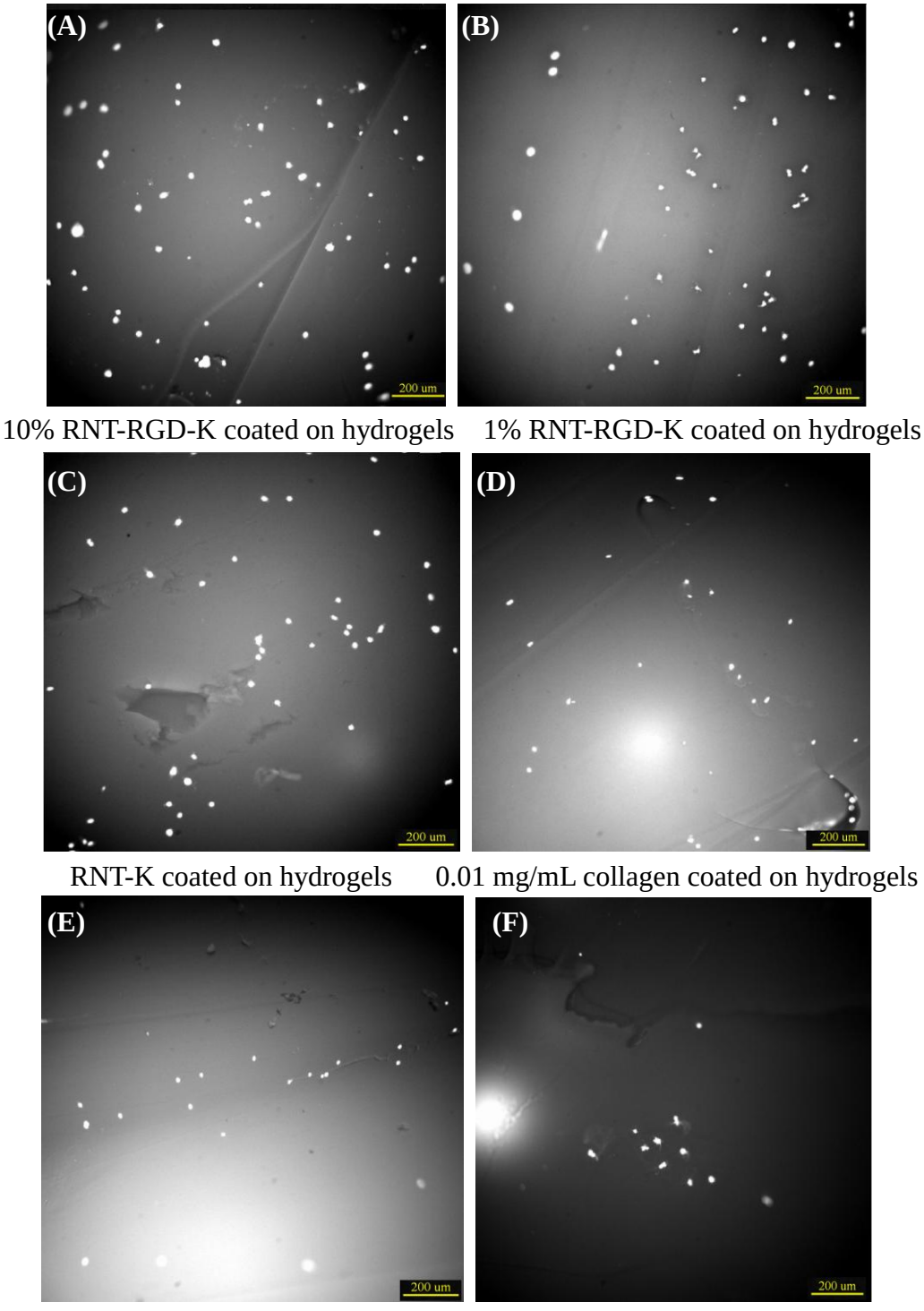

Figure 2.22 Fluorescence microscopy images of osteoblast stained nuclei on different substrates. Scale bar is 200 μm.

2.5 Discussion

2.5.1 The Morphologies and Properties of RNTs and Hydrogel with RNTs

It is widely known that components of the bone matrix (such as hydroxyapatite, collagen, laminin, fibronectin and vitronectin) are nanoscale in dimension as mentioned in section 1.3.1. Thus, current bone tissue engineering efforts are focused on the design of a matrix that mimics the nanoscale features of bone while providing a scaffold for tissue regeneration [31-33]. Previous research [34-38] has shown that various cell adhesion and proliferation can be greatly enhanced on materials including polymers, ceramics, metals and composites thereof with grain sizes (and consequent surface features) less than 100 nm. When RNTs were coated on implant surfaces, a nanometric network was formed that resembled the nanoscale constituents in bone (such as collagen) to increase bone cell functions. Previous studies have shown extensive networks and bundles of long RNT-K structures on titanium (Figure 2.23A) [4,29] and highly ordered pyrolytic graphite [3]. Since reproducing such dimensions on implant surfaces is critical in bridging synthetic materials with living systems (in order to achieve a stronger and more robust integration/bond between the implant and tissue), it was thus anticipated that RNTs would be better-suited for orthopedic applications compared to conventional implant materials (Figure 2.23B) which do not mimic the nanometric features of bone.

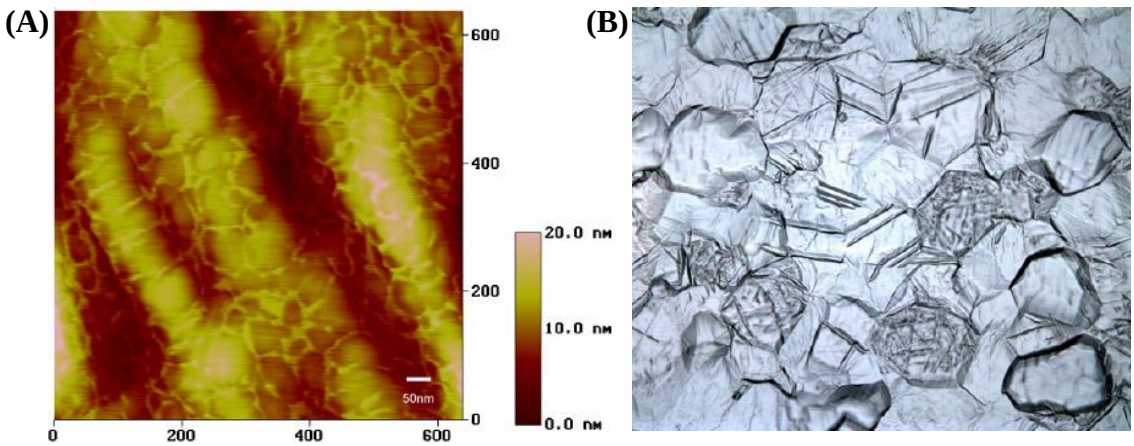

Figure 2.23 Surface roughness comparisons of RNTs and conventional titanium. (A) AFM images of RNTs with a 3.5 nm height roughness on titanium; (B) Optical micrographs of the micron titanium surface (400× magnification). The surface roughness of titanium is 1.5 ±0.5 μm. This figure is adapted from [29].

Furthermore, there is also much interest in the use of liquid injectable materials that can solidify into a scaffold once inserted in the human body. Injectable bone substitutes have the advantages of minimally invasive surgery and may alleviate many challenges associated with current surgical treatments [39,40]. Thus, the formation of injectable scaffolds onto which cells are able to develop new bone tissue at the site of fracture is a promising method to repair bone fractures and defects. Due to the fact that RNTs self-assembly is an entropically driven process in which temperature plays a crucial role, heating can result in longer and more aggregated nanotubes [3,4]. In this light, it has been found that when heating aqueous RNT-K to over 60 ℃, a phase transition from a liquid to a viscous gel is observed [3]. Furthermore, a more viscous gel-like RNT can be also obtained when added directly to serum-free media at body temperatures [3]. Because RNT can undergo the above phase transition from a liquid to a viscous gel when heated or when added directly to serum-free media, RNT may provide an exciting therapy to heal bone fractures and defects in situ as injectable bone filler materials. Figures 2.5C and

2.5D provided evidence that a dense, oriented and highly interconnected long nanotube network formed in the hydrogels when heating RNT-K in hydrogels to 40-50 ℃. Figure 2.7C, 2.7F and 2.7I revealed long nanotubes can form inside RGD modified RNT hydrogels as well. These studies also confirmed that the biologically-inspired nanostructure features of RNT-RGD-K occurred throughout the hydrogels and were not just limited to the surface.

In fact, the current study found that the polymerization of the novel nanostructured hydrogels occurred at a faster rate at 40-45 ℃ compared to hydrogel controls without RNTs. This ease of processability can be advantageous if used in vivo in injectable form and can, thus, be promising clinically since surgery time would be decreased. In addition, equilibrium water content and water content change are important parameters to evaluate the swelling behavior of hydrogels. Although RNTs embedded in hydrogels and controls have similar EWC, the swelling behavior of the RNT hydrogel composites created in this study revealed relatively small changes of water content compared with the hydrogels without RNTs. Since pHEMA has been investigated as an excellent drug delivery system, the slow change of water content may help control the release of growth factors (such as bone morphogenetic proteins) from macroporous hydrogels to bone fracture sites over an extended time period in order to accelerate the bone repair process.

Furthermore, because of the macroporous structure of the RNT hydrogels revealed by SEM, cellular infiltration into this scaffold is anticipated. These water-containing pores can easily allow water and other nutrients in while allowing waste removal from

embedded cells. In addition, the hydrogel pore size and morphology can be modified by controlling phase separation and gelation time, polymerization temperature and other factors [41].

2.5.2 The Excellent Cytocompatibility Properties of RNT Hydrogels

Because the adhesion of osteoblasts plays a critical role in subsequent bone tissue regeneration on implanted materials, the present cell adhesion experiments provided evidence of enhanced osteoblast adhesion on RNT-K hydrogel scaffolds even at RNT concentrations of 0.01 mg/mL. For example, hydrogel scaffolds coated with RNT-K at 0.01 mg/mL significantly increased osteoblast adhesion 75.1% and 129.5% compared to 0.001 mg/mL RNT-K coated and uncoated hydrogels, respectively. A similar tendency was also observed on 0.01 mg/mL RNT-K embedded hydrogels. Osteoblast adhesion on 0.001 mg/mL RNT-K coated and embedded hydrogels were statistically similar to uncoated hydrogels due to the relatively low concentration of RNT-K. These results are consistent with previous studies that focused on investigating RNT-K as a potential orthopedic Ti-coating material [3,4,29]. In addition, enhanced osteoblast proliferation on RNT-K embedded in hydrogels after 3 days revealed that RNTs further improved osteoblast functions much more than uncoated controls.

Importantly, a RGDSK peptide was successfully covalently linked onto the G^C base. The co-assembly of this conjugate with G^C–K at molar ratios of 1, 5, and 10% yielded nanotubular assemblies that were more efficient at promoting osteoblast adhesion. These

results are very encouraging because they not only indicate a new type of RNTs with desirable chemistry, but they also show the feasibility of diversifying the adhesive properties of RNTs to selectively recruit other cell types. For instance, conjugation of RNTs with KRSR (Lys-Arg-Ser-Arg) would selectively bind heparin sulfate proteoglycans in osteoblast cell membranes and promote osteoblast adhesion, but may inhibit fibroblast adhesion [42,43]. A 209% increase in osteoblast adhesion on RNT-RGD-K hydrogels as shown in this study (Figure 2.16) demonstrates the exceptional promise of these RNT-RGD-K hydrogels. This study also demonstrated that increasing the ratio of RGD to K on RNTs directly affected osteoblast density on these scaffolds. Consequently, this indicated that such RGD modified RNTs indeed contributed to a more cytocompatible bone healing material.

2.5.3 Mechanisms of Favorable Osteoblast Responses Towards RNTs

2.5.3.1 The Role of Protein Adsorption and Surface Wettability

A key objective of this study was to clarify possible reasons why nanostructured RNT hydrogels were more cytocompatible with osteoblasts than other substrates tested herein. As an attempt to understand osteoblast adhesion on these materials, fibronectin adsorption on RNT coated hydrogels compared to uncoated hydrogel controls was determined. Specific protein adsorption on implant surface is directly related to bone cell functions [44-46]. For instance, Webster et al. reported that increasing protein (including vitronectin and fibronectin) adsorption on nanophase materials [45,46] may be one of the

underlying mechanisms that improved osteoblast functions on such materials.

In the present work, greater fibronectin adsorption was observed on 0.01 mg/mL of 1% and 5% RNT-RGD-K as well as RNT-K hydrogels compared to uncoated hydrogels, lending insights into why osteoblast adhesion was enhanced on these scaffolds. Furthermore, although fibronectin adsorption on 10% RNT-RGD-K was statistically similar to uncoated hydrogels, the rich RGD side chains on its outer surface (ten and two times over RGD on 1% and 5% RNT-RGD-K) served some additional functions to directly improve osteoblast adhesion. In addition, it was also found that the unique surface chemistry of the RNTs played a key role in changing surface wettability and corresponding surface energy of these materials to influence protein adsorption. The pHEMA hydrogels increased hydrophobicity when coated with RNTs. The relatively long molecular chains shown in the G^C-RGDSK chemical structures increased surface hydrophobicity of the hydrogels. However, it should be pointed out that all RNT hydrogels exhibited modestly hydrophilic surfaces (contact angles roughly less than 60) which have been shown by others to be favorable for osteoblast attachment [26].

2.5.3.2 The Role of Surface Chemistry

Because RNTs have special surface chemistry originating from their rich peripheral amino acid and peptide distributions, these K or RGD side chains provided a favorable environment for improving cell adhesion. For example, Figure 2.16 provides evidence that higher molar ratios of RGD on RNTs (such as 10%) can induce more osteoblast

adhesion than RNT-K without RGD or 1% HRN-RGD-K. This indicated that the cell-adhesive RGD peptides on RNTs closely contributed to the favorable osteoblast responses on RNT-RGD-K hydrogels.

On the other hand, poly L-Lysine coated hydrogels were used to confirm that the amino acids (such as K) alone enhanced osteoblast adhesion. The structure and surface charge of poly L-Lysine (Figure 2.24) are similar to the lysine side chains on the outer surface of RNTs. Results indeed demonstrated that 0.01 mg/mL RNTs and poly L-Lysine with higher densities of lysine induced more osteoblast adhesion than 0.001 mg/mL RNTs and poly L-Lysine. This suggested that K side chains on RNTs provided a more favorable chemistry towards improving osteoblast adhesion on RNT coated hydrogels. According to the chemical structure of the various RNTs, numerous NH_2 (positively charged), COOH and OH groups on G^C-RGDSK or G^C-K building blocks have been reported to regulate focal adhesion, protein adsorption and osteoblast functions [47,48]. In addition, many other studies have supported the role that poly lysine plays in promoting cell adhesion [49-51]. For example, McKeehan and colleagues demonstrated that poly-lysine coated surfaces can cause human or chicken fibroblasts to adhere more strongly and fibroblasts were able to survive in lower concentrations of serum proteins in culture media when surfaces were coated with poly-lysine [49]. It was believed that the lysine moieties on RNTs had the potential for increasing osteoblast adhesion by possibly mimicking lysine-rich bovine bone proteins known to enhance osteoblast adhesion, proliferation and differentiation [4,52].

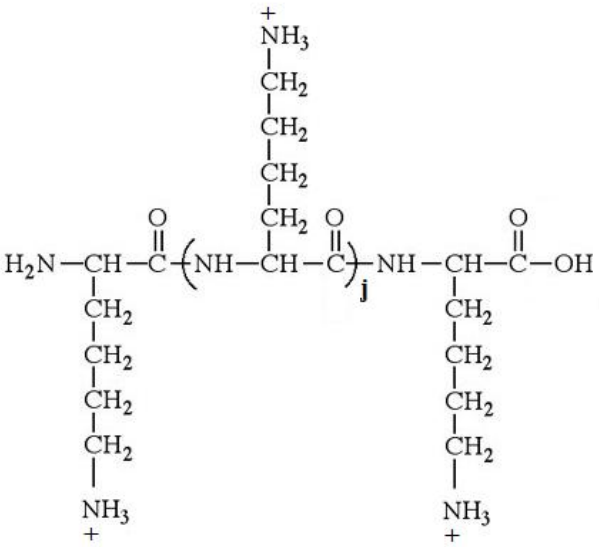

Figure 2.24 Poly L-Lysine structures. This figure is redrawn from [53].

Moreover, even though the molar amount of lysine on 0.01 mg/mL poly L-Lysine was more than that in 0.01 mg/mL RNT-K and RNT-RGD-K, osteoblasts attached more and were better spread on RNT coated hydrogels than poly L-Lysine coated hydrogels. Therefore, the lysine or RGD moieties may partly account for this favorable osteoblast adhesion on RNT coated and embedded hydrogels, but not for all of it. This may be explained by the unique nanotubular and biomimetic structures of RNTs in the next section.

2.5.3.3 The Role of Nanostructured Surface Topography

Actually, the nanoscale and tubular architecture that formed due to the presence of RNTs may have provided a nanoscale topography that improved protein adsorption in hydrogels by resembling properties (Specifically, chemistry, charges, and wettability) of an

extra-cellular matrix favorable to bone cells. For instance, higher concentrations of RNT-K hydrogels (such as 0.01 mg/mL RNT-K coated and embedded hydrogels) not only displayed more lysine side chains on the surfaces but also resembled a more dense nanometric network on hydrogels than 0.001 mg/mL RNT-K hydrogels, thus, inducing more osteoblast attachment. Since cell adhesion is a prerequisite for further differentiation, the present results show promise for RNT hydrogel scaffolds in orthopedic applications.

Furthermore, type I collagen is one of the main ECM components in bone, has nanometric and helical structures and contains cell-adhesive RGD peptides just like the RNT-RGD-K created in this study [30]. The RNT-RGD-K samples were further examined for their biomimetic properties by comparing osteoblast adhesion to collagen coated hydrogels. Results showed a collagen concentration-dependent osteoblast adhesion profile and that collagen promoted osteoblast adhesion more than poly L-Lysine. More importantly, RNT-RGD-K stimulated more osteoblast adhesion than type I collagen, which provided additional evidence of the promise of the biomimetic properties of RNTs for improving osteoblast adhesion.

2.6 Conclusions

In summary, the potential of nanostructured RNT hydrogels as novel tissue engineering scaffold materials for orthopedic applications was investigated here. A new family of RNTs functionalized with cell-adhesive RGD peptides were prepared and tested here for

the first time. This study demonstrated that these materials were attractive for promoting osteoblast adhesion due to their nanoscale dimensions and chemical composition. Easy and fast preparation of RNT coated and embedded hydrogels made them clinically promising materials for orthopedic applications.

Importantly, drastically increased osteoblast adhesion and proliferation were observed on these RNT hydrogels compared to hydrogel controls. Specifically, the 0.01 mg/mL RNT-K coated and embedded hydrogels significantly improved osteoblast adhesion compared to the hydrogel controls and other lower concentrations of RNT-K hydrogels. Furthermore, 10% RNT-RGD-K significantly promoted over a two-fold increase in osteoblast adhesion compared to hydrogel controls without RNTs. Incorporating cell-adhesive RGD onto RNTs improved their cytocompatibility properties pertinent to orthopedic applications more than unmodified RNT-K hydrogels.

In addition, this study investigated the possible underlying mechanisms of why RNTs increased osteoblast functions. Results demonstrated that 1% and 5% RNT-RGD-K and RNT-K coated on hydrogels greatly enhanced fibronectin adsorption compared to uncoated controls, which might be partly responsible for the enhanced osteoblast densities observed on these scaffolds. This study also provided evidence that the controllable surface chemistry (such as the K and RGD) and nanoscale-biomimetic features of RNTs created a cell-favorable environment to improve osteoblast functions, thus, making them intriguing materials for further study in orthopedic applications.

2.7 References

[1] Gu′ehennec LL, Soueidan A, Layrolle P, Amouriq Y. Surface treatments of titanium dental implants for rapid osseointegration. Dental Materials 2007;23:844–854.

[2] Zhang L, Chen Y, Rodriguez J, Fenniri H, Webster TJ. Biomimetic helical rosette nanotubes and nanocrystalline hydroxyapatite coatings on titanium for improving orthopedic implants. Int J Nanomedicine 2008;3:323–333.

[3] Chun AL. Helical rosette nanotubes: an investigation towards its application in orthopedics, Ph.D. thesis, Weldon School of Biomedical Engineering, Purdue University, West Lafayette, IN, 2006.

[4] Chun AL, Moralez JG, Webster TJ, Fenniri H. Helical rosette nanotubes: a biomimetic coating for orthopedics. Biomaterials 2005;26:7304–7309.

[5] Fenniri H, Mathivanan P, Vidale KL, Sherman DM, Hallenga K, Wood KV, Stowell JG. Helical rosette nanotubes: design, self–assembly and characterization. J Am Chem Soc 2001;123:3854–3855.

[6] Kroese–Deutman HC, Van Den Dolder J, Spauwen PHM, Jansen JA. Influence of RGD–loaded titanium implants on bone formation in vivo. Tissue Eng 2005;11:1867–1875.

[7] Schliephake H, Scharnweber D, Dard M, Rossler S, Sewing A, Meyer J, et al. Effect of RGD peptide coating of titanium implants on periimplant bone formation in the alveolar crest. An experimental pilot study in dogs. Clin Oral Implants Res 2002;13:312–319.

[8] Chua PH, Neoh KG, Kang ET, Wang W. Surface functionalization of titanium with hyaluronic acid/chitosan polyelectrolyte multilayers and RGD for promoting osteoblast functions and inhibiting bacterial adhesion. Biomaterials 2008;29:1412–1421.

[9] Picart C, Elkaim R, Richert L, Audoin T, Arntz Y, Cardoso MD, et al. Primary cell adhesion on RGD–functionalized and covalently crosslinked thin polyelectrolyte multilayer films. Adv Funct Mater 2005;15:83–94.

[10] Ho MH, Wang DM, Hsieh HJ, Liu HC, Hsien TY, et al. Preparation and

characterization of RGD–immobilized chitosan scaffolds. Biomaterials 2005;26:3197–3206.

[11] Schuler M, Owen GR, Hamilton DW, De Wilde M, Textor M, Brunette DM, et al. Biomimetic modification of titanium dental implant model surfaces using the RGDSP–peptide sequence: a cell morphology study. Biomaterials 2006;27:4003–4015.

[12] Lutolf MP, Weber FE, Schmoekel HG Schense JC, Kohler T, Muller R, Hubbell JA. Repair of bone defects using synthetic mimetics of collagenous extracellular matrices. Nat Biotechnol 2003;21:513–518.

[13] Elmengaard B, Bechtold JE, Soballe K. In vivo study of the effect of RGD treatment on bone ongrowth on press–fit titanium alloy implants. Biomaterials 2005;26:3521–3526.

[14] Masuko T, Iwasaki N, Yamane S, Funakoshi T, Majima T, et al. Chitosan–RGDSGGC conjugate as a scaffold material for musculoskeletal tissue engineering. Biomaterials 2005;26;5339–5347.

[15] Shin H, Jo S, Mikos AG. Modulation of marrow stromal osteoblast adhesion on biomimetic oligo[poly(ethylene glycol) fumarate] hydrogels modified with Arg–Gly–Asp peptides and a poly(ethylene glycol) spacer. J Biomed Mater Res 2002;61:169–179.

[16] Rammelt S, Illert T, Bierbaum S, Scharnweber D, Zwipp H, Schneiders W. Coating of titanium implants with collagen, RGD peptide and chondroitin sulfate. Biomaterials 2006;27:5561–5571.

[17] Bagno A, Piovan A, Dettin M, Chiarion A, Brun P, Gambaretto R, et al. Human osteoblast–like cell adhesion on titanium substrates covalently functionalized with synthetic peptides. Bone 2007;40:693–699.

[18] Zreiqat H, Akin FA, Howlett CR, Markovic B, Haynes D, Lateef S, et al. Differentiation of human bone–derived cells grown on GRGDSP–peptide bound titanium surfaces. J Biomed Mater Res A 2003;64:105–113.

[19] Giglio ED, Sabbatini L, Colucci S, Zambonin G. Synthesis, analytical characterization, and osteoblast adhesion properties on RGD–grafted polypyrrole coatings on titanium substrates. J Biomater Sci Polymer Edn 2000;11:1073–1083.

[20] Harris LG, Tosatti S, Wieland M, Textor M, Richards RG. Staphylococcus aureus adhesion to titanium oxide surfaces coated with non–functionalized and peptide–functionalized poly(L–lysine)–grafted–poly(ethylene glycol) copolymers. Biomaterials 2004;25:4135–4148.

[21] Zhang L, Rakotondradany F, Myles AJ, Fenniri H, Webster TJ. Arginine-Glycine-Aspartic Acid Modified Rosette Nanotube-Hydrogel Composites for Bone Tissue Engineering. Biomaterials, in press (2009).

[22] Cadotte AJ, DeMarse TB. Poly–HEMA as a drug delivery device for in vitro neural networks on micro–electrode arrays. J Neural Eng 2005;2:114–122.

[23] Refojo MF, Yasuda H. Hydrogels from 2-hydroxyethyl methacrylate and propylene glycol monoacrylate. J Appl Polym Sci 1965;9:2425–2435.

[24] Wisniewski S, Kim SW. Permeation of water-soluble solutes through poly(2-hydroxyethylmethacrylate) and poly(2-hydroxyethylmethacrylate) crosslinked with ethylene glycol dimethacrylate. J Membr Sc 1980;6:309–318.

[25] Stile RA, Burghardt WR, Healy KE. Synthesis and characterization of injectable poly(N isopropylacrylamide)–based hydrogels that support tissue formation in vitro. Macromolecules 1999;32:7370–7379.

[26] Liu X, Lim JY, Donahue HJ, Dhurjati R, Mastro AM, Vogler EA. Influence of substratum surface chemistry/energy and topography on the human fetal osteoblastic cell line hFOB 1.19: Phenotypic and genotypic responses observed in vitro. Biomaterials 2007;28:4535–4550.

[27] Khang D, Kim SY, Liu–Snyder P, Palmore GTR, Durbin SM, Webster TJ. Enhanced fibronectin adsorption on carbon nanotube/poly(carbonate) urethane: Independent role of surface nano–roughness and associated surface energy. Biomaterials 2007;28:4756–4768.

[28] Sato M. Nanophase hydroxyapatite coatings for dental and orthopedic applications, Ph.D. thesis, School of Materials Engineering, Purdue University, West Lafayette, IN, 2006.

[29] Chun AL, Moralez JG, Fenniri H, Webster TJ. Helical rosette nanotubes: a more effective orthopaedic implant material. Nanotechnology 2004;15:S234–S239.

[30] Webster TJ. Nanophase ceramics: the future orthopedic and dental implant

material. In: Ying JY, editor. Advances in chemical engineering. New York: Academic Press, 2001, p.125–166.

[31] Laurencin CT, Ambrosio AMA, Borden MD, Cooper JAJr. Tissue engineering: orthopedic applications. Annual Review of Biomedical Engineering 1999;1:19–46.

[32] Christenson EM, Anseth KS, Jeroen JJP, Beucken VD, et al. Nanobiomaterial applications in orthopedics. Journal of orthopedic research 2007;25:11–22.

[33] Ozbas B, Kretsinger J, Rajagopal K, Schneider JP, Pochan DJ. Salt-triggered peptide folding and consequent self-assembly into hydrogels with tunable modulus. Macromolecules 2004;37:7331–7337.

[34] Webster TJ, Siegel RW, Bizios R. Design and evaluation of nanophase alumina for orthopaedic/dental applications. Nanostructured Materials 1999;12:983–986.

[35] Webster TJ, Ejiofor JU. Increased osteoblast adhesion on nanophase metals: Ti, Ti6Al4V, and CoCrMo. Biomaterials 2004;25:4731–4739.

[36] Ejiofor J, Webster TJ. Biomedical implants from nanostructured materials. In: Schwarz JA, Contescu C, Putyera K, editors. Dekker Encyclopedia of Nanoscience and Nanotechnology. CRC Press: Taylor & Francis Group, LLC, 2004, p. 263–275.

[37] Thapa A, Miller DC, Webster TJ, Haberstroh KM. Nano-structured polymers enhance bladder smooth muscle cell function. Biomaterials 2003;24:2915–2926.

[38] Miller DC, Thapa A, Haberstroh KM, Webster TJ. Endothelial and vascular smooth muscle cell function on poly(lactic-co-glycolic acid) with nanostructured surface features. Biomaterials 2004;25:53–61.

[39] Stevens MM, George JH. Exploring and engineering the cell–surface interface. Science 2005;310:1135–1138.

[40] Bonzani IC, Adhikari R, Houshyar S, et al., Synthesis of two-component injectable polyurethanes for bone tissue engineering. Biomaterials 2007;28:423–433.

[41] Dalton PD, Flynn L, Shoichet MS. Manufacture of poly(2–hydroxyethyl methacrylate–co–methyl methacrylate) hydrogel tubes for use as nerve guidance channels. Biomaterials 2002;23:3843–3851.

[42] Balasundaram G, Webster TJ. Increased osteoblast adhesion on nanograined Ti modified with KRSR. J Biomed Mater Res 2007;80A:602–611.

[43] Dee KC, Andersen TT, Bizios R. Design and function of novel osteoblast adhesive peptides for chemical modifications of biomaterials. J Biomed Mater Res 1998;40:371–377.

[44] Tirrell M, Kokkoli E, Biesalski M. The role of surface science in bioengineered materials. Surf Sci 2002;500:61–83.

[45] Webster TJ, Ergun C, Doremus RH, Siegel RW, Bizios R. Specific proteins mediate enhanced osteoblast adhesion on nanophase ceramics. J Biomed Mater Res 2000; 51:475-483.

[46] Webster TJ, Schadler LS, Siegel RW, Bizios R. Mechanisms of enhanced osteoblast adhesion on nanophase alumina involve vitronectin. Tissue Eng 2001;7:291–301.

[47] Scotchford CA, Gilmore CP, Cooper E, Leggett GJ, Downes S. Protein adsorption and human osteoblast–like cell attachment and growth on alkylthiol on gold self–assembled monolayers. Inc J Biomed Mater Res 2002;59:84–99.

[48] Keselowsky BG, Collard DM, Garcia AJ. Integrin binding specificity regulates biomaterial surface chemistry effects on cell differentiation. PNAS 2005;102:5953–5957.

[49] McKeehan WL, Ham RG. Stimulation of clonal growth of normal fibroblasts with substrata coated with basic polymers. The Journal of Cell Biology 1976;71:727–734.

[50] Yavin, E., and Yavin, Z. Attachment and culture of dissociated cells from rat embryo cerebral hemispheres on polylysine-coated surface. The Journal of Cell Biology 1974;62:540–546.

[51] Watts KC, Husain OAN, Tucker JH, Stark M, Eason P, Shippey G, Rutovitz D, Frost GTB. The use of cationic polyelectrolytes in the preparation of cell monolayers for automated cell scanning and diagnostic cytopathology. Anal Quant Cytol 1984;6:272–278.

[52] Zhou HY, Ohnuma Y, Takita H, Fujisawa R, Mizuno M, Kuboki Y. Effects of a bone lysine-rich 18 kDa protein on osteoblast-like MC3T3-E1 cells. Biochem

Biophys Res Commun. 1992;186:1288–1293.

[53] Elbert DL, Hubbell JA. Self-assembly and steric stabilization at heterogeneous, biological surfaces using adsorbing block copolymers. Chemistry biology 1998;5:177–183.

CHAPTER 3

A BIOMIMETIC ROSETTE NANOTUBE NANOCRYSTALLINE HYDROXYAPATITE COMPOSITE FOR ORTHOPEDIC APPLICATIONS

A portion of this chapter has been published in:

1. **L. Zhang**, Y. Chen, J. Rodriguez, H. Fenniri and T.J. Webster. Biomimetic Helical Rosette Nanotubes and Nanocrystalline Hydroxyapatite Coatings on Titanium for Improving Orthopedic Implants. *Int. J. Nanomedicine*, 3(3): 323–333 (2008).
2. **L. Zhang**, J. Rodriguez, A.J. Myles, H. Fenniri and T.J. Webster. Biologically Inspired Rosette Nanotubes and Nanocrystalline Hydroxyapatite Hydrogel Nanocomposites as Improved Bone Substitutes. *Nanotechnology,* in press (2009).

3.1 Introduction

In the previous chapter, novel osteogenic rosette nanotube (RNT) hydrogels with favorable nanometric feature and cell-adhesive RGD or K side chains were created. It was demonstrated that RNT hydrogels significantly enhanced osteoblast adhesion and proliferation for bone tissue engineering applications. In this chapter, a biomimetic nanocomposite was designed to further improve the cytocompatibility and mechanical properties of RNTs for orthopedic applications.

As mentioned in chapter 1, inorganic nanocrystalline hydroxyapatite ($Ca_{10}(PO_4)_6(OH)_2$, HA) is the main component of the natural bone matrix. Specifically, HA has promising osteoconductive properties [1,2] and forms a tight bond with bone. High amounts of surface porosity, increased surface roughness and improved wettability of nanophase HA may have positive effects on the osseointegration of HA with juxtaposed bone by promoting various osteoblast functions (such as adhesion, proliferation and differentiation, etc.). As a result, HA has been one of the most popular bone graft substitutes, fillers and coating materials for orthopedic applications. Many researchers have reported even better cytocompatibility properties of nanophase HA than micron structured ceramics (including micron HA) and other conventional orthopedic implant materials [3-7]. For example, Webster et al. demonstrated significantly enhanced osteoblast adhesion and inhibited fibroblast (cells that contribute to forming a fibrous tissue capsule) adhesion on nanophase HA (67 nm grain size) compared to conventional HA (179 nm grain size) after 4 h of cell culture [3]. In addition, in vivo studies

demonstrated complete osseointegration of tantalum coated with nanophase HA after 2 weeks whereas tantalum coated with conventional (or micron) HA took up to 8 weeks [7]. Recently, Venugopal et al. electrospun a fibrous polycaprolactone (PCL)/HA/gelatin nanocomposite and demonstrated that osteoblast proliferation, alkaline phosphatase activity and mineralization were the greatest on the most flexible PCL/HA/gelatin nanocomposite when compared to the other PCL scaffolds [4].

Due to above mentioned excellent properties of nanocrystalline HA, it was combined with biologically-inspired RNTs for the following purposes: 1) It is anticipated that nanocrystalline HA and RNTs can enhance osteoblast adhesion by mimicking the natural HA/collagen self-assembly in bone; 2) HA nanoparticles can also increase the mechanical properties of novel scaffolds to match those of natural bone; 3) The osteoconductive HA can specifically bond to bone defect sites and increase bone mass quickly; and 4) the degradable nano HA can be functionalized with the knuckle region of BMP-2 and, thus, control the release of the knuckle region of BMP-2 to increase bone mass.

3.2 Research Objectives

This chapter focused on fabricating a biomimetic nanocrystalline HA/RNT-K orthopedic composite and determining its cytocompatibility and mechanical properties when incorporated into pHEMA hydrogels or when coated on conventional implant materials (i.e., titanium).

In this study, a wet chemistry precipitation method, which enabled good control of the crystalline phase and surface morphology of HA at the micrometer and nanometer levels, was used to synthesize HA [7-9]. Since grain size is one of the most important factors that may influence the growth of osteoblasts on implant materials, several grain sizes of nanocrystalline HA were fabricated here by utilizing different sintering temperatures or hydrothermal treatment regimes. Then, osteoblast responses on different grain sizes of nanocrystalline HA and RNT-K were determined when used as a coating on titanium.

Moreover, considering that agglomeration of nanometer crystals of HA in polymers may potentially decrease scaffold cytocompatibility and mechanical properties, well-dispersed nanocrystalline HA at different weight ratios (specifically, 2%, 10% and 20%) in RNT-K hydrogels were prepared. The mechanical and cytocompatibility properties of the biomimetic nanocrystalline HA in RNT-K hydrogels were investigated for the first time in this study. Lastly, direct HA nucleation and mineralization on RNTs and respective cell responses were investigated as well.

3.3 Materials and Methods

3.3.1 Synthesis of Nanocrystalline HA

As shown in Equation (1), nanocrystalline HA was synthesized by a wet chemistry method [7-9]. Briefly, 37.5 mL of a 0.6M ammonium phosphate (Sigma-Aldrich) solution was mixed with 375 mL of ddH_2O while ammonium hydroxide (Fisher Scientific) was used to adjust the solution pH to around 10. Then, 45 mL of a 1M calcium nitrate (Sigma-Aldrich) solution was slowly (~3.6 mL/min) dripped into the above mixture (that is, at 1:10:0.67:1.2 volume ratios of $(NH_4)_2HPO_4$: H_2O : NH_4OH : $Ca(NO_3)_2$) over 12 min while stirring. HA precipitation occurred immediately and was allowed to continue for 10 min without stirring. After removing 25% of the supernatant by centrifugation, HA precipitates were treated hydrothermally at 200 ℃ for 20 h in a 125 mL Teflon liner (Parr Instrument, Figure 3.1) [10]. This hydrothermal treatment method produced small grain sizes with high crystallinity of geometrically shaped nano HA rods at relatively low temperatures but under a higher pressure [11]. After 20 h, the nanometer HA crystals were centrifuged and rinsed sequentially with ddH_2O three times, then dried at 80 ℃ for 12 h and crushed into a nano HA powder.

$$6\ (NH_4)_2HPO_4 + 10\ Ca(NO_3)_2 + 8\ NH_4OH = \mathbf{Ca_{10}(PO_4)_6(OH)_2} + 20\ NH_4NO_3 + 6\ H_2O \qquad (1)$$

Larger grain size and higher yield rates of nanocrystalline HA were obtained without hydrothermal treatment for comparison. For this, 1M calcium nitrate was slowly added to

0.6M ammonium phosphate, while ethanol was used to disperse the mixture and ammonium hydroxide to adjust the pH up to 12. The mixture was then slightly heated at 40 ℃ for 1h and HA precipitated at room temperature for 24 h. The HA white powder was obtained after washing and centrifugation and was dried similar to the method described above. Then, the HA powder was sintered at 700 ℃ for 6 h to achieve a large nanocrystalline HA grain size or at 550 ℃ for 6 h to produce a middle nanocrystalline HA grain size with irregular shapes.

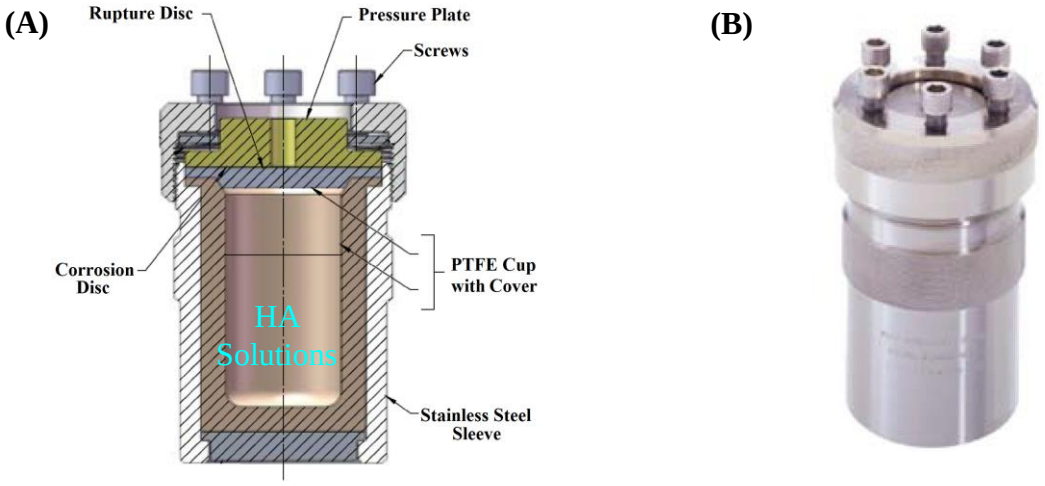

Figure 3.1 A 125 mL 4748 Parr Acid Digestion Vessel. (A) The cross section view and (B) the picture of the vessel. Figures are redrawn from [12].

3.3.2 Preparation of Nanocrystalline HA/RNT Coatings and Hydrogels

3.3.2.1 RNT-K and HA Coatings on Titanium

0.001 mg/mL of RNT-K solution was prepared as described in section 2.3.1.1. Then, the solution was sterilized with a 0.22 μm syringe filter before coating on titanium. Titanium

(Ti, 99.2% pure, Alfa Aesar) was cut to sizes of 1cm×1cm×0.2cm. They were cleaned by first soaking in acetone for 15 min, then sonicating for 15 min. This was followed by three rinses with ddH_2O. Similarly, they were then soaked in 70% ethanol, sonicated for 15 min and sequentially rinsed by ddH_2O. Lastly, they were soaked in ddH_2O, sonicated for another 15 min and rinsed. Substrates were then put into a drying oven overnight and autoclaved for sterilization before coating with RNTs and cell experiments.

250 mg of each type of nanocrystalline HA (specifically, small, middle and large HA grain sizes) was mixed with 5 mL of 70% ethanol and sonicated for 20 min to obtain a well-mixed HA solution. Then, 5 mL of 0.001 mg/mL RNT-K solution was added into each of the above mixtures. Nano HA and RNT-K mixtures were coated on the titanium surface by absorption for 45 min at room temperature and dried overnight. In addition, 0.001 mg/mL RNT-K without HA was coated on titanium. Uncoated titanium served as controls.

3.3.2.2 Nanocrystalline HA in RNT-K Hydrogel Composites

In addition to coating nanocrystalline HA and RNT-K on titanium, they were also dispersed into pHEMA hydrogels in this chapter. For this purpose, two types of nanocrystalline HA (prepared by the hydrothermal treatment or sintered at 550℃ methods) were added into the HEMA monomer (Polysciences, PA), 2,2’-azobisisobutyronitrile (free radical initiator, Sigma-Aldrich) and RNT-K solution to provide 2%, 10% and 20% ceramic/polymer weight ratios. In order to obtain

well-dispersed nanocrystalline HA hydrogel composites, the nanocrystalline HA was first sonicated in the HEMA solution using a Misonix sonicator 3000 (Misonix Inc., NY) for 12 min and 30 min. 0.01 mg/mL RNT-K and 2,2'-azobisisobutyronitrile were then added into the above mixtures, mixed thoroughly and heated at 78℃ for less than 1 h to polymerize (as described in section 2.3.1.2). After polymerization, the nanocrystalline HA/RNT-K hydrogel composites were cut into circular samples with a 1.55 cm diameter and 2 mm thickness.

2% nanocrystalline HA in hydrogels, 0.01 mg/mL RNT-K coated hydrogels and unmodified hydrogels were used as controls in the following experiments. 2% nanocrystalline HA in hydrogels were prepared by replacing the RNT-K with water in the above procedure. For the 0.01 mg/mL RNT-K coated hydrogels, hydrogels were soaked in 0.01 mg/mL RNT-K at room temperature for 45 min. For unmodified hydrogels, 2,2'-azobisisobutyronitrile, the same volume amount of HEMA monomer and water were heated in an oven at 78℃ for 1 h and cut into the same size as above. In addition, agglomerated 2%, 10% and 20% (wt.%) nanocrystalline HA in RNT-K hydrogels were prepared in a similar way to the well-dispersed nanocrystalline HA in RNT-K hydrogels except using a vortex mixer (Fisher Scientific) to mix the entire reaction solution without ultra-sonication. Finally, all of the resulting hydrogel composites and controls were soaked in water at room temperature for 30 min. Then, the various substrates were sterilized in 70% ethanol for 20 min and evaporated overnight before cell experiments.

3.3.3 Nanocrystalline HA Powder, RNT-K Coating and Hydrogel Nanocomposite Characterization

The crystallinity of nanophase HA powders was characterized by X-ray diffraction (XRD, Siemens Diffraktometer D5000 Kristalloflex; Bruker AXS Inc.). The diffraction angles (2θ) ranged from 20° to 70° at 0.02° s^{-1} for middle and large grain sizes of nanophase HA (prepared by sintering at 550 ℃ and at 700 ℃) and 0.4 ° s^{-1} for small grain sizes of nanophase HA (prepared by hydrothermal treatment). Diffraction signal intensity was monitored and processed using Diffrac^{Plus} software (Bruker AXS Inc.). In addition, the agglomerated mean particle sizes of these nano HA materials were examined by a particle size analyzer (Nano ZS, Malvern Instruments).

Nanocrystalline HA and RNT-K morphologies were characterized using a TEM (Philips, EM410 PW6008) at a 120 kV acceleration voltage. For this purpose, 0.01 mg/mL RNT-K and nanocrystalline HA were separately absorbed onto carbon-coated copper grids (EM Sciences). RNT-K coated grids were negatively stained with 2% aqueous uranyl acetate (EM sciences) for 20 s. In order to image the interaction between nanocrystalline HA and RNTs, nanocrystalline HA was further adsorbed onto the above RNT-K coated copper grids. After drying, all sample grids were imaged under TEM.

A SEM (LEO 1530-VP) operating at 3 kV accelerating voltage was used to characterize agglomerated and well-dispersed nanocrystalline HA in RNT-K hydrogels. The dehydrated composite substrates were sputter-coated with a thin layer of gold–palladium

using a PS-2 coating unit (International Scientific Instruments) in an argon environment for 3 min. SEM images of the top and bottom as well as cross sectional area of different nanocomposites were taken.

3.3.4 Cell Testing

The same osteoblast cell line described in section 2.3.3.1was used and cultured here. For the nanocrystalline HA and RNT-K used as coating materials, osteoblast adhesion was determined on: (1) 0.001 mg/mL RNT-K with the small grain size nanocrystalline HA (prepared by the hydrothermal treatment) coated on titanium, (2) 0.001 mg/mL RNT-K with the middle grain size nano HA (prepared by sintering at 550 ℃) coated on titanium, (3) 0.001 mg/mL RNT-K with the large grain size nanocrystalline HA (prepared by sintering at 700 ℃) coated on titanium, (4) 0.001 mg/mL RNT-K alone coated on titanium, and (5) uncoated titanium.

For the nanocrystalline HA in RNT-K hydrogels, seven substrates were tested: (1) 2% nanocrystalline HA (prepared by the hydrothermal treatment) in RNT-K hydrogels, (2) 2% nanocrystalline HA (prepared by the sintering method at 550 ℃) in RNT-K hydrogels, (3) 10% nanocrystalline HA (prepared by the sintering method at 550 ℃) in RNT-K hydrogels, (4) RNT-K coated hydrogels, (5) 2% nanocrystalline HA (prepared by the hydrothermal treatment) in hydrogels, (6) 2% nanocrystalline HA (prepared by the sintering method at 550 ℃) in hydrogels, and (7) hydrogel controls. 0.01 mg/mL RNT-K was used in the above RNT-K hydrogels. The 2% and 10% were weight ratios of nano HA in hydrogels.

Osteoblasts were seeded onto the above coatings, nanocomposites and control substrates of interest in this study at a density of 3500 cells/cm^2 and were cultured under standard cell culture conditions for 4 h. After the prescribed time period, cells were rinsed by several PBS washings. Then, the remaining cells were double fixed, stained with rhodamine-phalloidin (Molecular Probes) and DAPI (Invitrogen), and counted under a fluorescence microscope as described in section 2.3.3.2. Experiments were run in triplicate and repeated three separate times for each sample.

3.3.5 Mechanical Testing

The tensile and compressive mechanical properties of the 2% nanocrystalline HA/RNT-K hydrogel composites and hydrogel controls were determined using an Instron 5882 mechanical tester (Instron, Norwood, MA). 2% nanocrystalline HA prepared by sintering at 550 ℃ was first ultra-sonicated in HEMA solutions for 12 min. Then, they were mixed with a 0.01 mg/mL RNT-K solution and respective amounts of the free radical initiator and were poured into molds to polymerize with heating at 78-80 ℃ for less than 1 h. The dog bone shaped samples and cylindrical samples were used for tensile and compressive tests, respectively (Figure 3.2). The scaffolds were soaked in water for one day before measurements. The initial cross-sectional area and thickness of each sample were measured before testing. The extension and compression rates were 15 mm/min and 1 mm/min. The stress–strain curves were plotted by Microsoft Excel. The ultimate tensile stress (defined as the maximum load divided by the cross-sectional area of the sample)

was measured directly from the tensile stress–strain curve. The compressive and tensile moduli were calculated from the slope of the initial linear region of the respective stress–strain curves.

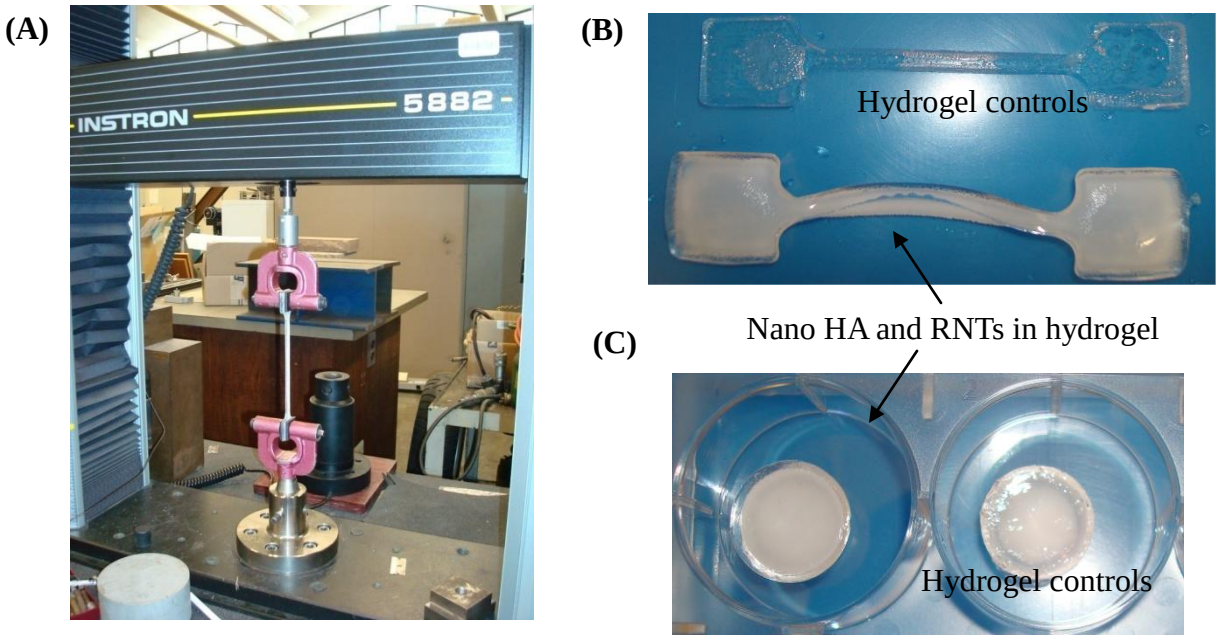

Figure 3.2 Mechanical testing. (A) A tensile test of 2% nanocrystalline HA in RNT-K hydrogels using an Instron 5882 mechanical tester. (B) The dog bone shaped nanocrystalline HA in RNT hydrogels and control samples used for tensile tests. (C) The cylindrical nanocrystalline HA in RNT hydrogels and control samples used for compressive tests.

3.3.6 Hydroxyapatite Nucleation on RNTs

Besides mechanically mixing pre-synthesized nanocrystalline HA with RNTs, the mineralization properties of RNTs by directly nucleating HA crystals were investigated here as well. For this, 10 μL of a 0.1 mg/mL RNT-K solution was mounted on a 300 mesh carbon grid (EM Science) and dried after 8 s with Whatman filter paper. 5 μL of 10 mM $CaCl_2$ (Sigma-Aldrich) was coated on the grid adsorbed with RNT-K for 1 min [13]. 5 mM Na_2HPO_4 (EMD) was then added to the back side and left to mix by passing through

the holes of the carbon grid for 2 min. Controls were also prepared by the same procedure but without RNT-K on the grids. Images of HA nucleation on the RNT-K coated grids as well as all the respective controls were obtained by Jose Rodriguez using a Hitachi S 4800 SEM from the National Institute for Nanotechnology in Edmonton, Canada. In addition, osteoblast adhesion was investigated on these HA precipitated RNTs and control grids by using the same method as described in section 3.3.4.

3.3.7 Statistics

Data were represented by the mean value with the standard error of the mean (SEM). A student's t-test was used to check statistical significance between means and $p<0.1$ was considered statistically significant.

3.4 Results and Discussion

3.4.1 Characterization of Nanocrystalline HA, Nanocrystalline HA/RNT Coatings and Hydrogels

3.4.1.1 Characterization of Nanocrystalline HA

In this chapter, different grain sizes and morphologies of nanocrystalline HA were synthesized using two treatment methods. TEM images showed that the hydrothermally treated nanocrystalline HA possessed regular rod-like nanocrystals within the range of 50-100 nm in length and 20-30 nm in width (Figures 3.3A and 3.3B). Nanocrystalline HA prepared by sintering at 700 ℃ for 6 h also had rod-like morphologies but of a larger size (~100-170 nm in length and 20-30 nm in width, Figure 3.3E). In addition, sintering HA powers at 550 ℃ for 6 h produced a middle grain size of irregular shaped nanocrystallized HA with a more agglomerated morphology (Figure 3.3C and 3.3D). Figure 3.3F showed that HA precipitates did not have clear demarkation lines or regular shapes before the hydrothermal treatments or sintering methods.

Furthermore, by measuring the sizes of nanocrystalline HA in TEM images, Figure 3.4 provided quantified results of the average HA grain sizes after hydrothermally treatment and sintering which demonstrated that hydrothermal treatment yielded much smaller crystallite sizes than other methods. Specifically, the nanocrystalline HA prepared by the

hydrothermal treatment had an average grain size of 82.8 nm (in length) while nanocrystalline HA particles prepared by sintering methods at either 550 ℃ or 700 ℃ had average grain sizes of 90.0 nm and 129.8 nm, respectively. Moreover, consistent with previous studies [14,15], all types of nanocrystalline HA agglomerated into micron sizes and hydrothermally prepared nanocrystalline HA agglomerated into smaller sizes than sintered nanocrystalline HA. Specifically, hydrothermally treated HA and HA sintered at either 550 ℃ or at 700 ℃ had ~1.51, 3.32 and 1.61 μm agglomerated mean particle sizes (Table 3.1), respectively. The agglomerated sizes of the irregular nanocrystalline HA sintered at 550 ℃ were two times higher than that of the rod-like nanocrystalline HA prepared by hydrothermally treatment or sintering at 700 ℃. A previous study demonstrated that conventional (or micron) HA agglomerated up to 169 μm [15]. The significant larger agglomeration size of the middle grain sizes nanocrystalline HA may be due to the more irregular HA shapes and possibly greater hydrophobic surface chemistry that increased agglomeration after sintering at 550 ℃ when compared to the regular rod-like hydrothermal HA. Moreover, Table 3.1 showed that sintering HA precipitates to either 550 ℃ or 700 ℃ achieved higher yield rates of nanocrystalline HA (86.46% and 83.51%, respectively) than nanocrystalline HA prepared by hydrothermal treatments (69.54%). The longer HA precipitation time (24 h) before sintering most likely contributed to the higher yield rates of nanocrystalline HA prepared by sintering (whereas only a 10 min precipitation was used during the hydrothermal treatment).

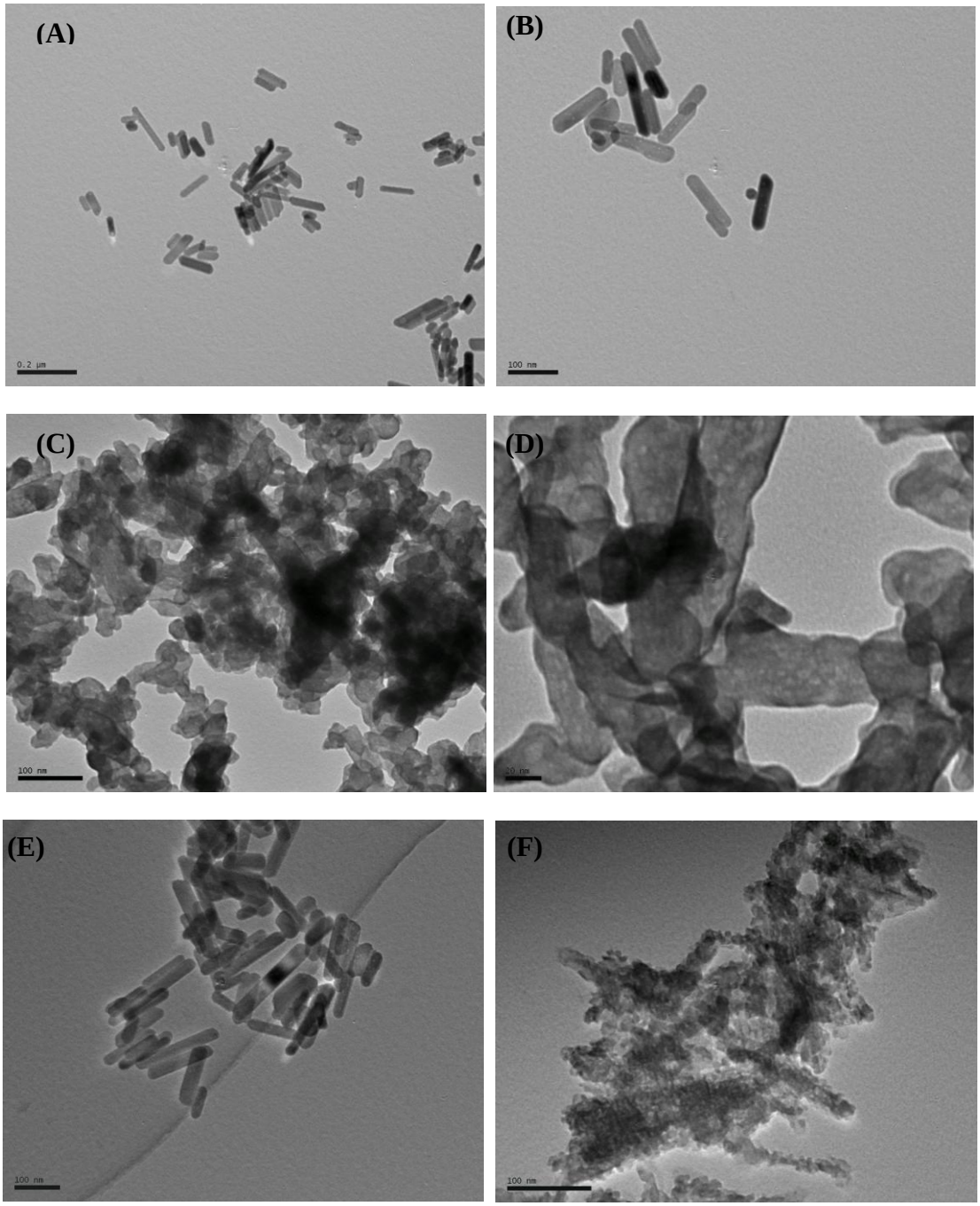

Figure 3.3 TEM images of various nanocrystalline HA and HA precipitates. (A) and (B) small grain size nanocrystalline HA (prepared by hydrothermal treatment) at different magnifications, (C) and (D) middle grain size nanocrystalline HA (prepared by sintering at 550 ℃) at different magnifications, (E) large grain size nanocrystalline HA (prepared by sintering at 700 ℃), and (F) HA precipitates before sintering. Scale bars are 200 nm, 100 nm and 20 nm.

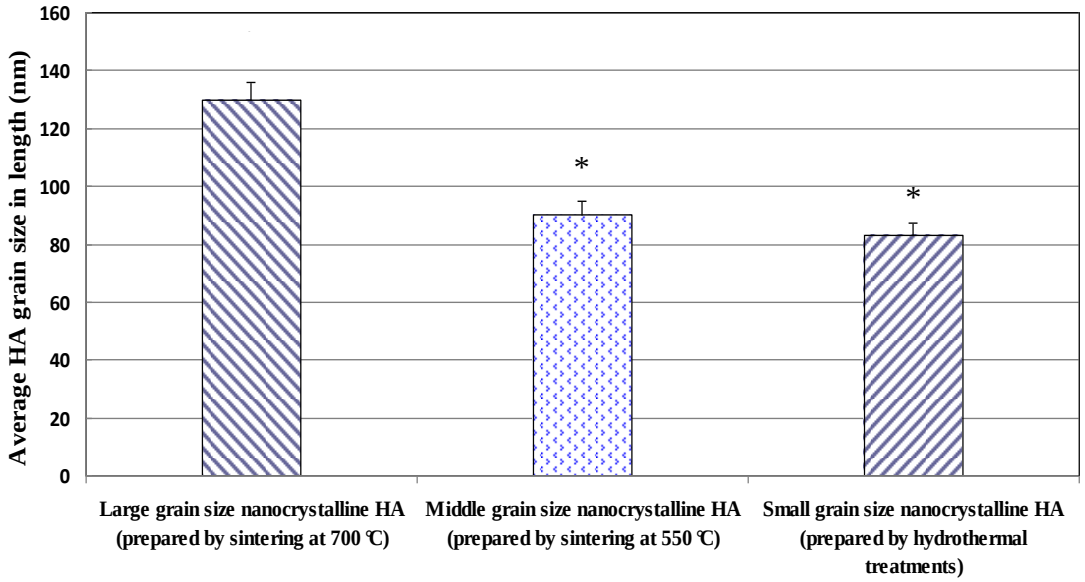

Figure 3.4 The comparison of the average grain sizes of nanocrystalline HA under different synthesis treatments. Data are mean ±SEM; n=50. **p<0.0001* when compared to large grain size nanocrystalline HA (prepared by sintering at 700 ℃).

Table 3.1 Summary of the nanocrystalline HA yield rates, agglomerated and grain sizes. Data are mean ± SEM. *p<0.001 compared to nano HA prepared by sintering at 550 ℃.

	Yield rates	Agglomerated mean size (nm)	Average grain sizes (nm)
Small grain size nanocrystalline HA (hydrothermally treated at 200 ℃ for 20 h)	**69.54%**	**1512.5 ± 180.6***	**82.8 ± 4.3**
Middle grain size nanocrystalline HA (prepared by sintering at 550 ℃ for 6h)	**86.46%**	**3323.5 ± 269.4**	**90.0 ± 4.7**
Large grain size nanocrystalline HA (prepared by sintering at 700 ℃ for 6h)	**83.51%**	**1609.9 ± 166.5***	**129.8 ± 6.0**
HA precipitates (before hydrothermal treatment or sintering)	—	**2278.6 ± 496.4**	**113.6 ± 6.3**

In addition, XRD patterns provided evidence that crystalline HA was present in all particles (Figure 3.5). Hydrothermally treated nanocrystalline HA displayed small amounts of peak broadening (Figure 3.5A) which supported previously mentioned data of smaller crystallite sizes of hydrothermally prepared nano HA compared to the other two types of sintered nano HA (Figures 3.5B and 3.5C).

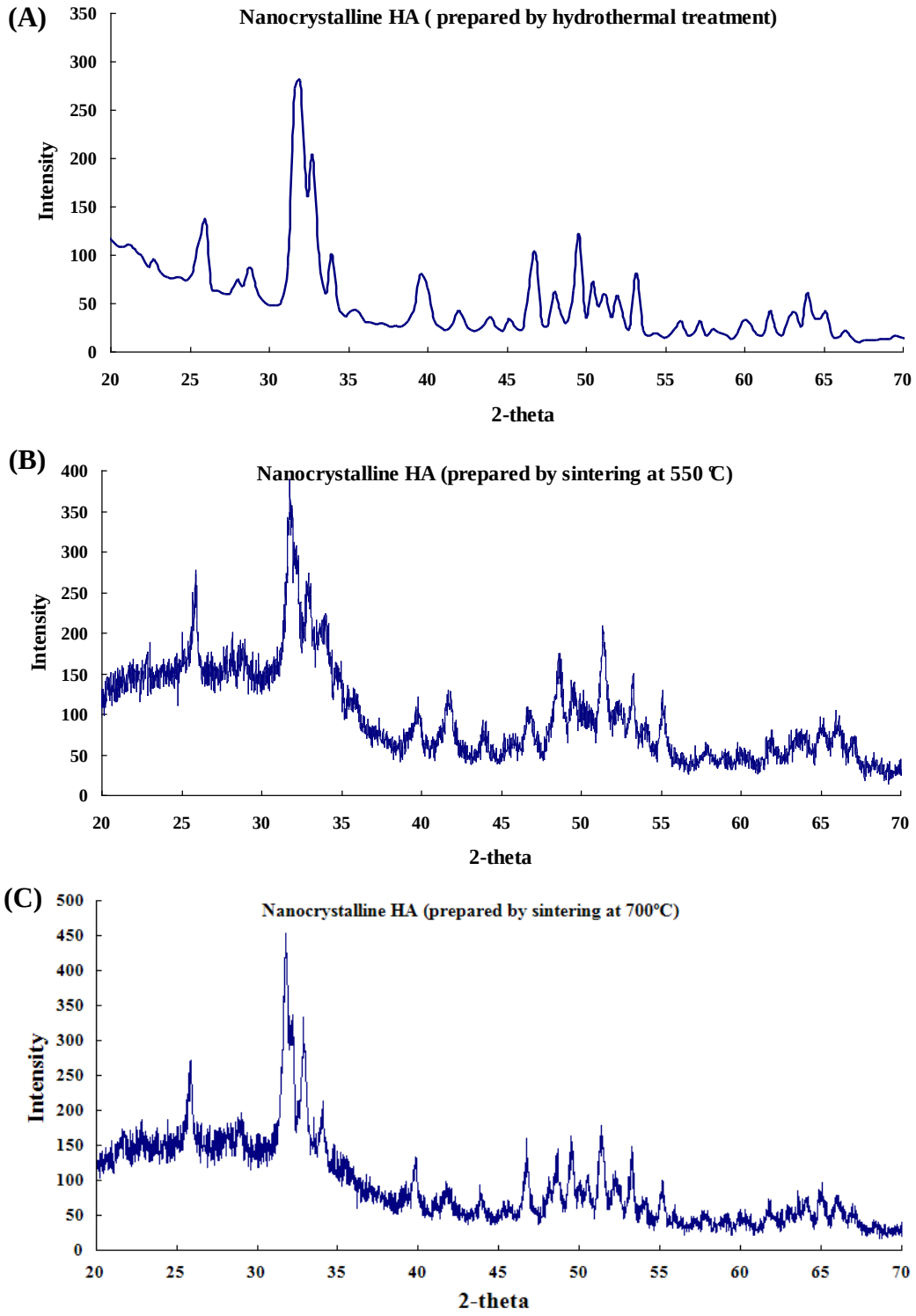

Figure 3.5 XRD pattern of nanocrystalline HA. (A) Small grain size nanocrystalline HA (prepared by hydrothermal treatment), (B) middle grain size nanocrystalline HA (prepared by sintering at 550 ℃), and (C) large grain size nanocrystalline HA (prepared by sintering at 700 ℃).

3.4.1.2 Morphology of Nanocrystalline HA/RNT Coatings

The morphology of RNT-K and nanocrystalline HA/RNT-K are shown in Figure 3.6. Bundles of the self-assembled RNT networks were observed in Figure 3.6A. Most importantly, Figure 3.6B showed for the first time a good affinity between RNT-K and nanocrystalline HA. Specifically, a bundle of RNT-K attached and oriented on the nanocrystalline HA surfaces by simple adsorption. However, the agglomeration of nanocrystalline HA was clearly observed in the TEM image.

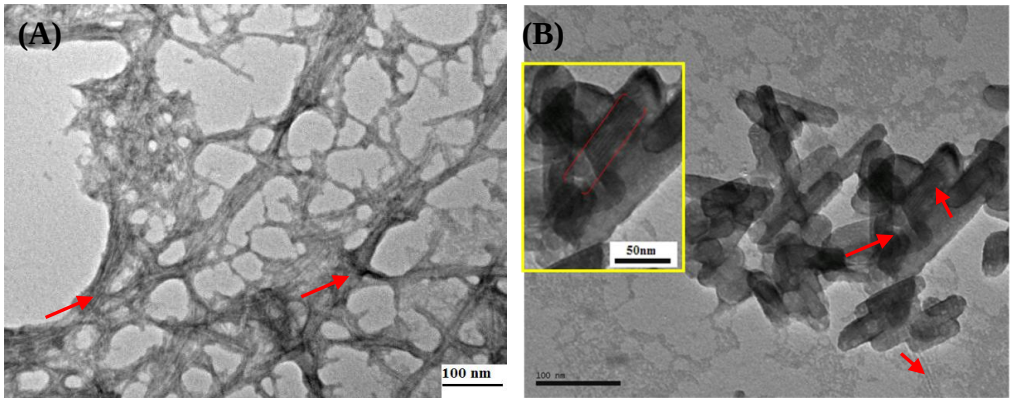

Figure 3.6 TEM images of nanocrystalline HA/RNT-K. (A) Bundles of 0.01 mg/mL RNT-K. (B) RNT-K with nanocrystalline HA prepared by hydrothermal treatment; inset shows the enlarged region of (B) demonstrating the close and aligned RNT-K/HA interaction. Arrows show the RNT-K.

SEM images showed that thin layers of different size distributions of nanocrystalline HA in 0.001 mg/mL RNT-K were coated on titanium (Figure 3.7). All of the nanocrystalline HA with RNT coatings had agglomerated nanocrystallites. In addition, uncoated titanium had micron roughness with large grain sizes while small grain sizes of nanocrystalline HA with RNTs revealed dense HA rod crystallite agglomerations in the coating (Figures

3.7A and 3.7B). Middle grain sizes of nanocrystalline HA with RNT coatings also showed very dense crystallite agglomerations but irregular crystalline distributions (Figures 3.7C and 3.7D) which was consistent with previous TEM and Table 3.1 results. In contrast, large grain sizes of nanocrystalline HA with RNT-K coatings exhibited the largest HA rod crystallite assemblies with a loose connecting pattern (Figures 3.7E and 3.7F) compared to the other coatings. TEM clearly demonstrated intimate interactions between RNTs and HA when coated on titanium.

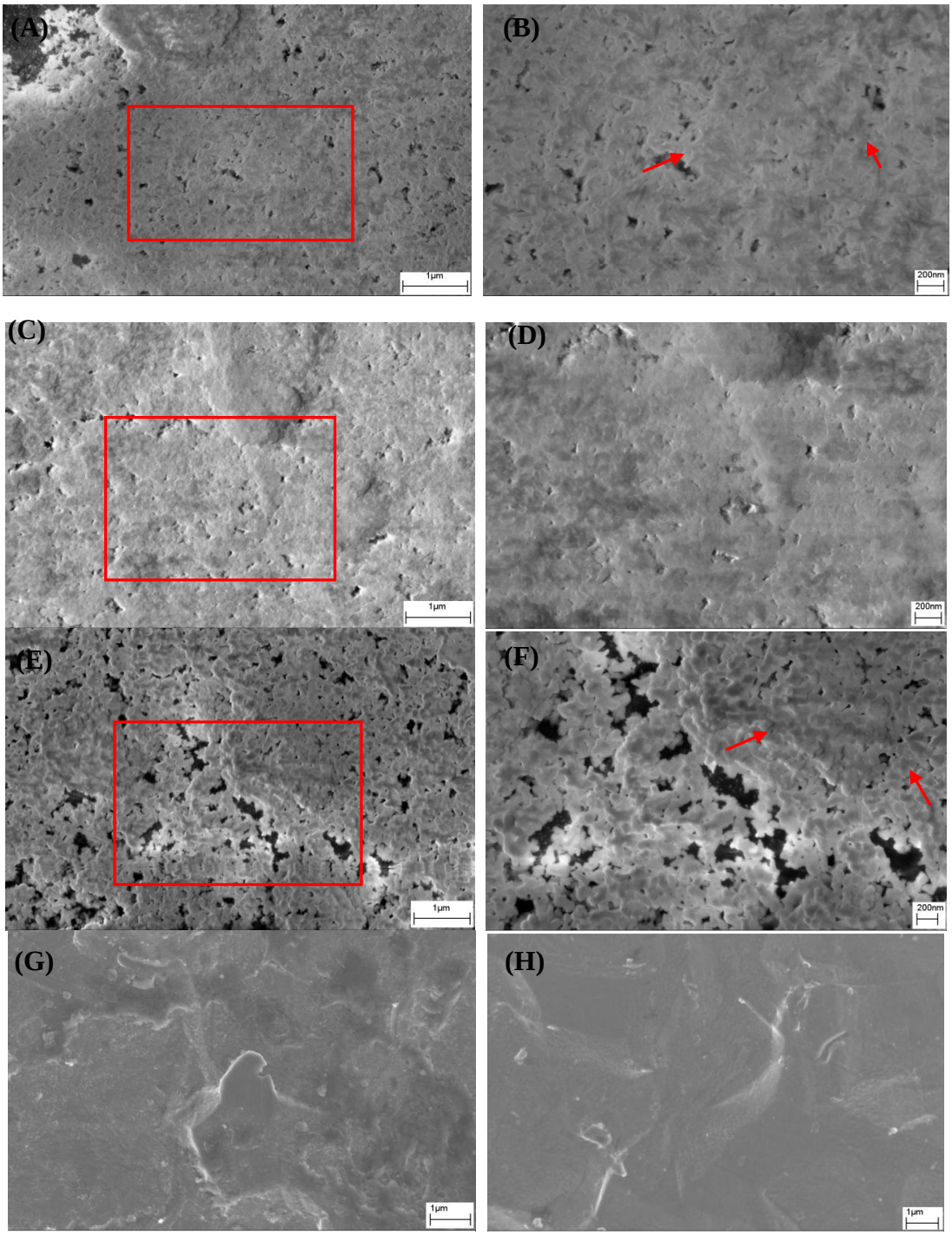

Figure 3.7 SEM micrographs of nano HA/RNT coatings. (A) Low and (B) high magnifications of small grain size nanocrystalline HA (prepared by hydrothermal treatment) with RNT-K coated on titanium. (C) Low and (D) high magnifications of middle grain size nanocrystalline HA (prepared by sintering at 550 ℃) with RNT-K coated on titanium. (E) Low and (F) high magnificaitions of large grain size nanocrystalline HA (prepared by sintering at 700 ℃) with RNT-K coated on titanium. (G) Titanium coated with RNT-K and (H) uncoated titanium. 0.001 mg/mL RNT-K was used in these coatings. Arrows show the single HA crystallites.

3.4.1.3 Morphology of Nanocrystalline HA in RNT-K Hydrogels

Increasing amounts of nanocrystalline HA particles were visible when 2%, 10% and 20% (wt%) nanocrystalline HA were added into RNT-K hydrogels (Figure 3.8). Specifically, larger amounts of agglomerated nanocrystalline HA (prepared either by hydrothermal treatment or sintering) were present at the bottom of the HA/RNT-K nanocomposites. Figures 3.8C-3.8E showed loose interactions between the agglomerated nanocrystalline HA and hydrogels. The 20% addition of nanocrystalline HA sintered at 550 ℃ in RNT hydrogels showed very dense crystallite agglomeration (Figure 3.8F) compared to respective hydrothermally treated nano HA/RNT-K hydrogels (Figure 3.8E). In addition, the cross section images (Figures 3.8G-3.8H) of the nanocomposites also revealed a non-homogeneous distribution of nanocrystalline HA throughout the RNT hydrogels. Agglomerated nano HA particles (either unevenly embed in hydrogels or those which settled down to the bottom side of the composite) were barely observed on the surface.

After ultra-sonicating nanocrystalline HA polymer solutions for 12 min (Figures 3.9A-3.9B, 3.9E-3.9F) and 30 min (Figures 3.9C-3.9D, 3.9G-3.9H), well-dispersed nanocrystalline HA/RNT-K hydrogel composites were fabricated. A too short sonication time did not yield a desirable homogenous mixture while a too long sonication time (such as over 30 min) led to larger amounts of water evaporation and an extremely viscous polymer solution. Thus, a 12 min sonication time was used in a further study to determine the mechanical and cytocompatibility properties of the materials of interest. The

homogenous distribution of nanocrystalline HA was observed in the ultra-sonicated 2% and 10% nano HA/RNT-K hydrogels. Specifically, Figures 3.9A-3.9H showed more nano HA particles on the surface of 2% and 10% nano HA/RNT-K hydrogel composites after using higher sonication powers, whereas most of the surface of the unsonicated 2% nano HA/RNT-K hydrogels lacked HA particles (Figures 3.9I and 3.9J). Furthermore, SEM images demonstrated that a large amount of nanocrystalline HA filled the inside pores of the hydrogels after ultra-sonicating (Figures 3.10A and 3.10B), which was even more than the amounts of nano HA in the 20% unsonicated nano HA/RNT hydrogel composites (Figure 3.10C).

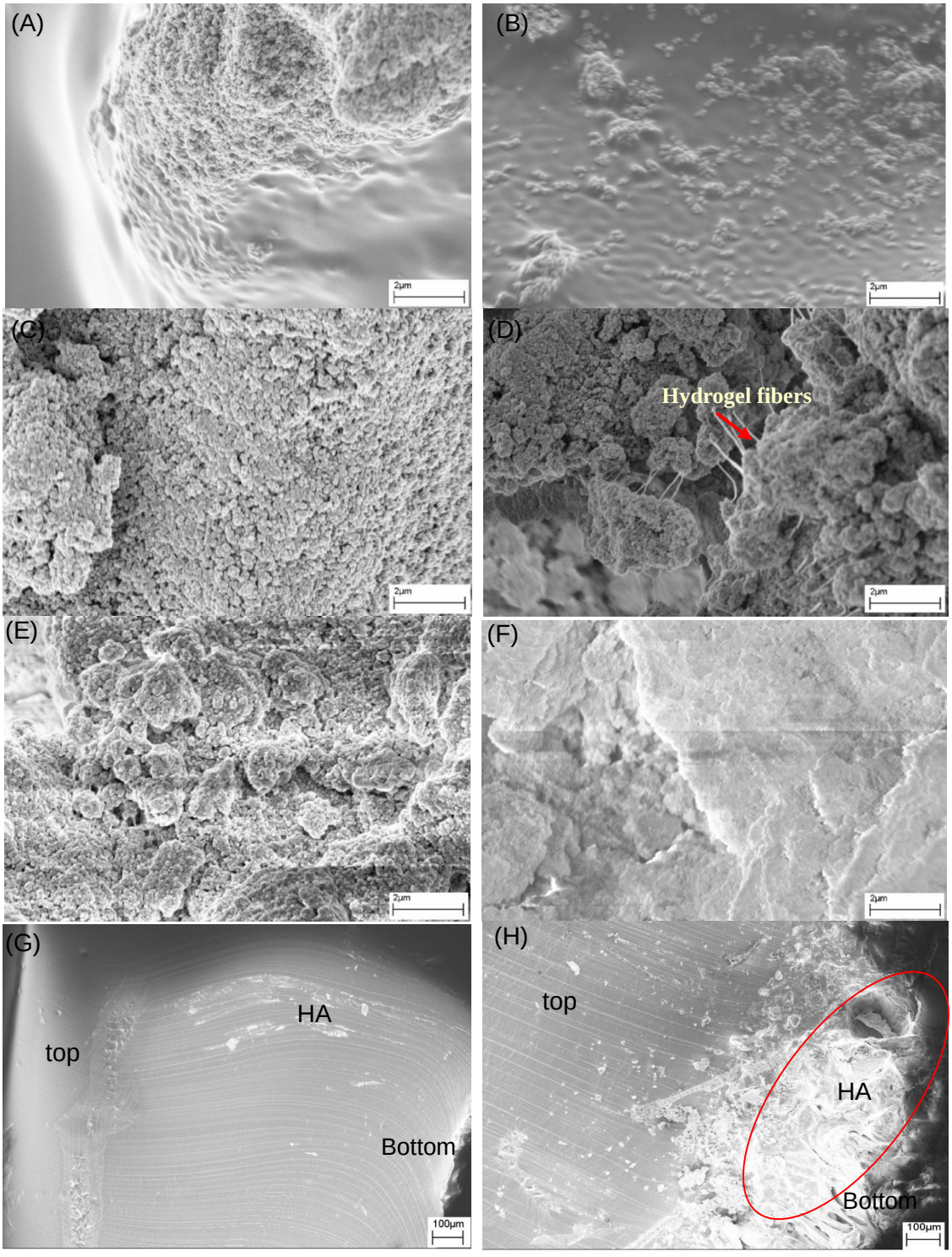

Figure 3.8 SEM images of different weight ratios of nano HA and RNT-K in hydrogels. (A) 2%, (C) 10% and (E) 20% nano HA (prepared by hydrothermal treatment) in RNT hydrogels (bottom images); (B) 2%, (D) 10% and (F) 20% nano HA (prepared by sintering at 550 ℃) in RNT hydrogels (bottom images); (G) and (H) are the cross sections of the 2% nano HA (hydrothermal treatment) and 10% nano HA (sintering at 550 ℃) in RNT hydrogels, respectively, which demonstrated the agglomeration of nano HA.

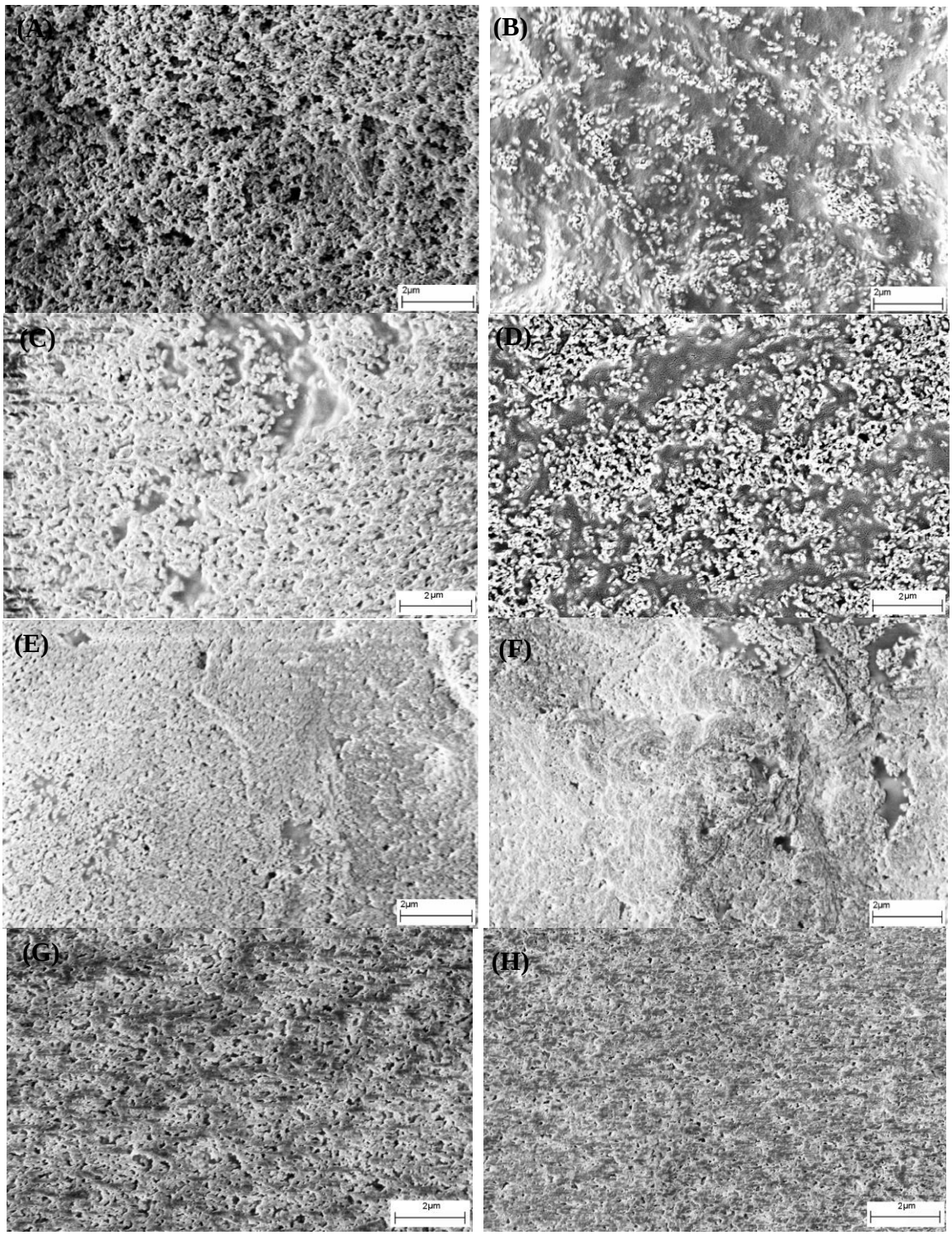
Bottom
Top
(A)
(B)
(C)
(D)
(E)
(F)
(G)
(H)
2µm

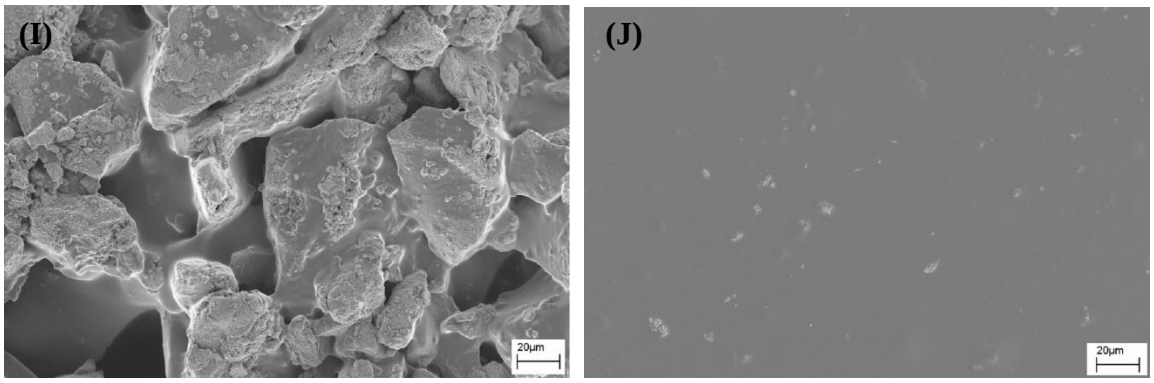

Figure 3.9 SEM images of well-dispersed small grain size nanocrystalline HA (prepared by hydrothermal treatment) and RNT-K hydrogels compared to agglomerated samples. The bottom and top images of well-dispersed 2% nanocrystalline HA in RNT-K hydrogels after ultra-sonicating for 12 min (A-B) and for 30 min (C-D); well-dispersed 10% nanocrystalline HA in RNT-K hydrogels after ultra-sonicating for 12 min (E-F) and for 30 min (G-H); (I) and (J) are unsonicated 2% nanocrystalline HA in RNT-K hydrogels which show mostly agglomerated HA at the bottom.

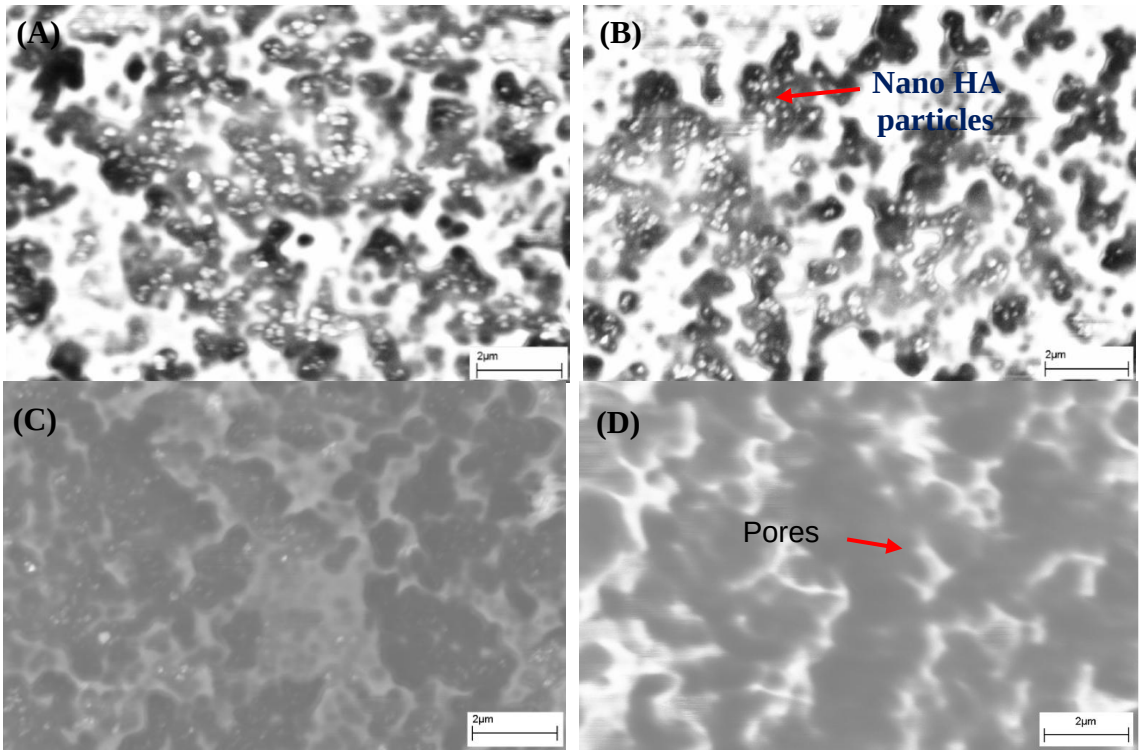

Figure 3.10 The cross sections of small grain size nanocrystalline HA in RNT-K hydrogels. (A) and (B) are the cross sections of the well-dispersed 2% and 10% nanocrystalline HA in RNT-K hydrogels after ultra-sonicating for 12 min; (C) is the unsonicated 20% nano HA in RNT-K hydrogels; and (D) is the hydrogel control.

3.4.2 Improved Mechanical Properties of Nano HA in RNT-K Hydrogels

As shown in Table 3.2 and Figure 3.11, the nanocrystalline HA in RNT-K (0.01mg/mL) hydrogel composite enhanced mechanical properties compared to the hydrogel controls. The compressive and tensile moduli of the scaffolds (Table 3.2) were determined from the compressive and tensile stress-strain curves (Figures 3.11A and 3.11B). 2% nanocrystalline HA/RNT hydrogels supported greater ultimate tensile stresses and had greater compressive and tensile moduli than hydrogel controls (Table 3.2). For example, the compressive modulus of 2% nanocrystalline HA in RNT hydrogels increased 38% compared to hydrogel controls. After ultra-sonicating, nanocrystalline HA may have reinforced the scaffold via a homogenously distribution into the hydrogels or filling pores. The improved mechanical properties of the scaffolds using nano HA in this study are important for bone tissue engineering applications and are also consistent with other reports of nanoparticles towards improving mechanical properties of polymer scaffolds [6,16]. For example, Wei et al. demonstrated that the introduction of over 30% nano HA particles into PLLA greatly increased the mechanical properties of the composite and the compressive modulus of nano HA/PLLA scaffolds increased with nano HA content [6]. Although the current mechanical properties of the composites were still lower than natural bone (i.e., the compressive modulus was ~10 MPa and 10 GPa in low-density cancellous bone and high-density compact bone, respectively [17]; The ultimate tensile strength of human femur was 124 MPa [18]), this study provided evidence that well-dispersed nanocrystalline HA in RNT-K hydrogel composites, even at a low

concentration of nanocrystalline HA, improved mechanical properties. Fundamentally, the water content, the crosslinking degree and molecular weight of the polymer may have affected mechanical properties of nanocrystalline HA/RNT polymer scaffold which needs to be the focus of future studies.

Table 3.2 Mechanical properties of nanocrystalline HA/RNT-K hydrogels and controls. Data are mean ±SEM, n=3. *p<0.05 when compared to respective hydrogel controls.

	2% nano HA in RNT-K hydrogels	Hydrogel controls
Compressive modulus (MPa)	**0.457 ± 0.028***	**0.331 ± 0.019**
Tensile modulus (MPa)	**0.333 ± 0.278**	**0.065 ± 0.030**
Ultimate tensile stress (MPa)	**0.201 ± 0.019***	**0.135 ± 0.015**

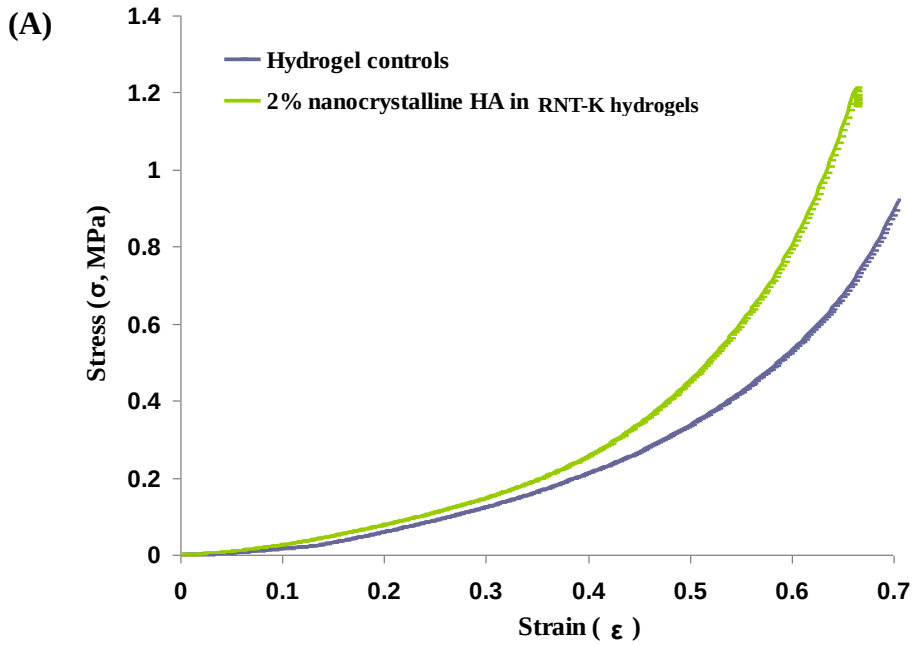

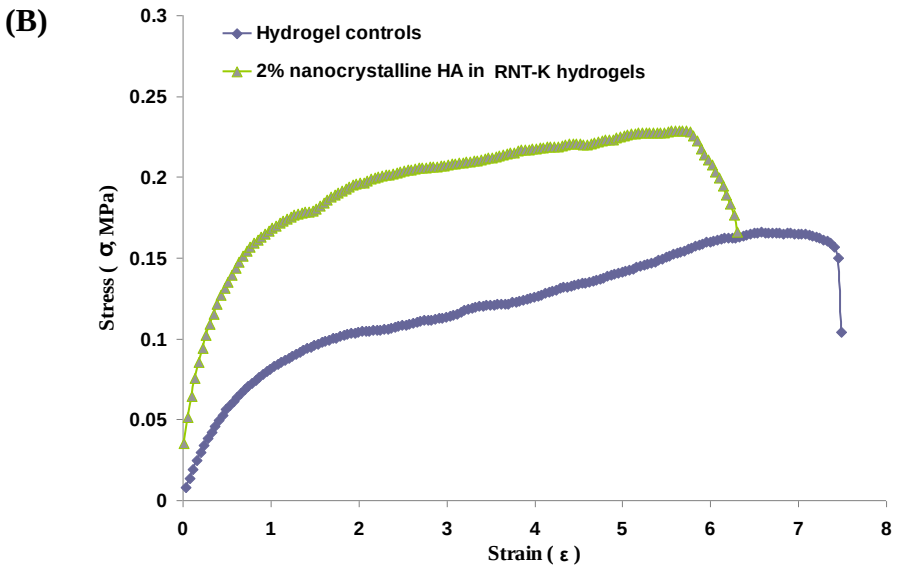

Figure 3.11 The stress and strain curves of the (A) compressive test and (B) tensile test of 2% nano HA in RNT-K hydrogels, as well as hydrogel controls.

3.4.3 Cytocompatibility Properties of Nanocomposites and Hydrogel Controls

3.4.3.1 Osteoblast Adhesion on Nano HA/RNT-K Coatings on Titanium

Results of this study also showed greater osteoblast adhesion on nanocrystalline HA/RNT-K coatings on titanium compared to uncoated titanium (Figure 3.12). Specifically, the small and middle grain sizes of nanocrystalline HA/RNT coatings increased osteoblast adhesion by 29.3% and 36.3% on titanium compared to uncoated titanium, respectively. In the present study, a grain size dependent osteoblast adhesion was also observed: i.e., the small and middle grain size nanocrystalline HA/RNT coatings increased osteoblast adhesion more than on the larger grain size nanocrystalline HA/RNT coatings. In addition, osteoblast attachment significantly improved on the 0.001 mg/mL RNT-K coated titanium (alone) which was consistent to previous studies [19].

Importantly, although the bone remodeling process in vivo includes various cell types (such as osteoblasts, osteoclasts, and osteocytes) [2], promoting initial osteoblast adhesion on orthopedic implant materials is essential for further new bone growth. Therefore, the significantly enhanced osteoblast adhesion on nanocrystalline HA/RNT coatings observed here indicated promise for the continued investigation of these biomimetic coatings for improving orthopedic implants.

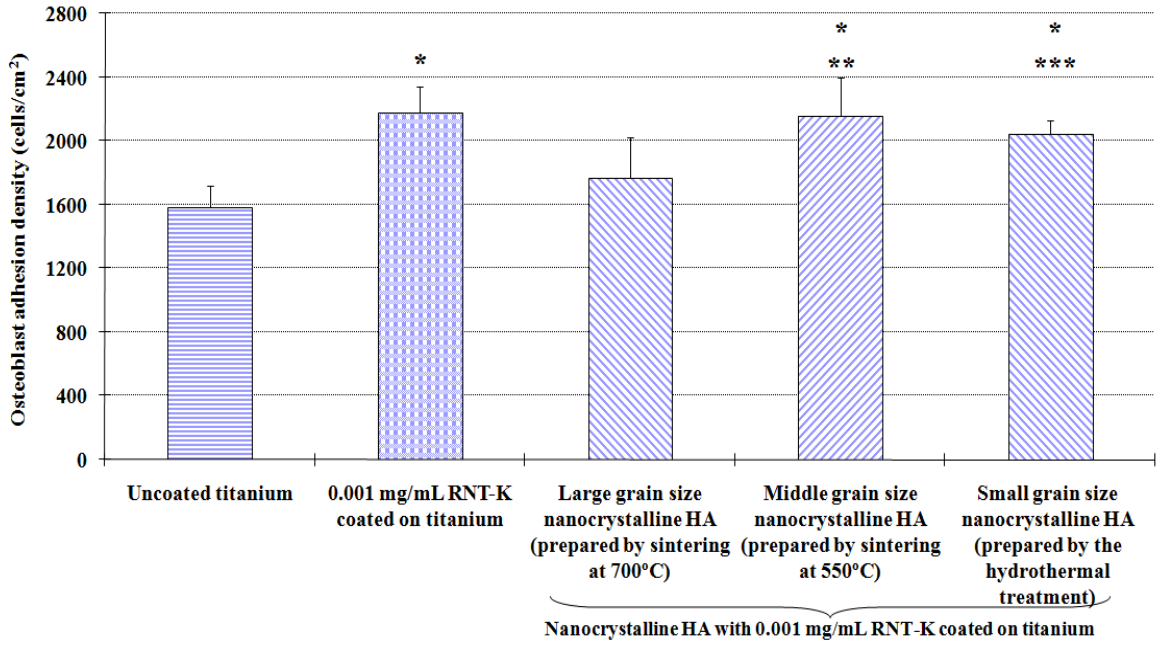

Figure 3.12 Osteoblast adhesion on HA and RNT-K coated titanium. Data are mean ±SEM; N=3. * $p<0.05$ when compared to uncoated titanium; ** $p<0.01$ and *** $p<0.1$ when compared to larger grain size nanocrystalline HA (prepared by sintering at 700 ℃) with 0.001 mg/mL RNT-K coated on titanium.

As is known, inorganic nanocrystalline HA and elastic collagen (which has helical nanostructures) assemble to form the natural bone matrix [2,20]. Thus, much effort has been devoted to apply bioactive and osteoconductive nano HA materials as coatings on

implant materials for orthopedic applications [7,10,14,15,21-28]. For instance, recently it was reported that enhanced cell functions were observed on titanium coated with nano HA by an electrochemical method [25]. However, current HA coatings still can not satisfy a patient's high expectations for orthopedic implants due to many shortcomings (i.e., lack of rapid osseointegration, low degree of crystallinity, weak interactions with titanium, etc.). In this study, it should be emphasized that novel nanotubular RNTs, which were coated with a high degree of nanocrystalline HA on titanium, not only possessed flexible functionalizable chemistries but also had biologically-inspired surface features which created a favorable bone-like environment (Figure 3.13) to possibly eventually improve osseointegration with juxtaposed bone.

In addition, although there were no statistical difference in osteoblast adhesion among the RNTs coated on titanium and nanocrystalline HA/RNT coated on titanium (due to the possibly different concentrations of exposed RNTs on their surfaces), creating a biomimetic coating on titanium is promising to promote osteoblast adhesion and long term bone tissue formation possibly contributing to lower implant failure rates. Moreover, nano HA and RNTs were coated on titanium by simple physical adsorption, which was adopted as a model coating method in this study. This coating method could be improved by using commercially available coating techniques (such as the widely used plasma-spray process, sol-gel processing, spin coating, electrospinning, newly developed IonTite^{TM} methods [14], etc.), which may contribute to more surface coverage and coating strength for orthopedic applications.

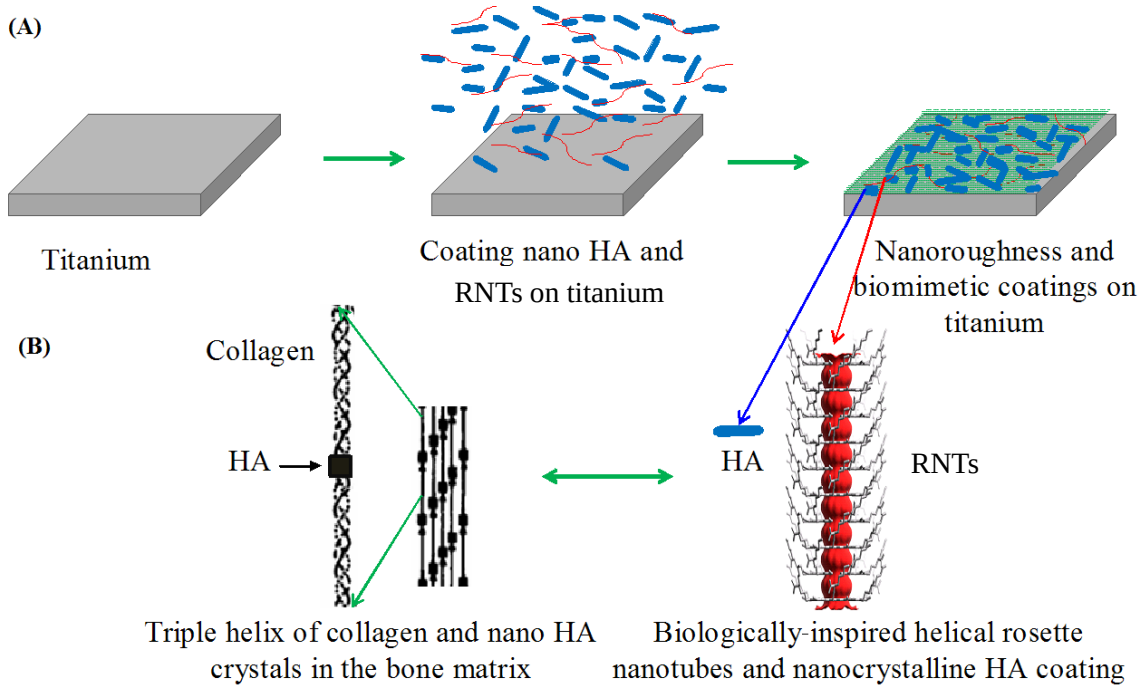

Figure 3.13 A biologically-inspired nanocrystalline HA/RNT coating. (A) The schematic illustration of coating nano HA/RNT on titanium, (B) the nanostructured HA/RNT coating mimics the natural bone matrix which consists in part of triple helices of collagen assembled with nanocystalline HA.

In the current study, the concentration of RNTs that osteoblasts interacted with was below 0.001 mg/mL due to dilution effects of co-coating RNTs and HA (e.g., some RNTs may be underneath the HA and not exposed on the surface). Since it has been demonstrated that higher concentrations of RNTs on hydrogels (such as 0.01 mg/mL) can enhance osteoblast adhesion compared to low RNT concentration coatings as described in previous section 2.4.2, it anticipated that increasing RNT-K concentration on the HA/RNT coating can further augment osteoblast adhesion.

3.4.3.2 Osteoblast Adhesion on Nano HA in RNT-K Hydrogels

Due to the positive cell responses on the biomimetic nano HA and RNT coatings observed in the above section, the cytocompatibility properties of nanocrystalline HA in higher concentrations of RNT-K (such as 0.01 mg/mL) in hydrogels for orthopedic applications was also investigated here. The result of this cytocompatibility study demonstrated for the first time that when combining the biologically-inspired RNT hydrogels and nanocrystalline HA, osteoblast adhesion can be greatly improved (Figure 3.14). Specifically, osteoblast adhesion was significantly higher ($p<0.005$) on 2% nanocrystalline HA hydrogels and 0.01 mg/mL RNT-K hydrogels as well as 10% nanocrystalline HA/RNT-K hydrogel composites than hydrogel controls. Essentially, all of the scaffolds incorporating 0.01 mg/mL RNT-K enhanced osteoblast adhesion compared to nanocrystalline HA in hydrogels without RNTs. In particular, 2% nanocrystalline HA (prepared by sintering at 550 ℃) in RNT-K hydrogels had the highest osteoblast densities, which were 235% and 99% greater than hydrogel controls and 2% nanocrystalline HA (prepared by sintering) in hydrogels, respectively. This suggested that although both of the nanocrystalline HA and RNTs contributed to greater cytocompatibility properties, the biomimetic and nanostructured RNT-K played a more important role in improving the cytocompatibility properties of the nanocomposites.

In previous sections, various RNTs with different amino acids or peptide side chains (such as lysine, RGD) were shown to have the potential to increase new bone growth when incorporated into hydrogels because of their nanoscale biologically-inspired

features and rich lysine or peptide side chains. However, of course for an orthopedic application, separation of RNTs from the biomaterial may occur and possible systemic toxicity may become an issue. In this light, Journeay et al. conducted an in vivo inflammatory study on the RNTs [29] and demonstrated that an inflammatory response was not triggered at a 5 μg dose (in 50 μL of water) and even with a 50 μg dose, inflammation was resolved after 7 days. Thus, RNTs not only exhibited excellent cytocompatibility properties in vitro but also had low acute toxicity in vivo. Importantly, the present study used RNT concentrations (0.01 mg/mL) lower than those concentrations in [29], which were cytocompatible here for orthopedic applications. More importantly, this study demonstrated that the introduction of osteoconductive nanocrystalline HA and RNT-K together into the hydrogel composites further boosted the cytocompatibility properties of hydrogels, making them promising for bone tissue engineering applications.

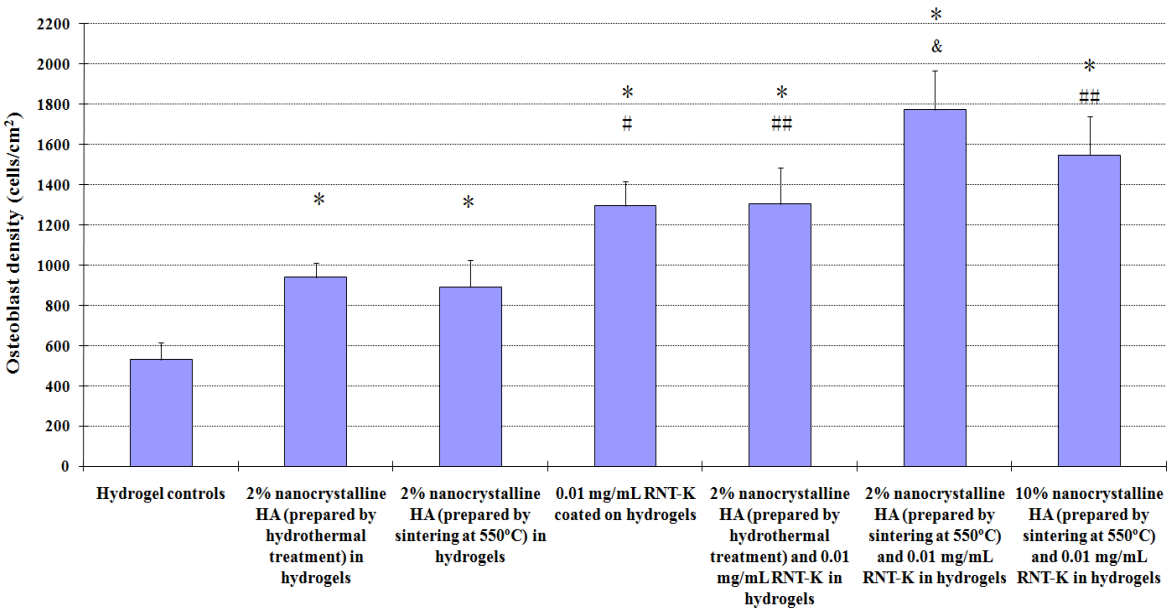

Figure 3.14 Greatly enhanced osteoblast adhesion on nanocrystalline HA/RNT-K hydrogel composites. Data are mean ±SEM, N=3. *p<0.005 compared to hydrogel controls; #p<0.005 and ##p<0.05 compared to 2% nanocrystalline HA (prepared by hydrothermal or sintering methods) in hydrogels; and &p<0.05 compared to all other scaffolds except 10% nanocrystalline HA in RNT-K hydrogels.

In addition, there were no significant differences in cell adhesion between 2% nanocrystalline HA prepared by two different methods, hydrothermal treatment or sintering at 550℃, when placed in hydrogels. However, after further introduction of nanocrystalline HA into RNT hydrogels, it was noted that the 2% nanocrystalline HA prepared by sintering at 550 ℃ attracted more osteoblasts than respective hydrothermally treated nanocrystalline HA in RNT hydrogels. This may be because nanocrystalline HA prepared by sintering at 550℃ had a slightly different surface chemistry and hydrophobicity which possibly led to more RNT adsorption and interaction than the rod-like hydrothermally treated HA, although clearly this needs further study. Furthermore, other researchers reported that increasing nano HA content (up to 30%) in polymers (such as poly(propylene fumarate)) may increase biocompatibility properties including pre-osteoblast cell adhesion and proliferation [30]. The present study did not observe a similar significant increased cytocompatibility with osteoblasts by increasing the nanocrystalline HA ratio from 2% to 10%. Since RNT-K was more effective and more important in enhancing cytocompatibility with osteoblasts than nanocrystalline HA, increasing the content of nanocrystalline HA may have minimized RNT surface coverage on hydrogel nanocomposites. Thus, 10% nanocrystalline HA (prepared by sintering at 550℃) in RNT-K hydrogels only slightly promoted osteoblast adhesion compared to RNT-K hydrogels and did not enhance the adhesion of as many osteoblasts as the 2% nanocrystalline HA (prepared by sintering at 550℃) in RNT-K hydrogels.

Moreover, results of this study showed that osteoblasts extended more filopodia and

possessed a relatively flatter and better spread shape on the 2% and 10% nanocrystalline HA in RNT-K hydrogels, 2% nano HA hydrogels and RNT hydrogels than hydrogels alone (Figure 3.15).

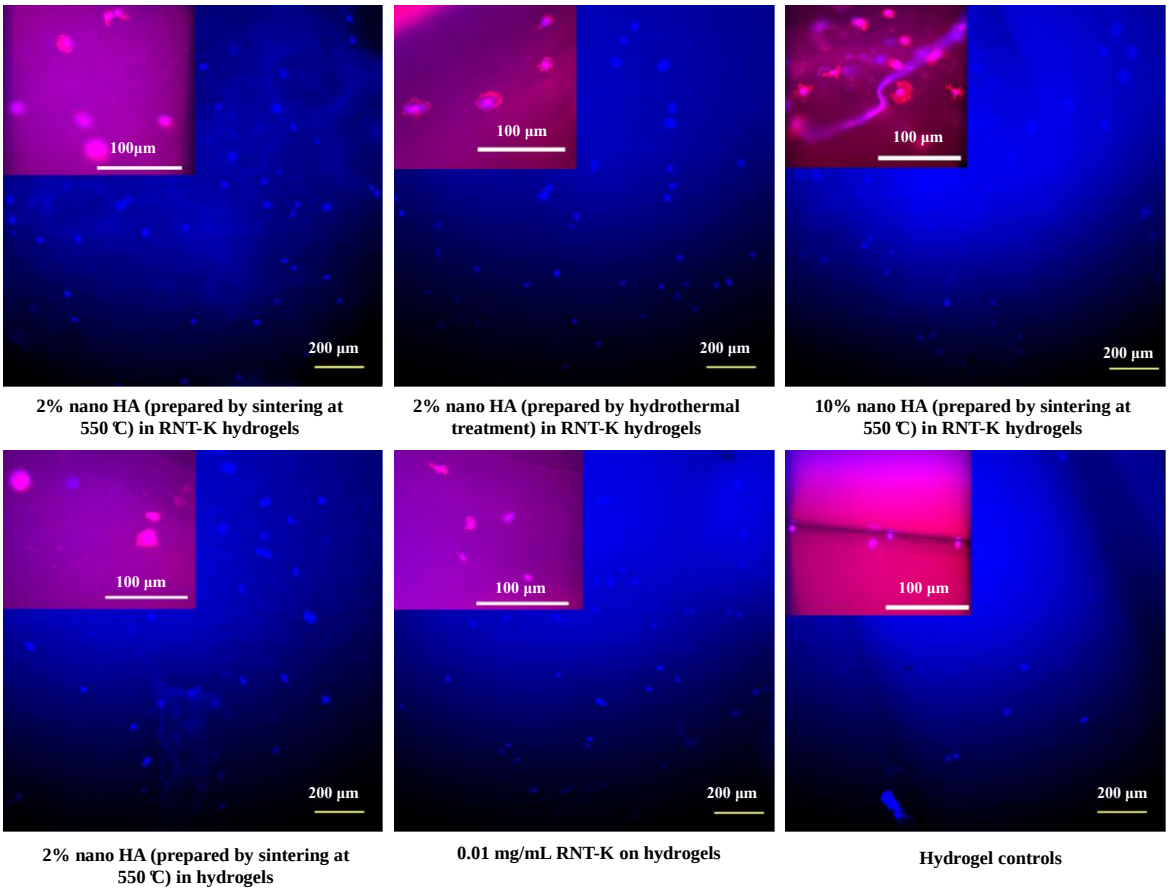

Figure 3.15 Fluorescently F-actin filament and nucleus stained osteoblasts on various nanocrystalline HA in RNT-K hydrogels and controls.

3.4.4 HA Nucleation on RNTs

For bone tissue engineering and orthopedic implant applications, the deposition, nucleation and growth of HA crystals in pores of an extracellular collagen matrix are important steps during bone remodeling in vivo. In addition, the ability of HA to nucleate in a similar fashion to what happens naturally on biomaterials is important for promoting long-term implant osseointegration. Thus, the ability of HA nucleation on RNTs was investigated here. Results demonstrated that after 2 min, HA crystals rapidly formed and regularly aligned on RNTs in a pattern similar to the HA nucleation on collagen in bone (Figure 3.16). However, randomly dispersed HA was observed on the grids without RNTs. Hartgerink et al. also demonstrated that peptide-amphiphile (PA) nanofibers can directly nucleate and align HA on the long axis of the nanofiber similar to the self-assemble pattern of collagen and HA crystals in bone [13]. However, this present study accomplished the alignment for a different self-assembly molecule (RNTs) suggesting that self-assembly nanotubes have the potential to serve as excellent biomimetic templates for HA deposition.

Lastly, the result of osteoblast adhesion experiments revealed that more osteoblasts were attached on the biomimetic RNT-K aligned with HA crystals than control grids without RNTs (Figure 3.17).

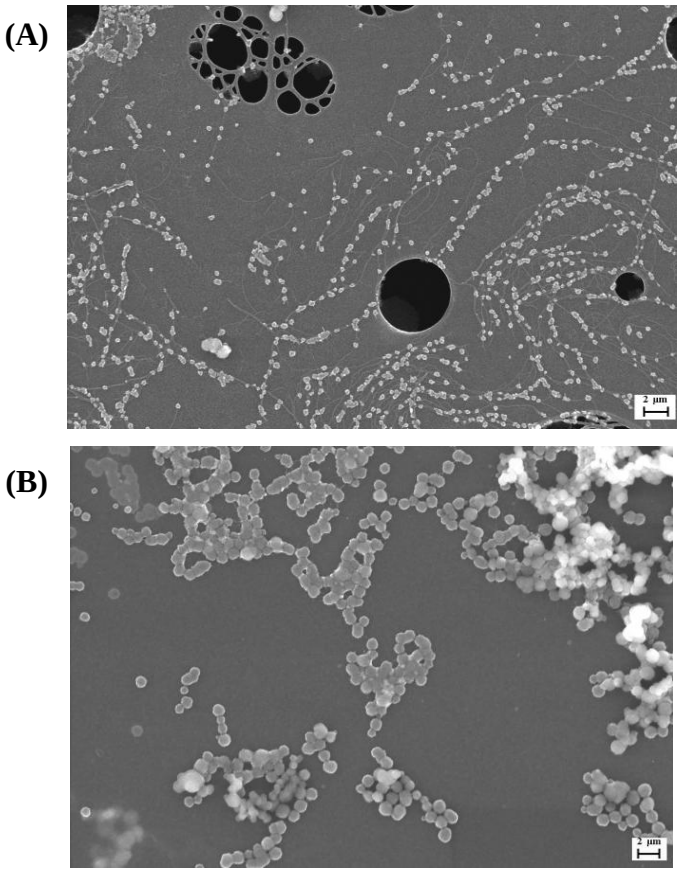

Figure 3.16 SEM images of HA nucleation. (A) Biomimetic HA nucleation on 0.1 mg/mL RNT-K on a porous carbon TEM grid and (B) only HA on TEM grid (control, 2 min reaction). Images were prepared by Jose Rodriguez from the University of Alberta.

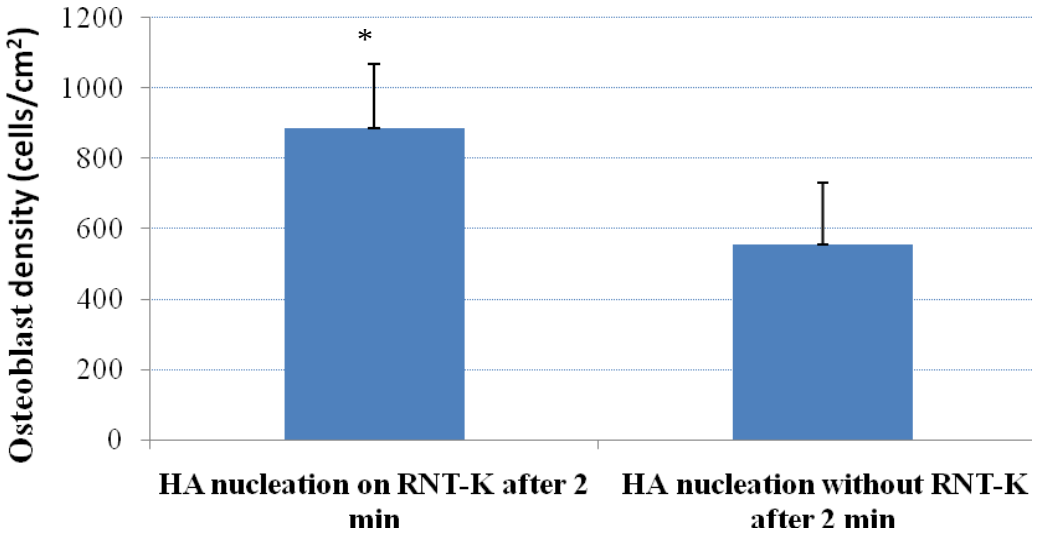

Figure 3.17 Osteoblast adhesion on HA nucleated RNT-K grid and control grids. Data are mean ± SEM, n=5. *p<0.1 compared to HA nucleation without RNTs (control).

3.5 Conclusions

In summary, different grain sizes of nanocrystalline HA were synthesized in this chapter via hydrothermal and sintering methods. They were co-coated with 0.001 mg/mL of RNT-K on titanium. The present study demonstrated that RNTs had a high affinity with nano HA. Furthermore, biomimetic nano HA/RNT coatings offer advantages over traditional orthopedic implant materials (such as uncoated titanium) by enhancing osteoblast adhesion.

In addition, nanocrystalline HA was well dispersed into 0.01 mg/mL RNT-K and pHEMA hydrogels via high power ultrasonicating. Further, the induction of nanocrystalline HA and RNTs increased the mechanical properties (such as compressive modulus, ultimate tensile stress, etc.) of the nanocomposites. Importantly, this study also provided evidence that the biomimetic nanocrystalline HA/RNT-K hydrogels, even at a low concentration of nano HA and RNTs, significantly enhanced osteoblast adhesion over hydrogel controls. Specifically, 2% nanocrystalline HA (prepared by sintering at 550℃) in RNT-K hydrogels enhanced two times more osteoblasts compared to hydrogel controls.

Lastly, this chapter also demonstrated that RNTs were an excellent template for directing HA nucleation and mineralization and, thus, further improved osteoblast adhesion. In summary, this study used RNTs and nanocrystalline HA to successfully design a novel biomimetic nanocomposite with improved mechanical and cytocompatibility properties for orthopedic applications, and, thus, should be further investigated.

3.6 References

[1] Hulbert SF, Hench LL, Forbers D, Bowman LS. History of bioceramics. Ceramics international 1982;8:131–140.

[2] Webster TJ. Nanophase ceramics: the future orthopedic and dental implant material. In: Ying JY, editor. Advances in chemical engineering. New York: Academic Press, 2001, p.125–166.

[3] Webster TJ, Ergun C, Doremus RH, Siegel RW, Bizios R. Specific proteins mediate enhanced osteoblast adhesion on nanophase ceramics. J Biomed Mater Res 2000; 51:475-483.

[4] Venugopal JR, Low S, Choon AT, Kumar AB, Ramakrishna S. Nanobioengineered electrospun composite nanofibers and osteoblasts for bone regeneration. Artificial Organs 2008;32:388–397.

[5] Chris Arts JJ, Verdonschot N, Schreurs BW, Buma P. The use of a bioresorbable nano-crystalline hydroxyapatite paste in acetabular bone impaction grafting. Biomaterials 2006;27:1110–1118.

[6] Wei G, Ma PX. Structure and properties of nano-hydroxyapatite/polymer composite scaffolds for bone tissue engineering. Biomaterials 2004;25:4749–4757.

[7] Sato M. Nanophase hydroxyapatite coatings for dental and orthopedic applications, Ph.D. thesis, School of Materials Engineering, Purdue University, West Lafayette, IN, 2006.

[8] Duan K, Wang R. Surface modifications of bone implants through wet chemistry. Journal of Materials Chemistry 2006;16:2309–2321.

[9] Lopez-Macipe A, Rodriguez-Clemente R, Hidalgo-Lopez A, et al. Wet chemical synthesis of hydroxyapatite particles from nonstoichiometric solutions. J Mater Synth Process 1998;6:21–26.

[10] Sato M, Slamovich EB, Webster TJ. Enhanced osteoblast adhesion on hydrothermally treated hydroxyapatite/titania/poly(lactide-coglycolide) sol–gel titanium coatings. Biomaterials 2005;26:1349–1357.

[11] Ioku K, Yoshimura M. Stochiometric apatite fine single crystals by hydrothermal synthesis. Phosphorus Research Bulletin 1991;1:15–20.

[12] http://www.parrinst.com/doc_library/members/249m.pdf

[13] Hartgerink JD, Beniash E, Stupp SI. Self-assembly and mineralization of peptide-amphiphile nanofibers. Science 2001;294:1684–1688.

[14] Sato M, Sambito MA, Aslani A, et al. Increased osteoblast functions on undoped and yttrium-doped nanocrystalline hydroxyapatite coatings on titanium. Biomaterials 2006;27:2358–2369.

[15] Balasundaram G, Sato M, Webster TJ. Using hydroxyapatite nanoparticles and decreased crystallinity to promote osteoblast adhesion similar to functionalizing with RGD. Biomaterials 2006;27:2798–2805.

[16] Peter SJ, Kim P, Yasko AW, Yaszemski MJ, Mikos AG. Crosslinking characteristics of an injectable poly(propylene fumarate)/b-tricalcium phosphate paste and mechanical properties of the crosslinked composite for use as a biodegradable bone cement. J Biomed Mater Res 1999;44:314–321.

[17] Fung YC. Biomechanics: Mechanical properties of living tissues. New York: Springer-Verlag, 1993, P.500-519.

[18] Yamada H. Strength of biological materials. Williams and Wilkins, Baltimore, MD, 1970.

[19] Chun AL. Helical rosette nanotubes: an investigation towards its application in orthopedics, Ph.D. thesis, Weldon School of Biomedical Engineering, Purdue University, West Lafayette, IN, 2006.

[20] Kaplan FS，Hayes WC, Keaveny TM，Boskey A，Einhorn TA, Iannotti JP. Form and function of bone. In: Sinmon SP, editor. Orthopedic basic science. American Academy of Orthopaedic Surgeons, 1994, p.127–185.

[21] Webster TJ, Ergun C, Doremus RH, et al. Hydroxylapatite with substituted magnesium, zinc, cadmium, and yttrium. II. Mechanisms of osteoblast adhesion. J Biomed Mater Res 2002;59:312–317.

[22] Choi JW, Cho HM, Kwak EK, et al. Effect of Ag-doped hydroxyapatite as a bone filler for inflamed bone defects. Key Eng Mater 2004;254–256:47–50.

[23] Bigi A, Bracci B, Cuisinier F, et al. Human osteoblast response to pulsed laser deposited calcium phosphate coatings. Biomaterials 2005;26:2381–2389.

[24] Evis Z, Sato M, Webster TJ. Increased osteoblast adhesion on nanograined hydroxyapatite and partially stabilized zirconia composites. J Biomed Mater Res 2006;78A:500–507.

[25] Narayanan R, Kim S, Kwon T, Kim K. Nanocrystalline hydroxyapatite coatings from ultrasonated electrolyte: Preparation, characterization, and osteoblast responses. J Biomed Mater Res 2008;87A:1053–1060.

[26] Teng S, Lee E, Park C, et al. Bioactive nanocomposite coatings of collagen/hydroxyapatite on titanium substrates. J Mater Sci: Mater Med 2008;19:2453–2461.

[27] Ciobanu G, Carja G, Ciobanu O, Sandu I, Sandu A. SEM and EDX studies of bioactive hydroxyapatite coatings on titanium implants. Micron 2009;40:143–146.

[28] Shibli SMA, Mathai S. The role of calcium gluconate in electrochemical activation of titanium for biomimetic coating of calcium phosphate. J Biomed Mater Res 2008;87A:994–1002.

[29] Journeay WS, Suri SS, Moralez JG, Fenniri H, Singh B. Rosette nanotubes show low acute pulmonary toxicity in vivo. Int J Nanomed 2008;3:373–383.

[30] Lee KW, Wang S, Yaszemski MJ, Lu L. Physical properties and cellular responses to crosslinkable poly(propylene fumarate)/hydroxyapatite nanocomposites. Biomaterials 2008;29:2839–2848.

CHAPTER 4
ROSETTE NANOTUBES WITH DIFFERENT FUNCTIONAL GROUPS AS ORTHOPEDIC OR VASCULAR STENT COATING MATERIALS

A portion of this chapter has been published in:

1. E. Fine, **L. Zhang**, H. Fenniri, and T. J. Webster. Enhance Endothelial Cell Functions on Helical Rosette Nanotubes Coated Titanium for Improved Vascular Stent Applications. *Journal of Nanoscience and Nanotechnology,* in press (2009).

4.1 Introduction

It has been well-known that cells (such as osteoblasts) preferentially attach with various amino acid or peptide sequences (such as RGD) via cell-membrane integrin receptors as shown in Figure 1.4. Furthermore, other researchers reported that other mechanisms may be also involved in cell adhesion processes [1-5]. For example, osteoblast adhesion may be regulated via cell-membrane heparin sulphate proteoglycans and heparin-binding sites on proteins (i.e., fibronectin and collagen) as well [1-4]. Dee and colleagues demonstrated for the first time that lysine-arginine-serine-arginine (KRSR) peptides selectively enhanced osteoblast, but not endothelial cell or fibroblast adhesion via a heparin sulphate proteoglycan mediated mechanisms [5]. Since osteoblast adhesion is an important process at the bone-implant interface, the selectively controlled osteoblast adhesion holds great potentials for the long-term success of orthopedic implant.

Thus, a novel KRSR functionalized rosette nanotube was investigated in this chapter for selectively controlled orthopedic applications. Figure 4.1 reveals the building blocks of RNT-KRSR and the self-assembly process in water. The RNT-KRSR building blocks were composed of twin G^C bases with one KRSR side chain (Figure 4.1A) while previous RNT-K and RNT-RGD-K building blocks had single G^C base. The resulted nanotubes had a larger diameter than the single base RNT-K. For the single base G^C-RGDSK motif, only up to 10% RGD modified RNTs were assembled in the current study due to the effects of long peptide side chains. However, this twin base construct

guaranteed the formation of stable rosette nanotubes functionalized with 100% KRSR side chains. It was anticipated that the RNTs with rich KRSR peptides can selectively improve osteoblast adhesion and inhibit other cell functions (such as fibroblasts, the undesirable fibrous tissue contributed cells) for better orthopedic applications. In addition, not limited to KRSR peptides, K (Figure 4.1B) and RGD (Figure not shown) can be covalently bonded onto twin base G^C motifs.

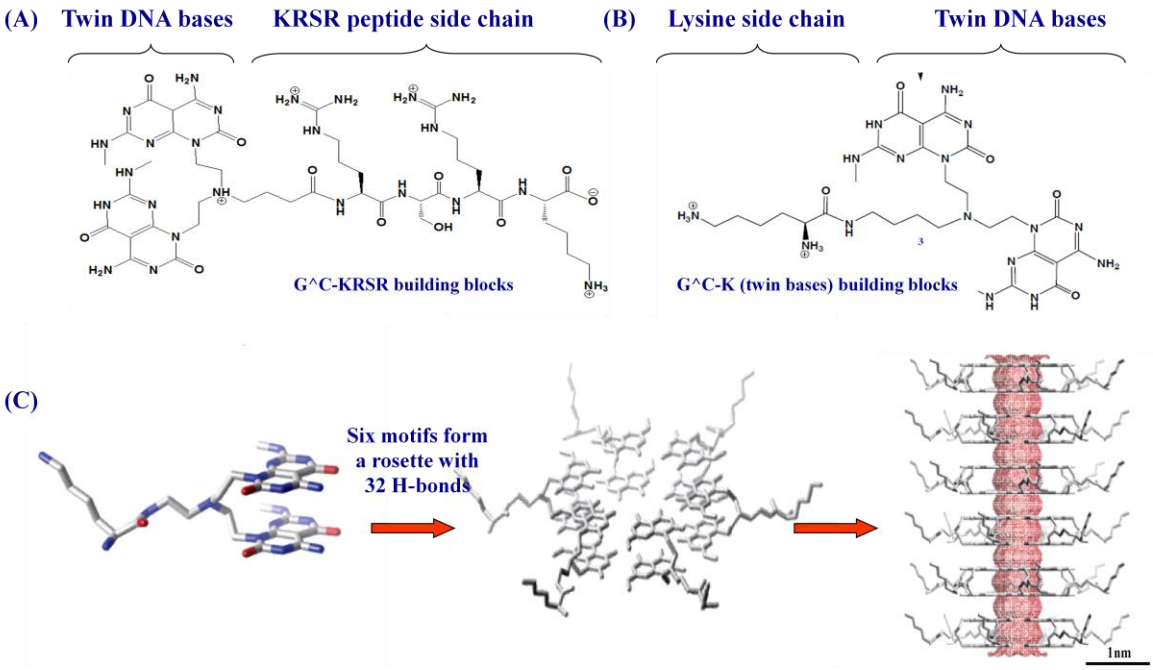

Figure 4.1 The new KRSR functionalized rosette nanotubes. (A) The twin base building blocks with KRSR side chains (G^C-KRSR, twin bases); (B) The twin base blocks with K side chains (G^C-K, twin bases); (C) The self-assembly process of twin bases into a larger diameter rosette nanotube (with K side chains). Figure 4.1C is redrawn from [6].

Moreover, due to the increasing prevalence of vascular diseases, there is an enormous market for vascular stents (commonly metallic scaffolds, such titanium) which are inserted into narrowing or clogged arteries in order to improve the normal blood flow and prevent myocardial infarction (Figure 4.2A). However, there still existed several

unresolved issues with current vascular stents. For example, bare metal stents often trigger an inflammatory response leading to scar tissue buildup on the stent, known as restenosis [7], which constricts the blood flow defeating the original purpose of the stent (Figure 4.2B). Drug-eluting stents combat this by releasing immune-suppressants, but these can also suppress the endothelial cell growth and leave parts of the metal exposed to the bloodstream, and eventually interactions between the two can form a clot in a process known as late thrombosis (Figure 4.2C) [8]. The underlying reasons of both of these issues are the contact between the stent and the proteins and cells of the bloodstream. Since nanomaterials have shown much promise to improve vascular cell (specifically, endothelial and smooth muscle cells) functions to inhibit thrombosis and severe inflammation [9-13], we investigated endothelialization on biologically-inspired RNT coatings on titanium without the use of drugs for improving vascular stent efficacy here.

4.2 Research Objectives

This chapter investigated the cytocompatibility properties of rosette nanotubes functionalized with KRSR, K and RGD as coatings on titanium for selectively improving orthopedic applications. For this purpose, different types of RNTs were characterized using transmission electron microscopy. Then, the osteoblast, fibroblast adhesion on the novel KRSR modified RNTs coated titanium were tested and compared to RNTs with K and RGD sequences coated titanium. In addition, long-term osteoblast responses (such as total protein synthesis, alkaline phosphatase activity and calcium deposition by

osteoblasts) on RNT-K hydrogels were investigated in this chapter.

Lastly, the endothelial cell adhesion and proliferation were determined on rosette RNT-K coated conventional vascular materials (specifically, titanium) for potential vascular stent applications.

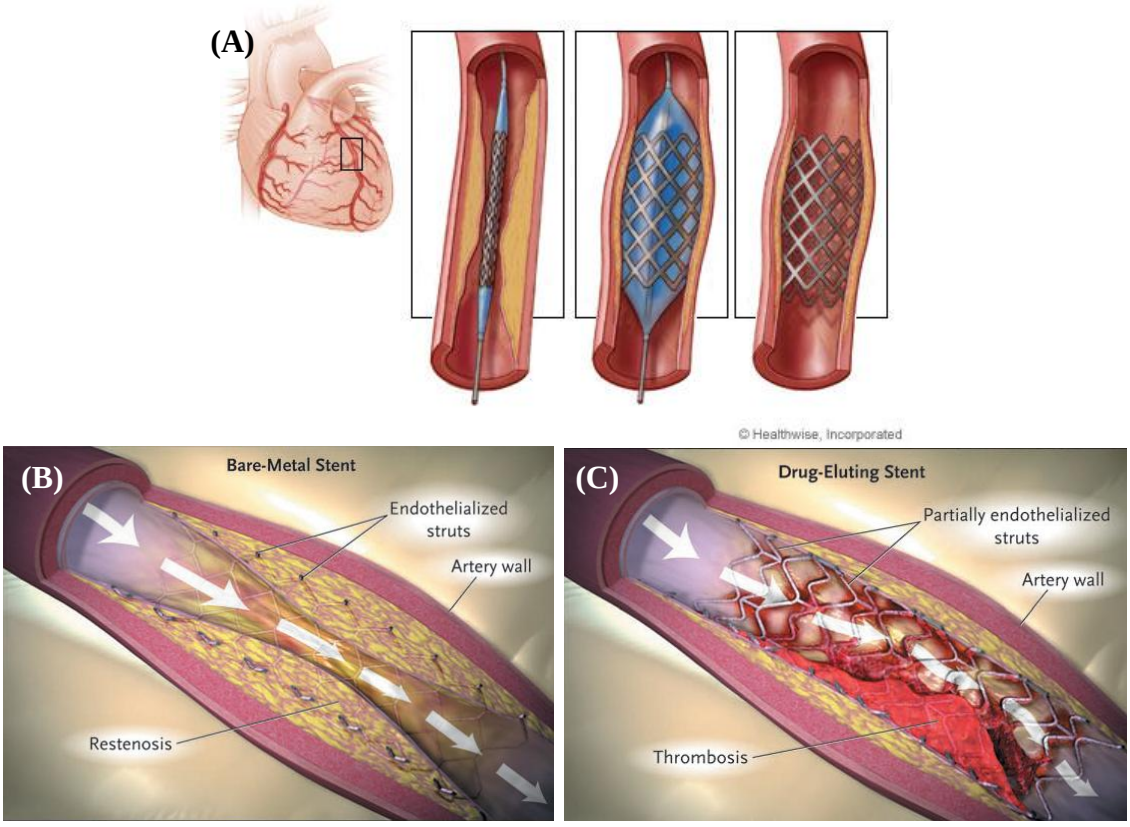

Figure 4.2 Coronary stenting. (A) Coronary stent implantation process. (B) Restenosis in a traditional bare-metal stent. (C) Late thrombosis in a drug-eluting stent. Arrows represent blood flow. Figure 4.2A is adapted from [14] and Figures 4.2B-4.2C are adapted from [15].

4.3 Materials and Methods

4.3.1 Sample Preparation and Characterization

Titanium squares (1x1x0.05 cm, Ti, Alfa Aesar titanium foil) and glass coverslips were cleaned as described in sections 3.3.2.1 and 2.3.1.2. Then, they were put into a drying oven overnight and autoclaved for sterilization before cell experiments. In the proliferation experiment, the titanium was first soaked in soap for 15 min, sonicated for 30 min and then rinsed prior to undergoing the above steps in order to thoroughly clean the substrate and remove any grease that might be deposited when the pieces were cut.

G^C-KRSR or G^C-K (twin bases, in HCl or in TFA) motifs were synthesized by Usha Hemraz in Department of Chemistry at University of Alberta. The G^C-K (twin bases) in HCl or in TFA are the same types of nanotube building blocks except being synthesized in different solvents, thus may have different counter ions. 1 mg/mL of RNT-KRSR and RNT-K (twin bases) stock solutions were prepared by dissolving 1mg of G^C-KRSR or G^C-K (twin bases, in HCl or in TFA) into 1 mL of ddH_2O. These stock solutions were diluted into 0.1 mg/mL and 0.01 mg/mL solutions. In addition, 0.01 mg/mL 1% and 5% RNT-RGD-K and 0.01 or 0.001 mg/mL of RNT-K were prepared as described in section 2.3.1.2. Furthermore, 1 mg/mL KRSR peptide solutions was also prepared by directly dissolving 1mg KRSR into 1mL of ddH_2O and was then diluted into 0.01 mg/mL as comparisons. All of the above sample solutions were filtered through a 0.22 μm syringe

filter. The morphology of various RNTs with KRSR, RGD and K (singe or twin bases) were characterized by TEM. The day before cell seeding, the cleaned titanium was coated by various 0.01 mg/mL or 0.001 mg/mL of RNT and 0.01 mg/mL KRSR peptide solutions for 45 min at room temperature, then removed and left to dry overnight.

In addition, 0.01 mg/mL and 0.001 mg/mL RNT-K embedded in and coated on hydrogels samples were achieved (as described in section 2.3.1.2) in order to test long-term osteoblast differentiation.

4.3.2 Short-Term Cell Testing

4.3.2.1 Osteoblast, Fibroblast and Endothelial Cell Culture

The same human fetal osteoblast cell line described in Chapters 2 and 3 was used and cultured here. Rat skin fibroblast cell line (FR, ATCC, CRL-1213) was cultured in Eagle's Minimum Essential Medium (EMEM, ATCC, 30-2003) supplemented with 10% fetal bovine serum (FBS, Hyclone, UT) under standard cell culture conditions (37℃, humidified, 5% CO_2/95% air). Rat aortic endothelial cell (RAEC, VEC Technologies) was cultured in MCDB-131 Complete medium (VEC Technologies) under standard cell culture conditions. The fibroblasts at population numbers 6-9 and the endothelial cells at pollution numbers 6-11 were used in the adhesion and proliferation study. The cell medium was replaced every other day.

4.3.2.2 Osteoblast, Fibroblast and Endothelial Adhesion Study

For the osteoblast, fibroblast and endothelial adhesion study, various RNT-KRSR, RNT-RGD-K, RNT-K, RNT-K (twin bases) and KRSR peptide coated titanium, uncoated titanium controls and glass references were tested. Cells were seeded onto the substrates at a density of 3500 cells/cm^2 and were incubated in the medium (specifically, DMEM supplemented with FBS and P/S for osteoblasts, EMEM supplemented with FBS for fibroblasts and MCDB-131 complete medium for endothelial cells) for 4 h. Then, the substrates were rinsed three times with PBS to remove non-adherent cells. The remaining cells were double fixed, stained with rhodamine-phalloidin (Molecular Probes) and DAPI (Invitrogen) as described in section 2.3.3.2. The cells were observed using a fluorescent microscope and five different areas of each sample were imaged. The cell density was then determined by counting cells using Image Pro Analyzer.

4.3.2.3 Endothelial Cell Proliferation Study

For the 5 day endothelial cell proliferation study, three sets of substrates including 0.01 mg/mL and 0.001 mg/mL RNT-K coated titanium as well as uncoated titanium were seeded at a cell density of 1000 cells/cm^2 and were placed in an incubator. The medium was changed every other day. After 1, 3 and 5 days, a set was taken out, stained and counted using the same procedure as in the adhesion study. Cellular experiments were run in triplicate and repeated three separate times for each samples.

4.3.3 Long-Term Osteoblast Function Study

Previous chapters and sections mainly focused on short-term osteoblast adhesion and proliferation, long-term osteoblast functions including total protein synthesis, alkaline phosphatase activity and calcium deposition were further investigated here. Osteoblasts were seeded at a density of 50,000 cells/cm^2 on: 1) 0.01 mg/mL and 2) 0.001 mg/mL RNT-K coated on hydrogels; 3) 0.01 mg/mL and 4) 0.001 mg/mL RNT-K embedded in hydrogels; 5) uncoated hydrogels; and 6) glass references. Then they were cultured in DMEM supplemented with 10% FBS, 1% P/S, 50 μg/mL L-ascorbate acid (Sigma), and 10 mM β-glycerophosphate (Sigma) for 7, 14, and 21 days under the standard cell culture conditions. Cell culture medium was changed every other day. At each prescribed time point, osteoblasts were lysed using distilled water and three freeze-thaw cycles as mentioned elsewhere [16,17], which removed intracellular and membrane-bound proteins. All of resulted solutions were stored at 4 ℃ refrigerator before testing.

4.3.3.1 Total Protein Synthesis

Total protein content in the cell lysates was measured using a commercial BCA^{TM} Protein Assay Reagent kit (Pierce Biotechnology) and following manufacturer's instructions. For this purpose, 150 μL of aliquot supernatants of the protein-containing cell lysates were mixed with 150 μL of working agent solutions (including 1:24:25 of cupric sulfate : bicinchnoninic acid : a reagent with sodium bicarbonate, sodium carbonate and sodium tartrate) and then were incubated at 37 ℃ for 2 h. Light absorbance was measured at 562 nm on a spectrophotometer. According to a standard curve of known concentrations of

albumin versus absorbance run in parallel with experimental samples, the total protein synthesized by osteoblasts cultured on the substrates of interest to this study was calculated.

4.3.3.2 Alkaline Phosphatase Activity

The alkaline phosphatase activity in the cell lysates prepared above was evaluated by a commercially available Alkaline/Acid Phosphatase Assay kit (Upstate, Cat#17-128). For this purpose, 20 µL of the distilled water supernatants of cell lysates were mixed with 5 µL $NiCl_2$, 5 µL bovine serum albumin (BSA) and 5 µL phosphopeptide stock solution and 45 µL pNPP ser/thr assay buffer in one well of a 96-well microplate. Then, 25 µL aliquots of above mixtures (in triplicate) were transferred into a new plate and were incubated for 15 min at 37 ℃. 100 µL of Malachite Green solution were added to detect alkaline phosphatase activity. The absorbance of the prepared samples was read on a spectrophotometer at an absorbance wavelength of 650 nm (SpectraMax 340PC, Molecular Devices) and analyzed with SoftMax$^{@}$ Pro 5 software. Alkaline phosphatase synthesized by osteoblasts cultured on the substrates of interest to this study was calculated according a standard curve of known concentrations of phosphate versus absorbance run in parallel with the experimental samples. The final alkaline phosphatase activity was normalized by the substrate area and expressed as pmoles of converted pNPP per minute per square centimeter.

4.3.3.3 Calcium Deposition

Calcium deposition as one of the most important indicators of osteoblast differentiation was measured using a calcium reagent kit (Pointe Scientific Inc.). Briefly, after osteoblasts were lysed and removed, the extracellular matrix of all substrates was immersed in a 0.6 N HCl solution at 37℃ for 24h. After the prescribed time period, the amount of dissolved calcium present in the acidic supernatant was measured by reacting with the o-cresolphthalein complexone to form a purple-color solution. The light absorbance of these samples was measured at 570 nm by a spectrophotometer. Total calcium deposition was calculated from standard curves of known calcium concentrations versus absorbance run in parallel with the experimental samples. Calcium deposition values were normalized by the substrate area and expressed as mg/cm^2.

4.3.4 Statistics

Data were represented by the mean value with the standard error of the mean (SEM) and were analyzed with a student's t-test to make pair-wise comparisons. Statistical significance was considered at $p<0.1$.

4.4 Results and Discussion

4.4.1 Morphology of RNTs with Different Functional Groups

TEM images demonstrated that both the single and twin bases of DNA constructs with different amino acids and peptides (such as KRSR, K and RGD) formed rich rosette nanotube in water (Figure 4.3). Specifically, the RNT-KRSR formed a dense nanotube network in water (Figures 4.3A and 4.3B). Furthermore, TEM images revealed that the RNT-KRSR had a larger diameter (~ 4.5 nm) than other RNT-K (single or twin bases). In addition, 0.1 mg/mL RNT-K (twin bases, in HCl or TFA, Figures 4.3C and 4.3D) also formed many long nanotubes with ~ 4 nm diameters and several hundred nm lengths while the normal singe base RNT-K had ~ 3.5 nm diameters (Figure 4.3E). As controls, KRSR peptide did not show nanotube morphologies under TEM (Figure 4.3G).

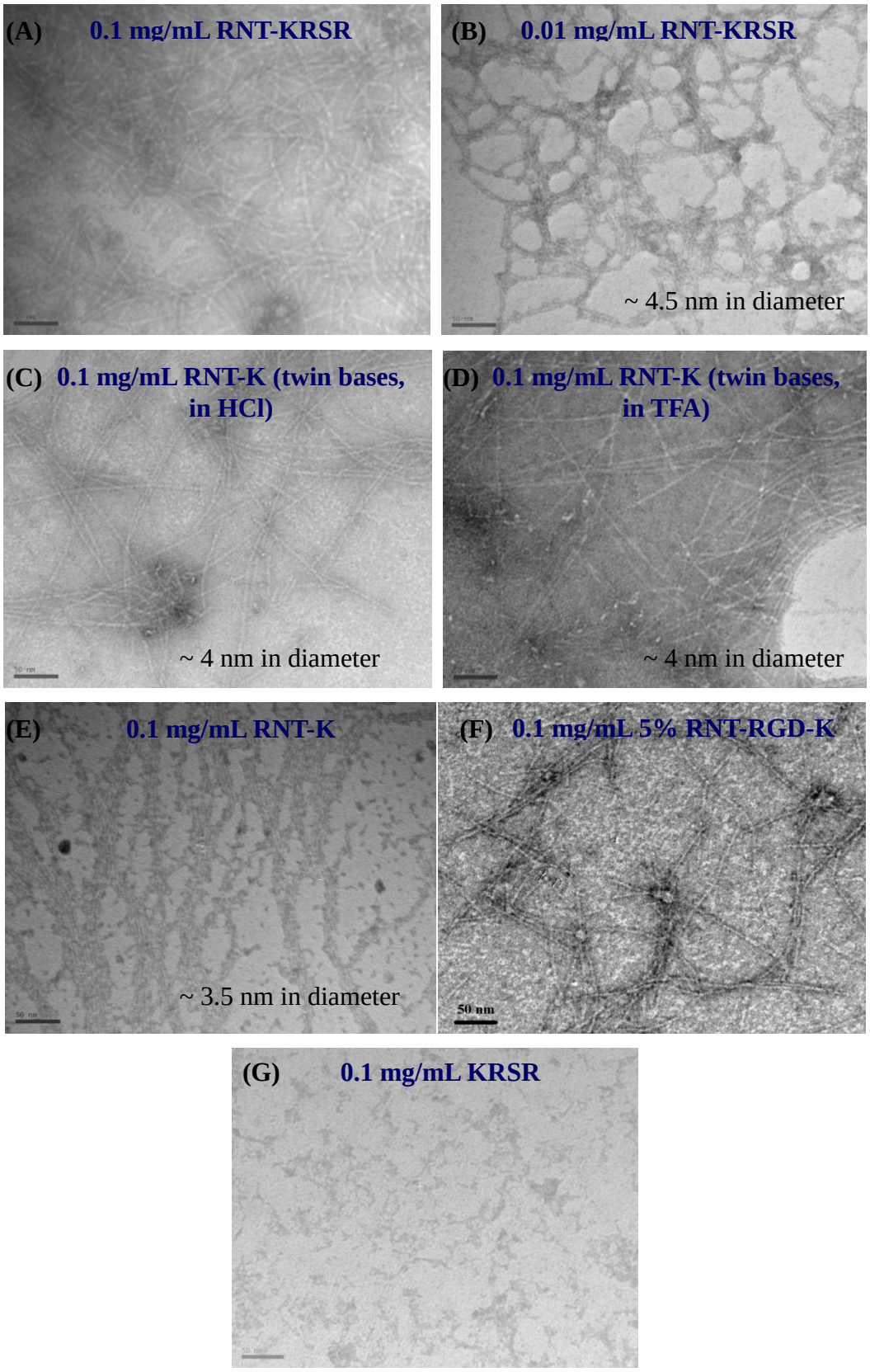

Figure 4.3 TEM images of various RNTs and KRSR peptides.

4.4.2 Cell Responses Towards RNT Coatings

4.4.2.1 Osteoblast Adhesion

Several other studies showed the promise of the KRSR peptides for improved orthopedic implants [18,19]. For example, Balasundaram et al. once immobilized KRSR peptides on nanophase and conventional titanium surfaces for improved osteoblast adhesion [18]. In their study, they demonstrated that KRSR functionalized titanium (both nanophase and conventional) increased osteoblast adhesion compared to respective nonfunctionalized substrates, which indicated that altering surface chemistry of implant materials using KRSR peptides was promising for future orthopedic applications. Furthermore, they also observed a high density of osteoblasts on nanophase titanium without KRSR when compared to conventional titanium with KRSR, which possibly suggested the importance of nanometric feature of biomaterials on improving osteoblast adhesion. In this chapter, nanostructured RNTs functionalized with cell-adhesive KRSR peptides were coated on titanium in order to create a biomimetic environment for cell adhesion.

Results demonstrated that all of RNTs and KRSR peptide coated titanium significantly enhanced osteoblast adhesion compared to uncoated titanium (Figure 4.4). For example, 0.01 mg/mL RNT-KRSR and 5% RNT-RGD-K coated titanium improved osteoblast adhesion by 121.7% and 124.4%, respectively, compared to uncoated titanium. In fact, the KRSR and RGD peptides modified RNTs (specifically, RNT-KRSR or 5% RNT-RGD-K) induced the highest osteoblast densities on titanium. The results confirmed

again the surface chemistry role of RNTs towards improving cell functions as discussed in section 2.5.3.2. Furthermore, all of the RNTs coated on titanium also attached more cells than KRSR peptides coated titanium, which was consistent to previous results of favorable cell responses on RNTs over poly L-lysine and collagen (see chapter 2). Especially, osteoblast adhesion on RNT-KRSR coated titanium was 84.4% more than on KRSR coated titanium, which provided evidence that nano-biomimeitc features of RNTs besides the favorable surface chemistry contributed to improving cell adhesion as well.

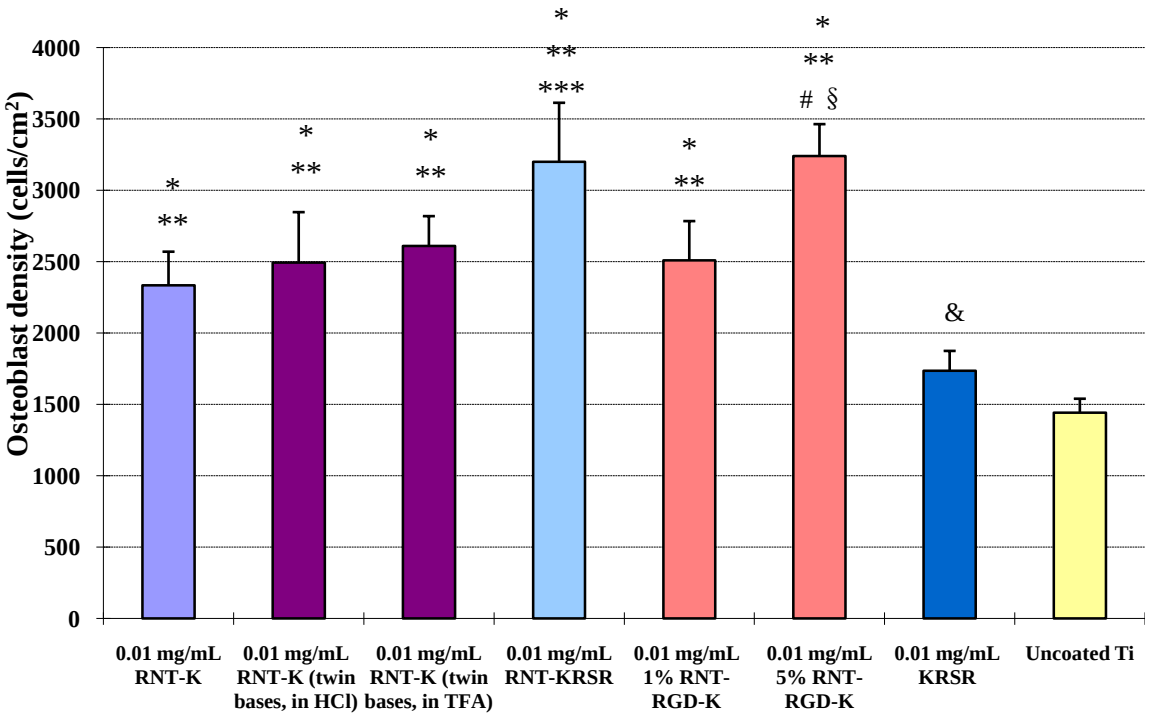

Figure 4.4 Osteoblast adhesion on RNTs coated on titanium. Data are mean values ±SEM, N=3. *p<0.01 and &p<0.1 compared to uncoated titanium; **p<0.05 compared to 0.01 mg/mL KRSR coated on titanium; ***p<0.1 compared to 0.01 mg/mL RNT-K, 1% RNT-RGD-K, RNT-K (twin bases, in HCl) coated titanium; #p<0.05 compared to 0.01 mg/mL RNT-K coated titanium; and §p<0.1 compared to 1% RNT-RGD-K, RNT-K (twin bases, in HCl or in TFA) coated titanium.

Moreover, Figure 4.5 showed nuclei stained cell density and the rhodamine stained osteoblast spreading morphology on the substrates of interest to the present study. Generally, compared to KRSR coated and uncoated titanium, all of RNT coated titanium

increased cell number. Additionally, osteoblasts were more extended on the nanostructured RNT (such as RNT-K with singe or twin bases, RNT-RGD-K and RNT-KRSR) coated titanium than on uncoated titanium. Very long osteoblast filopodia protrusions were observed at RNTs coated titanium as indicated by arrows (Figures 4.5A', 4.5F').

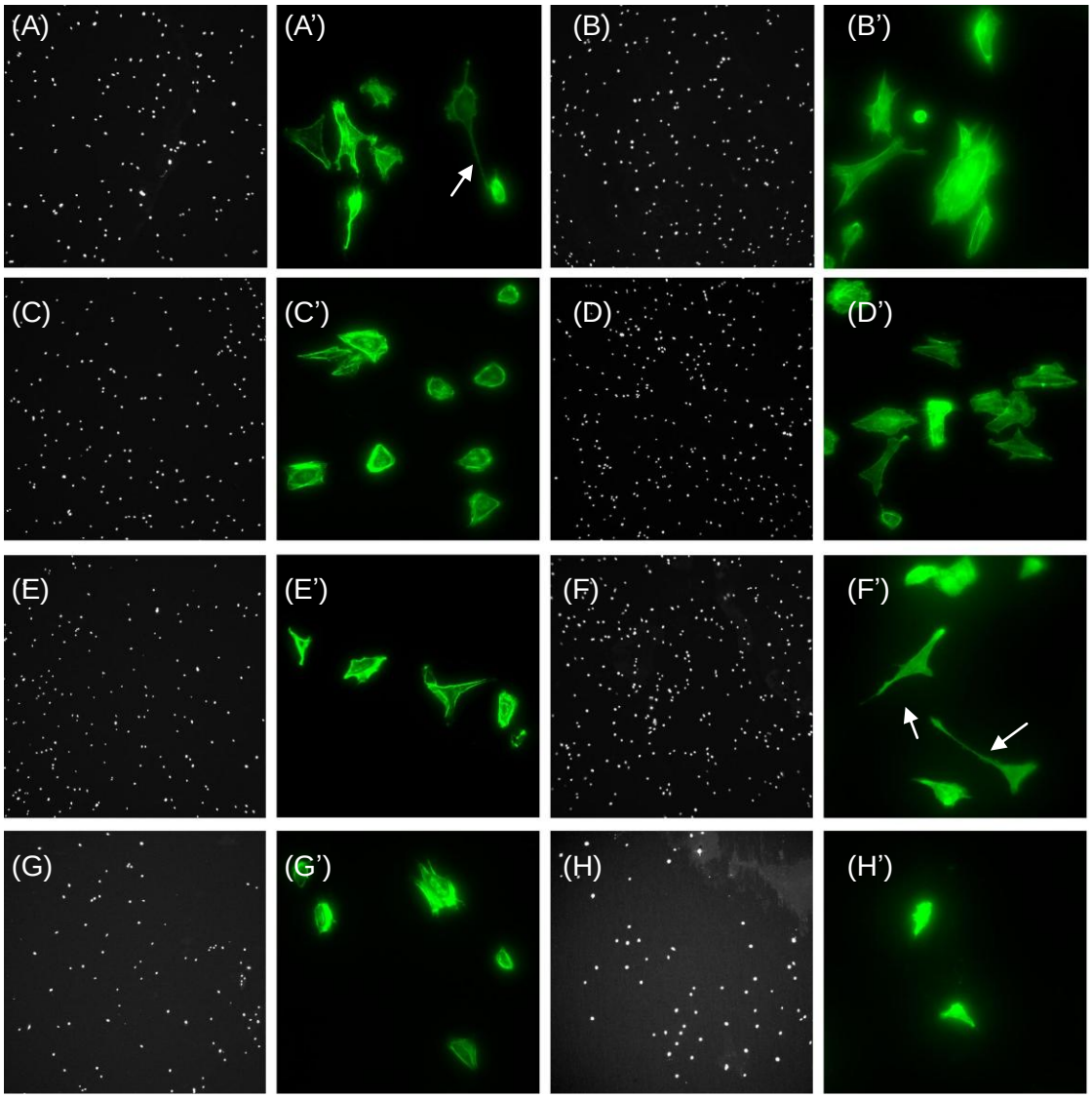

Figure 4.5 Fluorescent microscopy images of osteoblast adhesion on RNT coated titanium at low (original magnification 50×, DAPI stained nuclei) and high magnifications (400×, rhodamine stained F-actin). 0.01mg/mL of (A) and (A') RNT-K; (B) and (B') RNT-K (twin bases, in HCl); (C) and (C') RNT-K (twin bases, in TFA); (D) and (D') RNT-KRSR; (E) and (E') 1% RNT-RGD-K; (F) and (F') 5% RNT-RGD-K; and (G) and (G') KRSR coated titanium. (H) and (H') uncoated titanium as controls.

4.4.2.2 Fibroblast Adhesion

Fibroblasts are one of the contributor cells for forming a fibrous capsule, which prevents sufficient osseointegration and frequently leads to orthopedic implant failure. Consequently, minimizing the functions of fibroblasts (such as their adhesion) is necessary at the surface of a newly implanted orthopedic device [20]. For this purpose, this chapter investigated fibroblast responses towards the RNTs functionalized with KRSR and K.

The result provided evidence that RNTs functionalized with KRSR or K regardless of singe base or twin bases did not improve fibroblast adhesion (Figure 4.6). Specifically, the KRSR peptides inhibited the fibroblast adhesion. Due to the previous reports [1-4], KRSR peptides may only improve osteoblast not other cell adhesion on substrates via cell-membrane heparin sulphate proteoglycan mechanism. The selectively controlled cell adhesion on RNT coated titanium (i.e., only attracting favorable osteoblast adhesion and repelling undesirable fibroblast adhesion) may have a positive effect on the orthopedic success in a long run. Finally, Figure 4.7 showed the fibroblast spreading morphologies on different RNT-K and RNT-KRSR coated titanium and controls. Many tiny filopodia extensions of rounded fibroblasts were visible on all substrates.

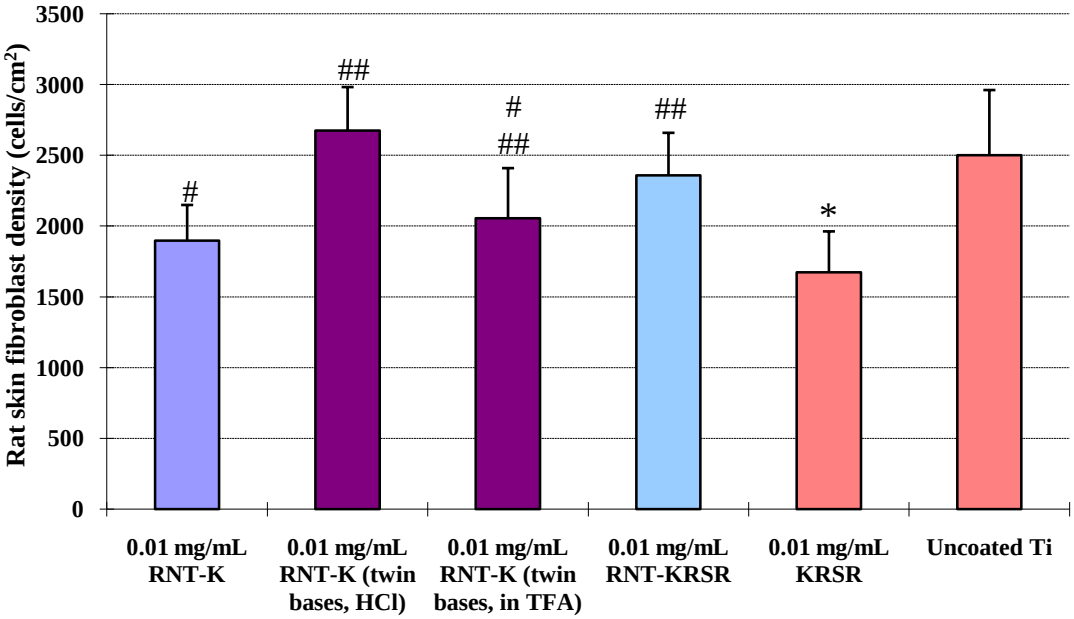

Figure 4.6 Fibroblast adhesion on RNTs coated on titanium. Data are mean values ±SEM, N=3. *p<0.05 compared to uncoated titanium; #p<0.05 compared to 0.01 mg/mL RNT-K (twin bases, in HCl) coated on titanium; and ##p<0.05 compared to 0.01 mg/mL KRSR coated on titanium.

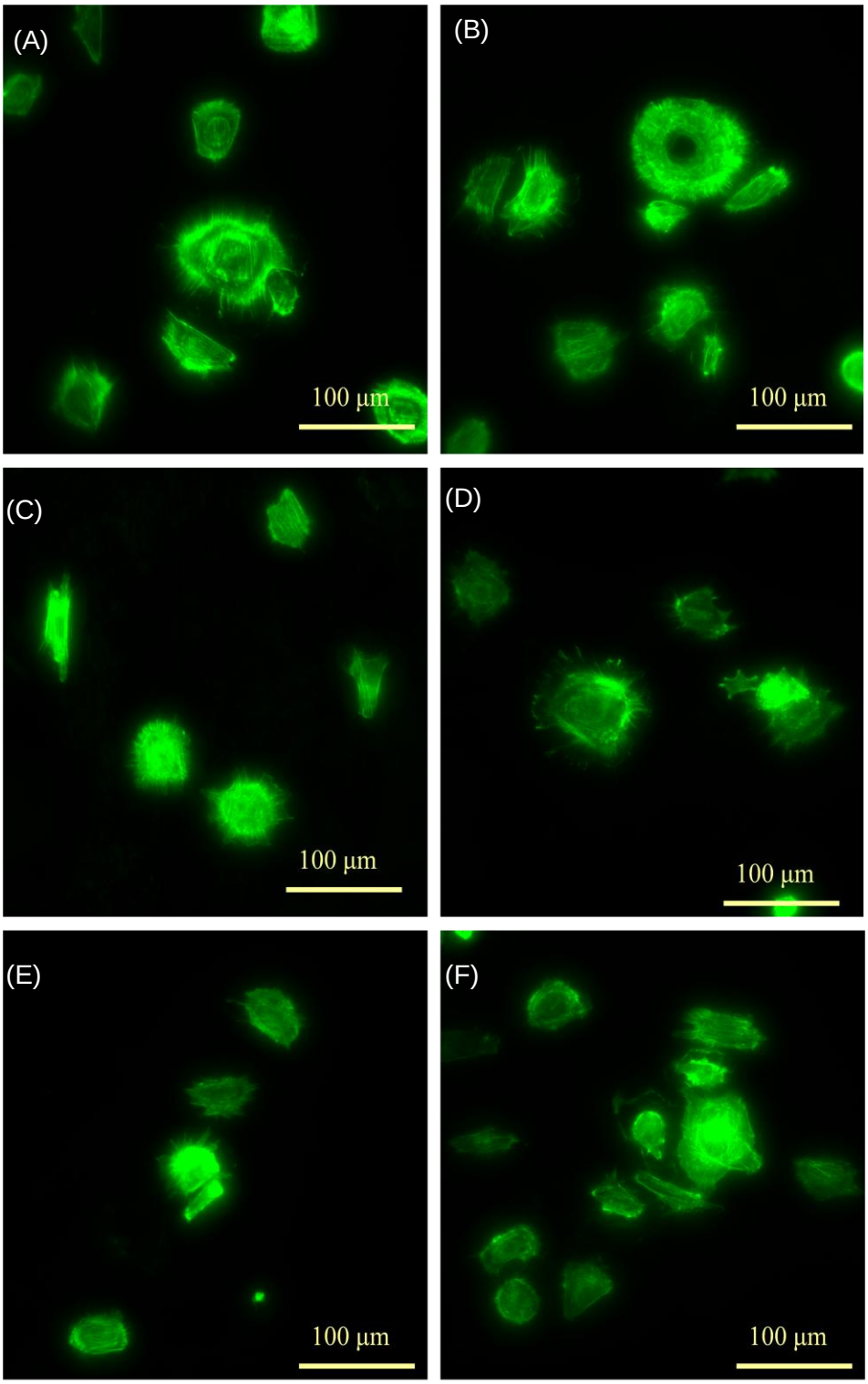

Figure 4.7 Fluorescent microscopy images of fibroblast spreading morphologies. (A) RNT-K (twin bases, in HCl) coated titanium; (B) RNT-K (twin bases, in TFA) coated titanium; (C) RNT-K coated titanium; (D) RNT-KRSR coated titanium; (E) KRSR coated titanium and (F) uncoated titanium.

4.4.3 Osteoblast Long-Term Functions on RNT-K Hydrogels

Figure 4.8 showed the total protein content synthesized by osteoblasts on all substrates after 7, 14 and 21 days. With longer time of osteoblast culture, greater total protein synthesis on all samples was observed after 21 days than after 7 days. There was no statistical significance among the RNT-K hydrogels and controls at each time point. However, there still existed an increasing trend of total protein synthesis on 0.01 mg/mL RNT-K coated on hydrogels and 0.001 mg/mL RNT-K embedded in hydrogels compared to hydrogel controls after 21 days of culture.

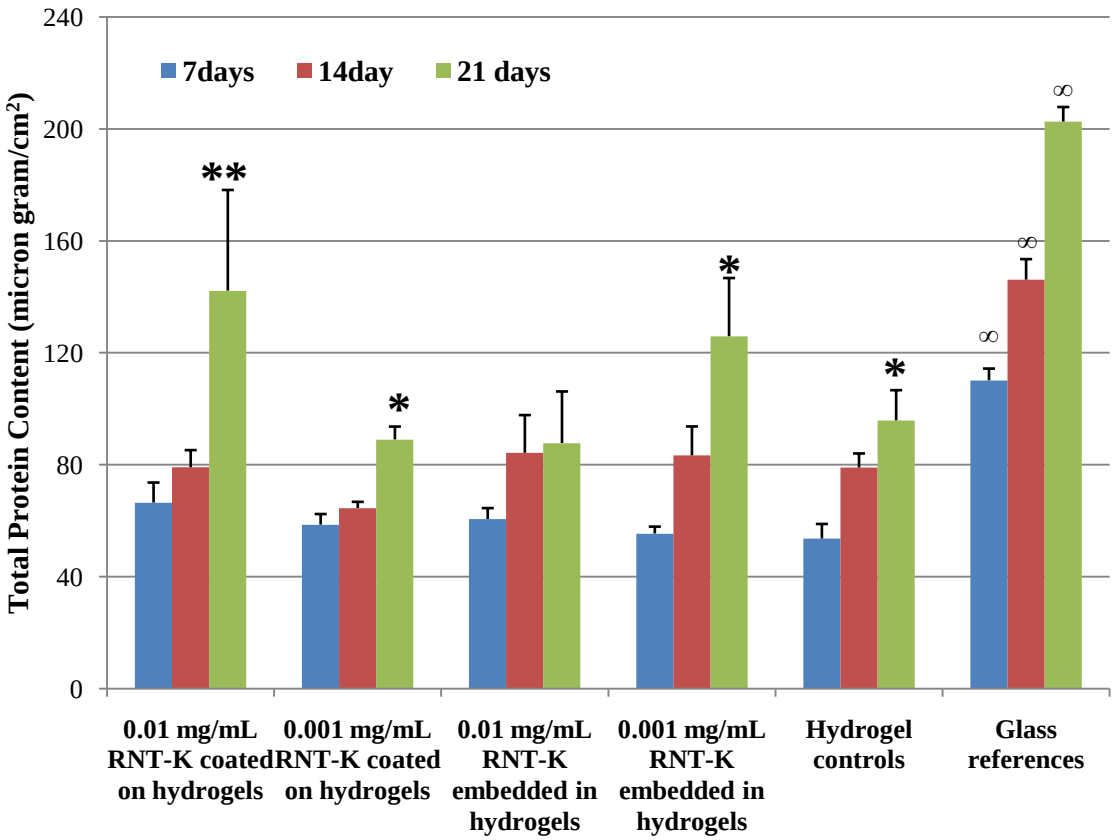

Figure 4.8 Total protein content in osteoblasts cultured on RNT-K hydrogels, hydrogel controls and glass references. Data are mean ± SEM, n=3; *$p<0.05$ and **$p<0.1$ compared to respective substrates at 7 days. ∞$p<0.05$ compared to all hydrogel substrates at respective 7, 14 and 21 days.

As an enzyme occurring in high concentrations during bone growth [21], alkaline phosphatase signifies the osteoblast differentiation [22] and often correlates to the degree of mineralization. The increasing amounts of alkaline phosphatase synthesized by osteoblasts were detected on all the substrates after 7, 14, and 21 days of culture (Figure 4.9). Specifically, the 0.01 mg/mL and 0.001 mg/mL RNT-K embedded in hydrogels promoted significantly greater ($p<0.1$) alkaline phosphatase activity than hydrogel controls after 7 days. The early alkaline phosphatase activity can translate into more rapid calcium deposition by osteoblasts [17] which will be shown next. In addition, there was no statistical difference between other RNT-K coated hydrogels and uncoated hydrogels after 7 days of culture. After 14 days of culture, only 0.001 mg/mL RNT-K coated on hydrogel had greater amount of intracellular alkaline phosphatase activity than 0.001 mg/mL RNT-K embedded in hydrogel ($p<0.05$). Importantly, after 21 days of culture, the amount of alkaline phosphatase was the highest on 0.01 mg/mL RNT-K embedded in hydrogels. Osteoblast on the higher concentration (0.01 mg/mL) of RNT-K embedded in hydrogels had the greater ($p<0.05$) alkaline phosphatase activity than on 0.001 mg/mL RNT-K embedded in hydrogels after 21 days.

Most importantly, the calcium deposition into extracellular matrix was a crucial step during new bone growth. The results of the present study provided evidence that there were detectable amounts of calcium deposited by osteoblasts on all RNT-K hydrogels (Figure 4.10). The calcium depositions on all the substrates after 21 days were greater than after 7 and 14 days. Importantly, there were significantly greater calcium depositions on the 0.01 mg/mL and 0.001 mg/mL RNT-K embedded in hydrogels as well as 0.001

mg/mL RNT-K coated on hydrogels than hydrogel controls after 7 days of culture. In addition, there was no statistical difference between any of the RNT-K hydrogel and control substrates after 21 days of culture. All RNT hydrogels and control substrates had a larger amount of deposited calcium and alkaline phosphatase activity ($p<0.05$) than did the glass references at all time periods.

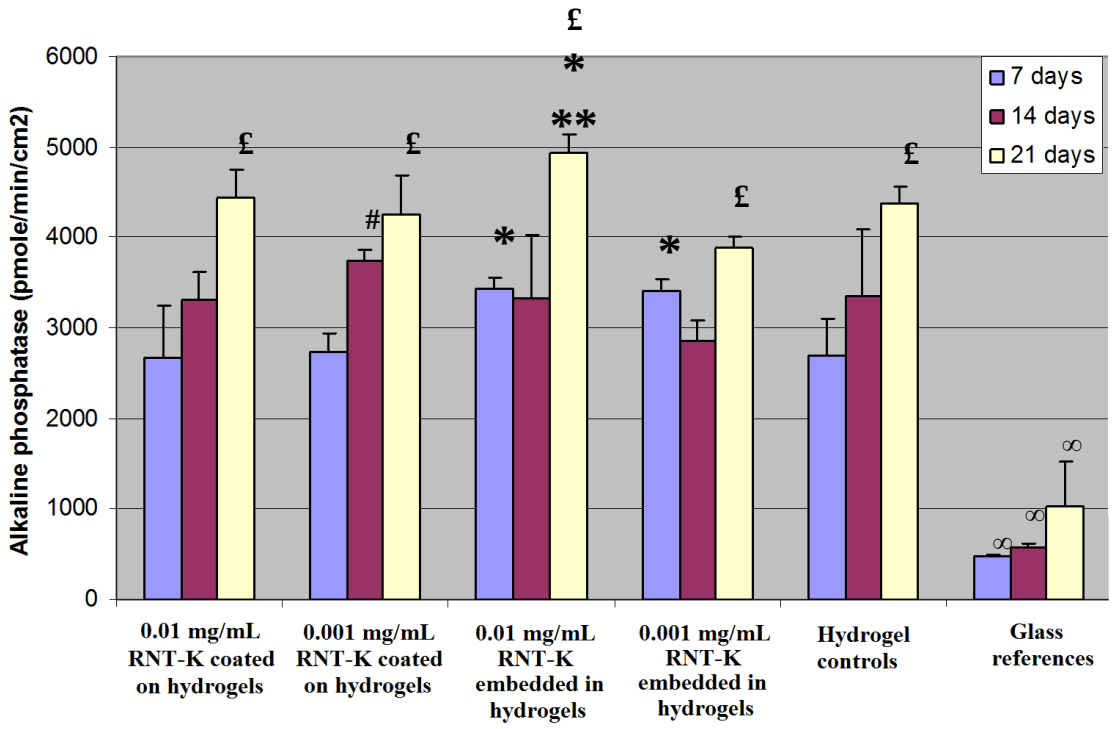

Figure 4.9 Enhanced alkaline phosphatase activity on RNT-K in hydrogels. Data are mean ± SEM, n=3; *p<0.1 compared to respective hydrogel controls at 7 and 21 days. #p<0.05 compared to 0.001 mg/mL RNT-K embedded in hydrogels at 14 days. **p<0.05 compared to 0.001 mg/mL RNT-K embedded in hydrogels at 21 days. £p<0.1 compared to respective substrates at 7 days. ∞p<0.05 compared to all hydrogel substrates at respective 7, 14 and 21 days.

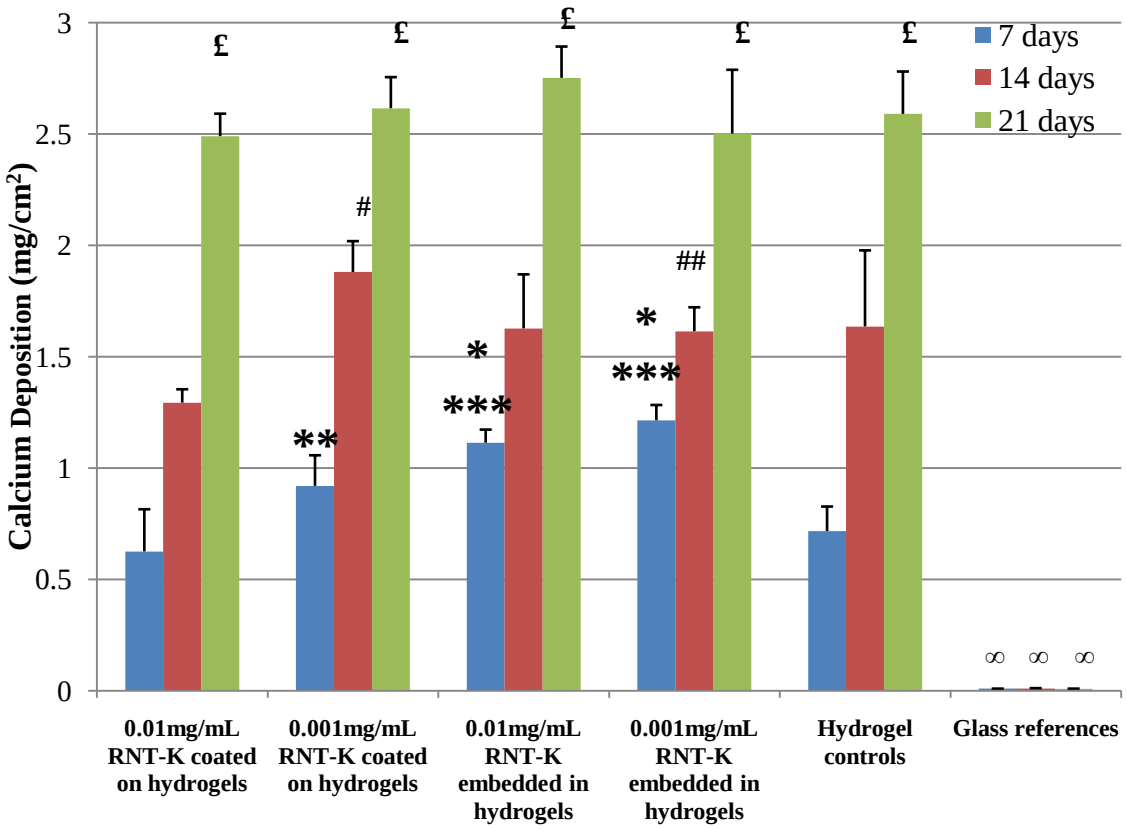

Figure 4.10 Increased early calcium deposition on RNT-K in hydrogels. Data are mean ± SEM, n=3; *p<0.05 and **p<0.1 compared to hydrogel controls at 7 days. ***p<0.1 compared to 0.01 mg/mL RNT-K coated on hydrogel at 7 days. #p<0.05 and ##p<0.1 compared to 0.01 mg/mL RNT-K coated on hydrogel at 14 days. £p<0.05 compared to respective substrates at 7 days. ∞p<0.05 compared to all hydrogel substrates at respective 7, 14 and 21 days.

Previous chapters demonstrated that various RNT (such as RNT-K and RNT-RGD-K) hydrogels greatly enhanced short-term osteoblast adhesion and proliferation as bone tissue engineering scaffolds [23-25]. The results of this osteoblast differentiation study demonstrated for the first time that the different concentrations of RNT-K coated on or embedded in hydrogels had exceptional cytocompatibility properties for long-term osteoblast functions. Although the total protein synthesis by osteoblasts did not increase significantly by the RNT-K, the alkaline phosphatase activity and the important calcium deposition were greatly promoted on RNT-K hydrogels compared to hydrogels controls

especially after 7 days of culture. In addition, the alkaline phosphatase activity on RNT hydrogels was increased with the increase of the RNT-K concentrations after 21 days, which was consistent to the previous osteoblast adhesion result in Figure 2.12. Apparently, the nanostructured RNTs can provide a biomimetic environment for the long-term bone growth.

Lastly, although alkaline phosphatase activity and calcium deposition on all RNT-K hydrogels were not significantly enhanced compared to hydrogel controls after 21 days, the more and quicker calcium deposition and alkaline phosphatase activity on RNT-K in hydrogels after 7 days may play a crucial role for further successfully regenerating strong bone at defect sites. Interestingly, the 0.01 mg/mL RNT-K coated on hydrogels which had the more osteoblast adhesion in previous chapters did not show the greater alkaline phosphatase activity and calcium deposition than other substrates at each time point. One of the possible explanations might be due to a portion of RNTs on the hydrogel surface washed out under a long time interaction with medium. Consequently, a better coating method in addition to the current physical adsorption method may be necessary to strongly coat RNTs on hydrogel or titanium. In addition, it was possible that the very strong osteoblast adhesion on 0.01 mg/mL RNT-K coated hydrogels in the short-term may have reverse effects on osteoblast migration and differentiation in a long term. Of course, this needs further exploration in details.

4.4.4 Endothelial Cell Functions on RNT Vascular Stent Coatings

4.4.4.1 Endothelial Cell Adhesion

The 4 h endothelial cell adhesion study provided evidence for the first time that cells adhered at a significantly higher ($p<0.05$) density to the titanium coated with 0.01 mg/mL of RNTs with K or RGD side chain than the uncoated titanium (Figure 4.11). Specifically, RNT-K (twin bases, in HCl) coated titanium attached the greatest endothelial cell over all other substrates. Furthermore, more cells were attached on the RNT-K coated titanium than on RNT-KRSR coated on titanium. The RNT-KRSR and KRSR peptide coated titanium did not enhance endothelial cell adhesion here, which confirmed the KRSR selectively controlled cell adhesion on substrates as described previously [5]. Endothelial cell spreading morphologies were shown in Figure 4.12.

Due to the above favorable endothelial cell adhesion on RNT-K coated titanium, different concentrations of RNT-K (specifically, 0.01 mg/mL and 0.001 mg/mL) coated titanium were further studied for potential vascular stent coatings. The results showed that both the concentrations of RNT-K significantly increased endothelial cell density over uncoated titanium (*$p<0.05$ and **$p<0.1$ in Figure 4.13). One hypothesis as to the cause of the increased endothelial cell adhesion was that the nanostructured RNTs had biomimetic features which were favorable for endothelial adhesion. In addition, other studies reported that poly L-lysine coated vascular stents can significantly improve endothelial

cell adhesion compared to uncoated controls perhaps due to the electric interaction between poly L-lysine and endothelial cell membrane [26]. Therefore, considering the rich K side chains and their well-controlled spatial distributions on RNTs, RNTs may alter the surface chemistry and surface roughness of titanium to allow the increased cell attachment and spreading as shown in Figures 4.11, 4.12 and 4.13.

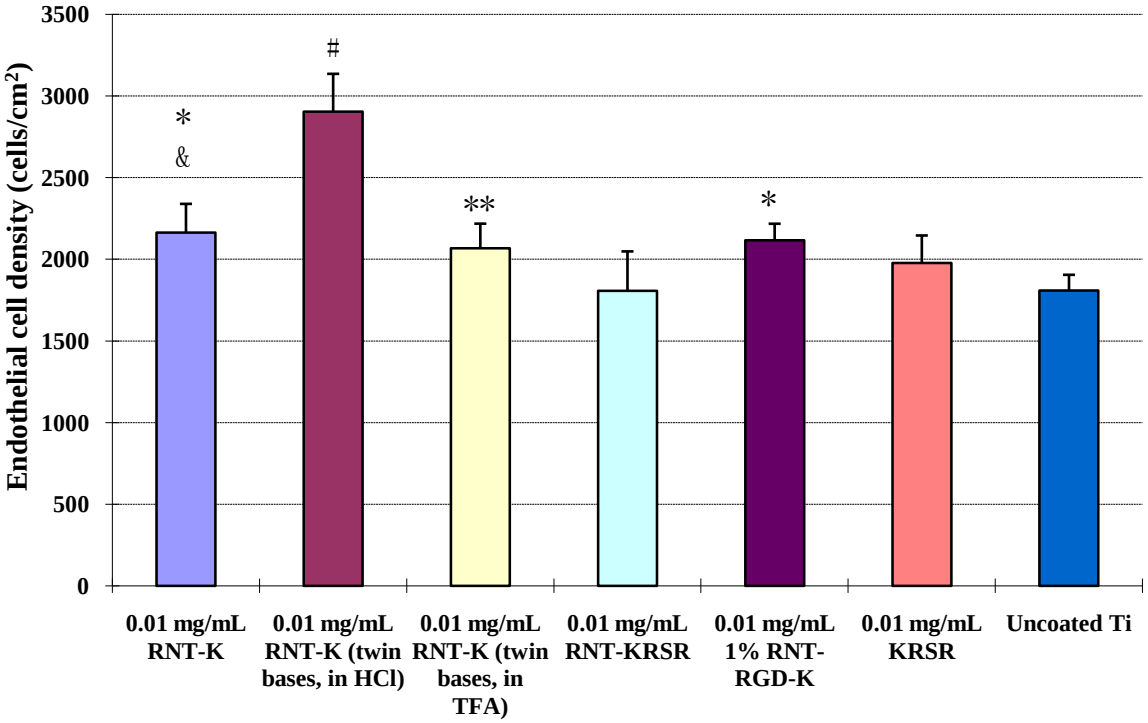

Figure 4.11 Endothelial cell adhesion on RNTs coated on titanium. Data are mean values ±SEM, N=3. *p<0.05 and **p<0.1 compared to uncoated titanium. #p<0.05 compared to all other substrates. &p<0.1 compared to 0.01 mg/mL RNT-KRSR coated on titanium.

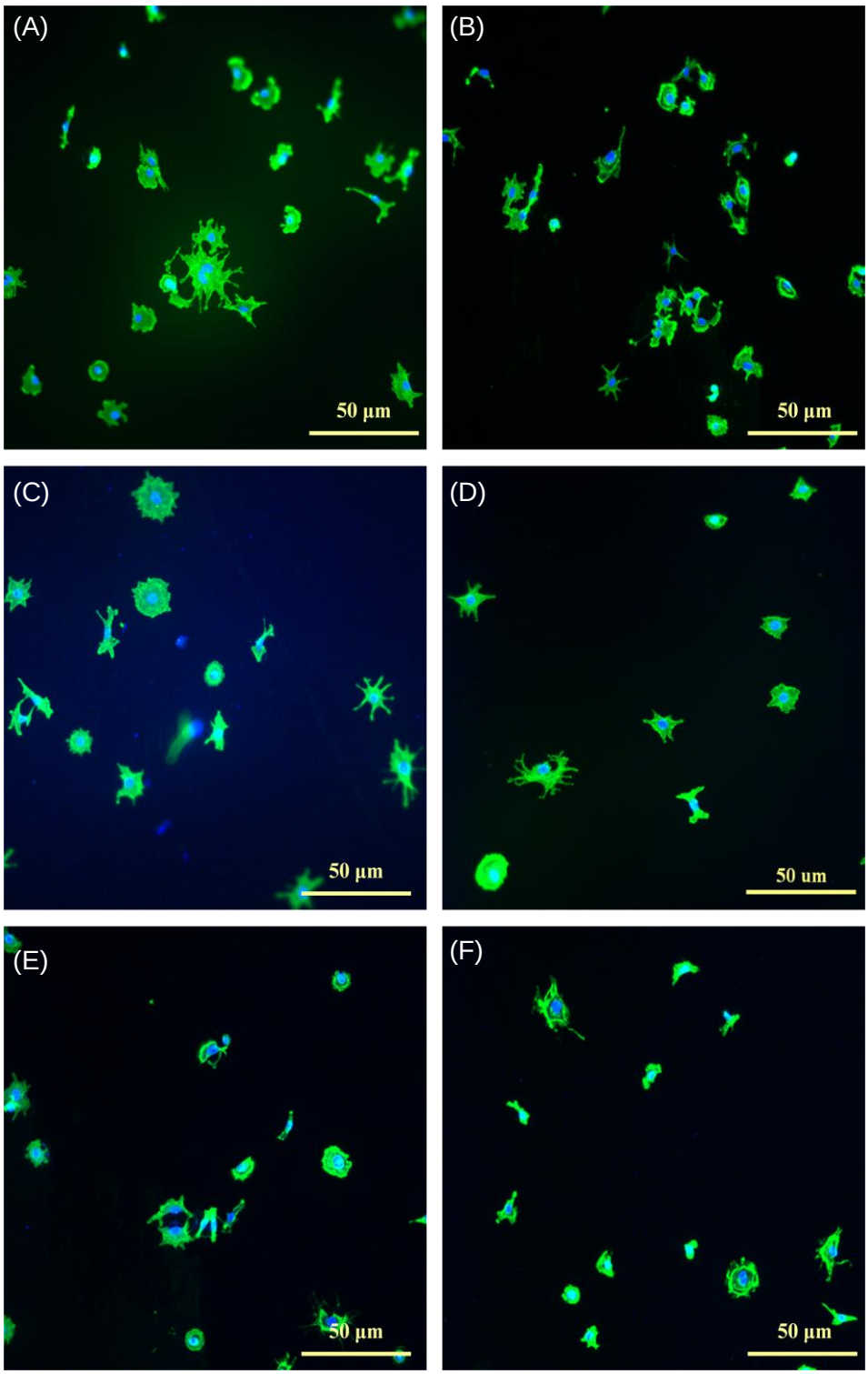

Figure 4.12 Fluorescent microscopy images of endothelial cell spreading morphologies on various coatings after 4 h. (A) RNT-K coated titanium; (B) RNT-K (twin bases, in HCl) coated titanium; (C) 1% RNT-RGD-K coated titanium; (D) RNT-KRSR coated titanium; (E) KRSR coated titanium; and (F) uncoated titanium. F-actins were stained by rhodamine (green color) and cell nuclei were stained by DAPI (blue color).

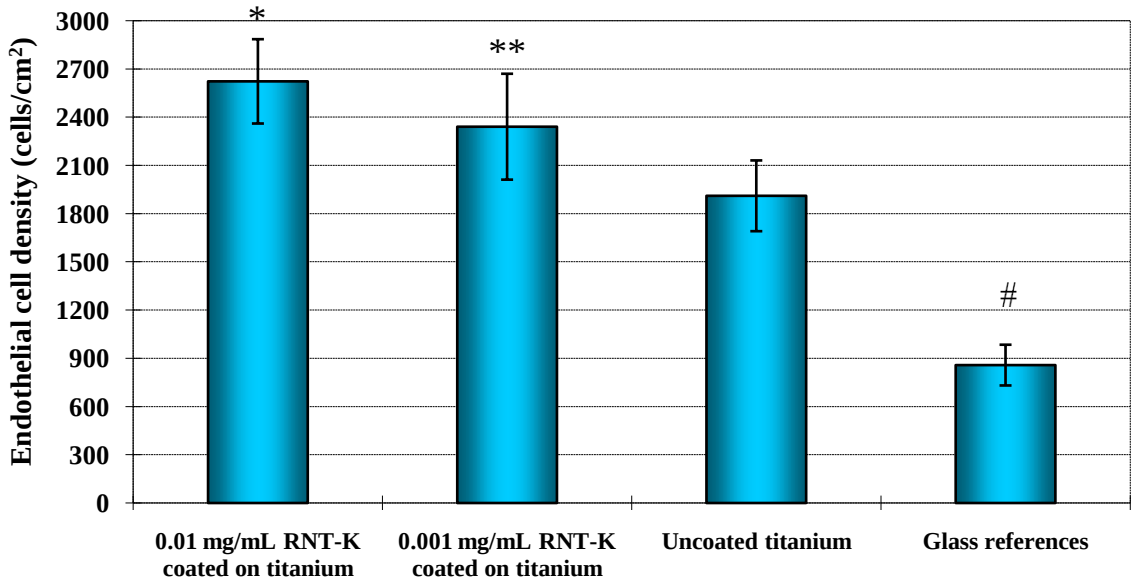

Figure 4.13 Enhanced endothelial cells adhesion of 0.01 and 0.001 mg/ml RNT-K coated on titanium after 4 h. Data are mean values ±SEM; N=3. *p<0.05, **p<0.1 compared to uncoated titanium and #p<0.005 compared to all other substrates.

4.4.4.2 Endothelial Cell Proliferation

Endothelial cells greatly proliferated on all substrates after 5 days. Importantly, the 5-day proliferation study demonstrated that RNT-K coated titanium greatly improved endothelial cell functions compared to the uncoated titanium (Figure 4.14). For example, the 0.01 mg/mL and 0.001 mg/mL RNT-K coated titanium showed 52% ($p<0.01$) and 21% ($p<0.05$) increases in cell densities respectively over uncoated titanium after 3 days of culture. In addition, the cell densities were significantly higher on 0.01 mg/mL RNT-K coated titanium than 0.001 mg/mL RNT-K coated titanium on day 3. This could be because the denser nanometric network on the titanium surfaces created by the higher concentrations of RNTs, with more lysine side chains displayed, induced more endothelial cell attachment.

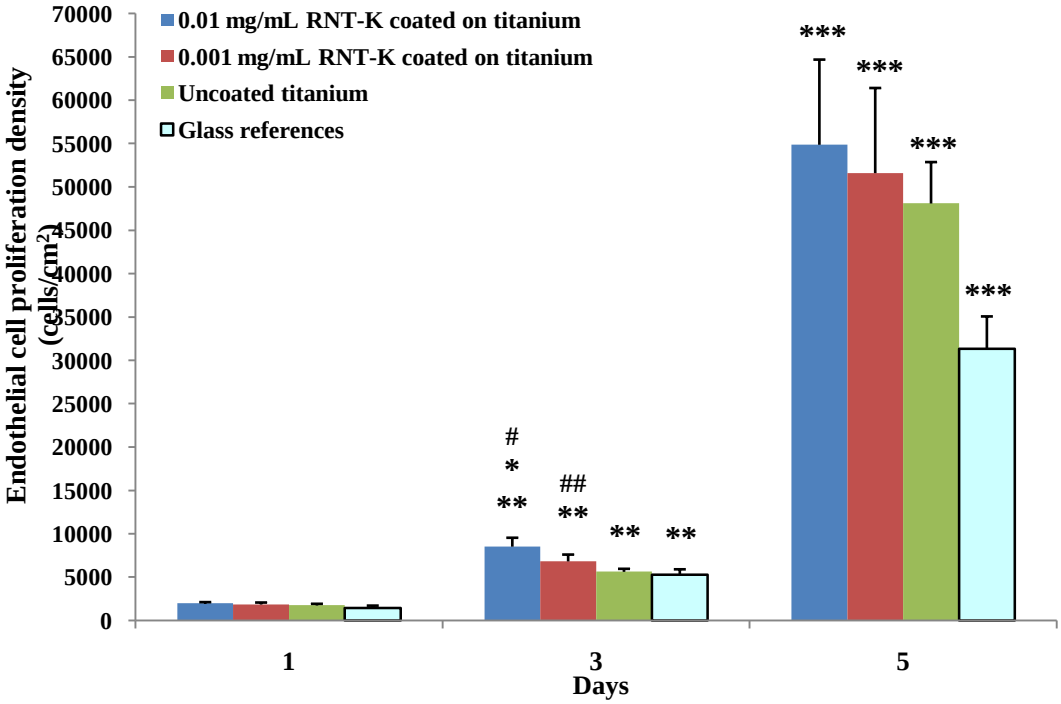

Figure 4.14 Enhanced endothelial cell density on RNT-K coated on titanium after 3 and 5 days. Values are means ±SEM; N=3; #p<0.01 and ##p<0.05 compared to uncoated titanium on day 3; *p<0.05 compared to 0.001 mg/ml RNT-K coated on titanium on day 3; **p<0.001 compared to respective substrates on day 1; ***p<0.001 compared to respective substrates on day 3. The proliferation data was collected by Eli Fine from Biomedical Engineering Department at Brown University [27].

By the 5th day, the RNT coated titanium still had a higher average density, but the differences were no longer significant (Figure 4.14). This leaved open the possibility that cells continued to proliferate at a higher rate on the RNT coated titanium but reached confluence earlier than the uncoated substrate during the undocumented time between 3 and 5 days. Furthermore, Figure 4.15 showed more endothelial cell densities on RNT coated titanium than uncoated titanium after 1, 3 and 5 days. Figure 4.16 revealed the endothelial cell spreading morphology images. The flat and well spread cell morphologies were observed on RNT coated titanium after 3 days and cells on all three substrate types had reached confluence by the 5th day.

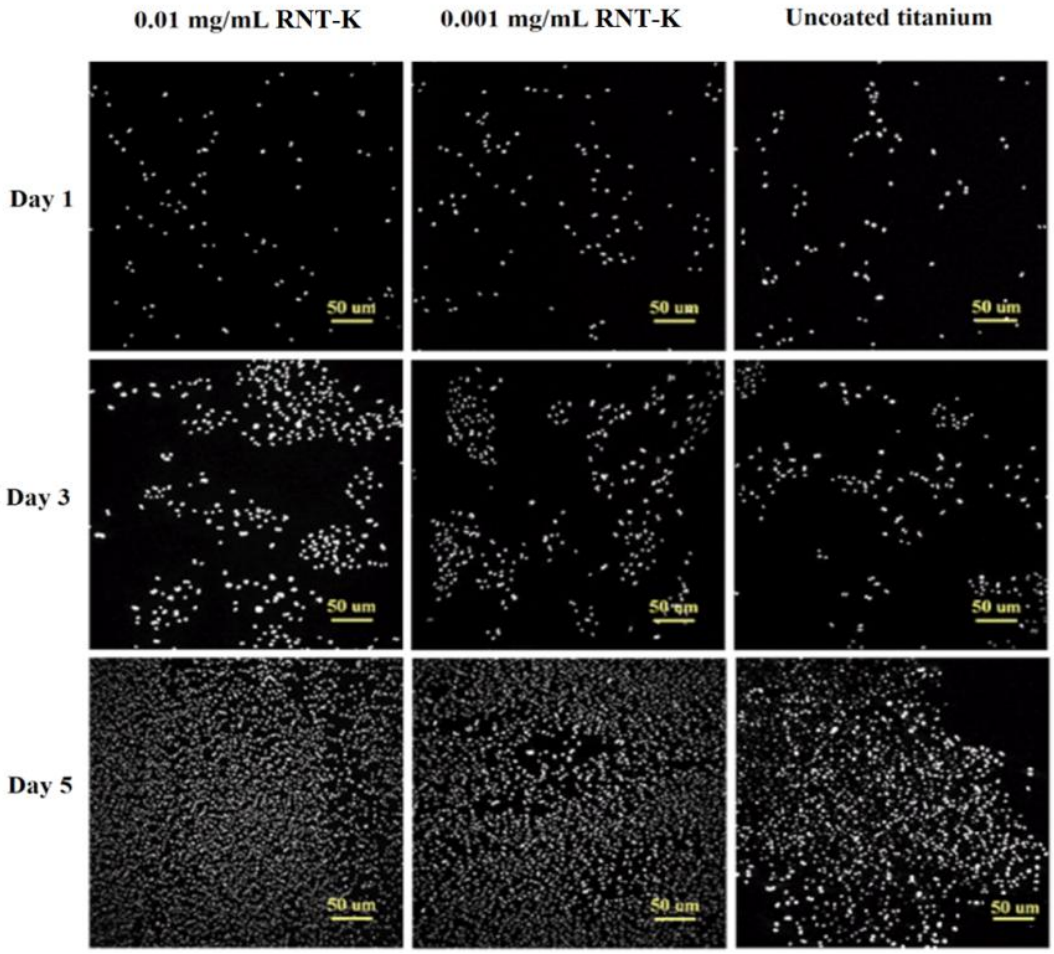

Figure 4.15 The fluorescence microscopy images of increasing endothelial cell densities (DAPI stain) on 0.01 mg/mL and 0.001 mg/mL RNT-K coated on titanium compared to uncoated titanium after 1, 3 and 5 days of proliferation.

In short, this study showed the improved endothelial cell adhesion and proliferation on RNT coated titanium, which suggested the potential and promise of these biomimetic RNT coatings for improved vascular stent application. Further investigations may determine the adherence strength of RNT coating on the titanium under the shear stress of the physiological flow of the bloodstream.

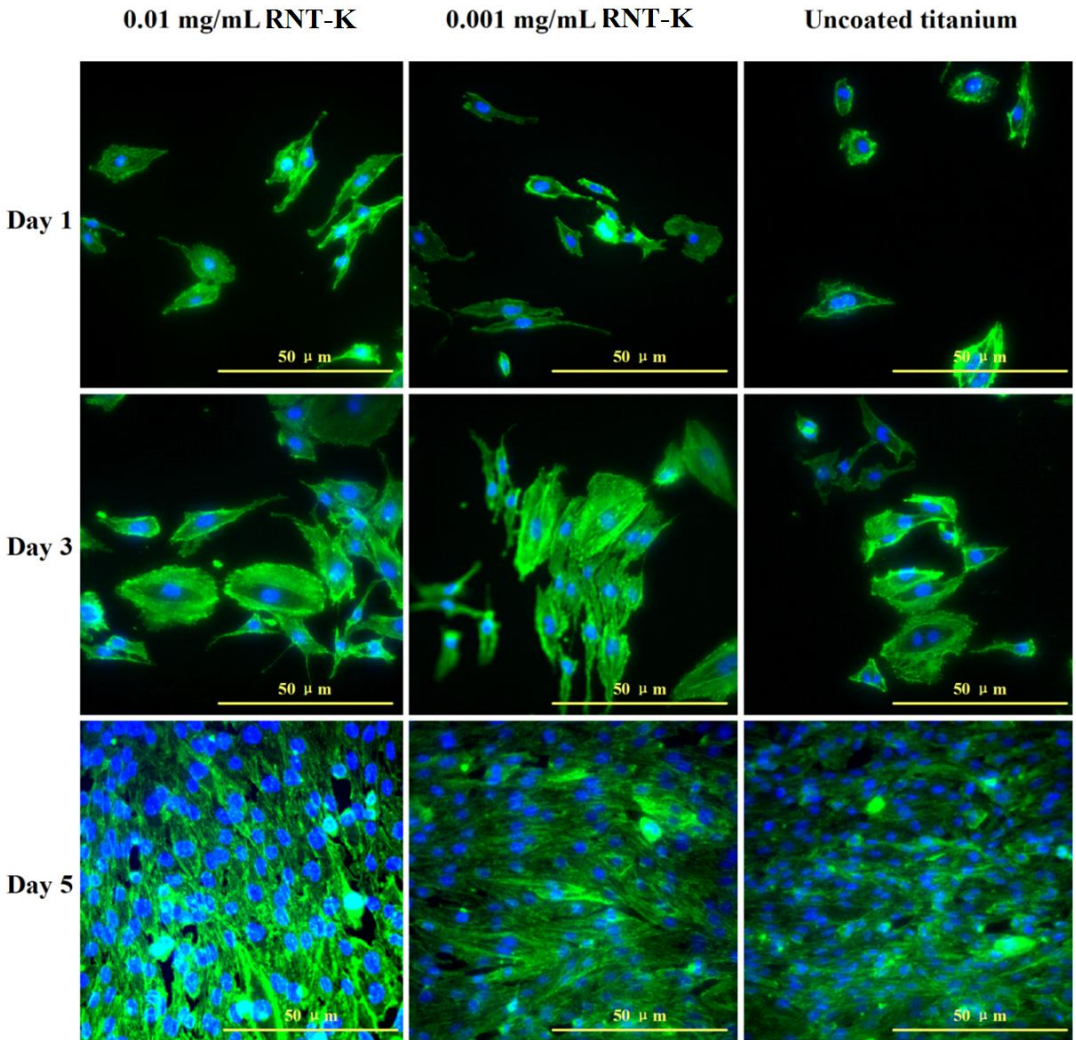

Figure 4.16 The fluorescence microscopy images of double-stained endothelial cell spreading morphologies on 0.01 mg/mL, 0.001 mg/mL RNT-K coated on titanium and uncoated titanium after 1, 3 and 5 days of proliferation. F-actins were stained by rhodamine (green color) and cell nuclei were stained by DAPI (blue color).

4.5 Conclusions

In summary, this study tested the cytocompatibility of a novel KRSR functionalized RNTs as orthopedic coating materials. The greater osteoblast adhesion was observed on the RNT-KRSR coated titanium than on uncoated titanium and unmodified RNT-K coated titanium. In contrast, the fibroblast adhesion did not improve on the RNT-KRSR

and other types of RNTs compared to uncoated controls. Furthermore, KRSR peptide inhibited the undesirable fibroblast adhesion, which made the selectively controlled cell growth possible at the bone defect site. Therefore, this study suggested that RNTs with diverse amino acid and peptide side chains had excellent cytocompatibility properties and favorable surface chemistry for selectively enhancing bone cell attachments.

Moreover, the 7, 14 and 21 days of osteoblast differentiation study demonstrated that nanostructured RNT-K hydrogels even at a very low concentration (such as 0.001 mg/mL) had greater and quicker calcium deposition and alkaline phosphatase activity than hydrogel controls and glass references. This confirmed the excellent cytocompatiblity of RNTs as shown in previous chapters and indicated that the nanoscale features, chemical composition and the flexible design of RNTs created a biomimetic bone-like environment for improved orthopedic applications.

Last but not the least, the initial investigation of the effects of RNTs on endothelial cell function yielded very positive results. Titanium coated with RNTs showed a significant increase in endothelial cell densities compared to uncoated titanium after 4 h in the adhesion study and after 3 days in the proliferation study. While further investigations, such as testing cell growth in a flow system and in vivo study, are needed to determine the suitability of RNTs as a vascular stent coating, the results of this study showed great promise for RNTs to improve vascular stent applications. Furthermore, since growing new blood vessels was important for bone growth as well, the increased endothelial cell function on RNTs was also good for orthopedic applications.

4.6 References

[1] Dalton BA, McFarland CD, Underwood PA, Steele JG. Role of the heparin-binding domain of fibronectin in attachment and spreading of human bone-derived cells. J Cell Sci 1995;108:2083–2092.

[2] Nakamura H, Ozawa H. Immunohistochemical localization of heparan sulfate proteoglycan in rat tibiae. J Bone Min Res 1994;9:1289–1299.

[3] Puleo DA, Bizios R. Mechanisms of fibronectin mediated attachment of osteoblasts to substrates in vitro. Bone Miner 1992;18:215–226.

[4] Hasenbein ME, Andersen TT, Bizios R. Micropatterned surfaces modified with select peptides promote exclusive interactions with osteoblasts. Biomaterials 2002;19:3937–3942

[5] Dee KC, Andersen TT, Bizios R. Design and function of novel osteoblast-adhesive peptides for chemical modification of biomaterials. J Biomed Mater Res 1998;40:371–377.

[6] Moralez JG, Raez J, Yamazaki T, Motkuri RK, Kovalenko A, Fenniri H. Helical rosette nanotubes with tunable stability and hierarchy. J Am Chem Soc 2005;127:8307–8309.

[7] Restenosis. http://www.angioplasty.org/devices6.html.

[8] Problems resurface with drug eluting stents. Angioplasty.org, http://www.ptca.org/newscenter.html?http://www.ptca.org/news/2006/0904.html

[9] Zhang L, Webster TJ. Nanotechnology and nanomaterials: promises for improved tissue regeneration. Nanotoday 2009;4:66–80.

[10] Choudhary S, Haberstroh KM, Webster TJ. Enhanced functions of vascular cells on nanostructured Ti for improved stent applications. Tissue Eng 2007;13:1421–1430.

[11] Miller DC, Haberstroh KM, Webster TJ. PLGA nanometer surface features manipulate fibronectin interactions for improved vascular cell adhesion. J Biomed Mater Res 2007;81A:678–684.

[12] Lee SJ, Yoo JJ, Lim GJ, Atala A, Stitzel J. In vitro evaluation of electrospun nanofiber scaffolds for vascular graft application. J Biomed Mater Res 2007;83A:999–1008.

[13] Genove´E, Shen C, Zhang S, Semino CE. The effect of functionalized self-assembling peptide scaffolds on human aortic endothelial cell function. Biomaterials 2005;26:3341–3351.

[14] http://myhealth.ucsd.edu/library/healthguide/en-us/support/topic.asp?hwid=zm2311

[15] Curfman GD, Morrissey S, Jarcho JA, Drazen JM. Drug-eluting coronary stents -promise and uncertainty. The new England journal of medicine 2007;356:1059–1060.

[16] Webster TJ, Ergun C, Doremus RH, Siegel RW. Enhanced functions of osteoblasts on nanophase ceramics. Biomaterials 2000;21:1803–1810.

[17] Price RL, Gutwein LG, Kaledin L, Tepper F, Webster TJ. Osteoblast function on nanophase alumina materials: Influence of chemistry, phase, and topography. J Biomed Mater Res 2003;67A:1284–1293.

[18] Balasundaram G, Webster TJ. Increased osteoblast adhesion on nanograined Ti modified with KRSR. J Biomed Mater Res 2007;80A:602–611.

[19] Nelson M, Balasundaram G, Webster TJ. Increased osteoblast adhesion on nanoparticulate crystalline hydroxyapatite functionalized with KRSR. Int J Nanomed 2006:1;339–349.

[20] Webster TJ. Nanophase ceramics: the future orthopedic and dental implant material. In: Ying JY, editor. Advances in chemical engineering. New York: Academic Press, 2001, p.125–166.

[21] http://www.medterms.com/script/main/art.asp?articlekey=8701

[22] Chim H, Ong JL, Schantz JT, Hutmacher DW, Agrawal CM. Efficiency of glow discharge gas plasma treatment as a surface modification process for three-dimensional poly(d,l-lactide)scaffolds. J Biomed Mater Res A 2003;65:327–335.

[23] Zhang L, Ramsaywack S, Fenniri H, Webster T.J. Enhanced osteoblast adhesion on self-assembled nanostructured hydrogel scaffolds, Tissue Eng 2008;14:1353-1364.

[24] Zhang L, Rakotondradany F, Myles AJ, Fenniri H, Webster TJ. Arginine-glycine-aspartic acid modified rosette nanotube hydrogel composites for bone tissue engineering. Biomaterials 2009;30:1309–1320.

[25] Zhang L, Rodriguez J, Myles AJ, Fenniri H, Webster TJ. Biologically inspired rosette nanotubes and nanocrystalline hydroxyapatite hydrogel nanocomposites

as improved bone substitutes. Nanotechnology, in press, 2009.

[26] Wang GX, Deng XY, Tang CJ, et al. The adhesive properties of endothelial cells on endovascular stent coated by substrates of poly L-Lysine and fibronectin. Artif Cells Blood Substit Immobil Biotechnol 2006;34:11-25.

[27] Fine E, Zhang L, Fenniri H, Webster TJ. Enhance endothelial cell functions on helical rosette nanotubes coated titanium for improved vascular stent applications. J Nanosci Nanotech, in press, 2009.